

SENSORS & TRANSDUCERS

ISSN 1726-5479

vol. 207

12/16

Electronic version. Not for distribution.

Electronic version. Not for distribution.

Sensors and Electronic Instrumentation

International Frequency Sensor Association Publishing



Sensors & Transducers

**International Official Open Access Journal of the
International Frequency Sensor Association (IFSA)
Devoted to Research and Development
of Sensors and Transducers**

Volume 207, Issue 12, December 2016

Editor-in-Chief

Prof., Dr. Sergey Y. YURISH



IFSA Publishing: Barcelona • Toronto

Sensors & Transducers is an open access journal which means that all content (article by article) is freely available without charge to the user or his/her institution. Users are allowed to read, download, copy, distribute, print, search, or link to the full texts of the articles, or use them for any other lawful purpose, without asking prior permission from the publisher or the author. This is in accordance with the BOAI definition of open access. Authors who publish articles in *Sensors & Transducers* journal retain the copyrights of their articles. The *Sensors & Transducers* journal operates under the Creative Commons License CC-BY.

Notice: No responsibility is assumed by the Publisher for any injury and/or damage to persons or property as a matter of products liability, negligence or otherwise, or from any use or operation of any methods, products, instructions or ideas contained in the material herein.

Published by International Frequency Sensor Association (IFSA) Publishing. Printed in the USA.





Editors-in-Chief: Professor, Dr. Sergey Y. Yurish, tel.: +34 696067716, e-mail: editor@sensorsportal.com

Editors for Western Europe

Meijer, Gerard C.M., Delft Univ. of Technology, The Netherlands
Ferrari, Vittorio, Università di Brescia, Italy
Mescheder, Ulrich, Univ. of Applied Sciences, Furtwangen, Germany

Editor for Eastern Europe

Sachenko, Anatoly, Ternopil National Economic University, Ukraine

Editors for North America

Katz, Evgeny, Clarkson University, USA
Datskos, Panos G., Oak Ridge National Laboratory, USA
Fabien, J. Josse, Marquette University, USA

Editor for Africa

Maki K., Habib, American University in Cairo, Egypt

Editors South America

Costa-Felix, Rodrigo, Inmetro, Brazil
Walsoe de Reca, Noemi Elisabeth, CINSO-CITEDEF
UNIDEF (MINDEF-CONICET), Argentina

Editors for Asia

Ohyama, Shinji, Tokyo Institute of Technology, Japan
Zhengbing, Hu, Huazhong Univ. of Science and Technol., China
Li, Gongfa, Wuhan Univ. of Science and Technology, China

Editor for Asia-Pacific

Mukhopadhyay, Subhas, Massey University, New Zealand

Editorial Board

Abdul Rahim, Ruzairi, Universiti Teknologi, Malaysia
Abramchuk, George, Measur. Tech. & Advanced Applications, Canada
Aluri, Geetha S., Globalfoundries, USA
Ascoli, Giorgio, George Mason University, USA
Atalay, Selcuk, Inonu University, Turkey
Atghiaee, Ahmad, University of Tehran, Iran
Augutis, Vygantas, Kaunas University of Technology, Lithuania
Ayeshe, Aladdin, De Montfort University, UK
Baliga, Shankar, B., General Monitors, USA
Barlingay, Ravindra, Larsen & Toubro - Technology Services, India
Basu, Sukumar, Jadavpur University, India
Booranawong, Apidet, Prince of Songkla University, Thailand
Bousbia-Salah, Mounir, University of Annaba, Algeria
Bouvet, Marcel, University of Burgundy, France
Campanella, Luigi, University La Sapienza, Italy
Carvalho, Vitor, Minho University, Portugal
Changhai, Ru, Harbin Engineering University, China
Chen, Wei, Hefei University of Technology, China
Cheng-Ta, Chiang, National Chia-Yi University, Taiwan
Cherstvy, Andrey, University of Potsdam, Germany
Chung, Wen-Yaw, Chung Yuan Christian University, Taiwan
Cortes, Camilo A., Universidad Nacional de Colombia, Colombia
D'Amico, Arnaldo, Università di Tor Vergata, Italy
De Stefano, Luca, Institute for Microelectronics and Microsystem, Italy
Ding, Jianning, Changzhou University, China
Djordjevic, Alexander, City University of Hong Kong, Hong Kong
Donato, Nicola, University of Messina, Italy
Dong, Feng, Tianjin University, China
Erkmen, Aydan M., Middle East Technical University, Turkey
Fezari, Mohamed, Badji Mokhtar Annaba University, Algeria
Gaura, Elena, Coventry University, UK
Gole, James, Georgia Institute of Technology, USA
Gong, Hao, National University of Singapore, Singapore
Gonzalez de la Rosa, Juan Jose, University of Cadiz, Spain
Goswami, Amarjyoti, Kaziranga University, India
Guillet, Bruno, University of Caen, France
Hadjiloucas, Sillas, The University of Reading, UK
Hao, Shiyong, Michigan State University, USA
Hui, David, University of New Orleans, USA
Jaffrezic-Renault, Nicole, Claude Bernard University Lyon 1, France
Jamil, Mohammad, Qatar University, Qatar
Kaniusas, Eugenijus, Vienna University of Technology, Austria
Kim, Min Young, Kyungpook National University, Korea
Kumar, Arun, University of Delaware, USA
Lay-Ekuakille, Aime, University of Lecce, Italy
Li, Fengyuan, HARMAN International, USA
Li, Jingsong, Anhui University, China
Li, Si, GE Global Research Center, USA
Lin, Paul, Cleveland State University, USA
Liu, Aihua, Chinese Academy of Sciences, China
Liu, Chenglian, Long Yan University, China
Liu, Fei, City College of New York, USA
Mahadi, Muhammad, University Tun Hussein Onn Malaysia, Malaysia

Mansor, Muhammad Naufal, University Malaysia Perlis, Malaysia
Marquez, Alfredo, Centro de Investigacion en Materiales Avanzados, Mexico
Mishra, Vivekanand, National Institute of Technology, India
Moghavvemi, Mahmoud, University of Malaya, Malaysia
Morello, Rosario, University "Mediterranea" of Reggio Calabria, Italy
Mulla, Intiaz Sirajuddin, National Chemical Laboratory, Pune, India
Nabok, Aleksey, Sheffield Hallam University, UK
Neshkova, Milka, Bulgarian Academy of Sciences, Bulgaria
Passaro, Vittorio M. N., Politecnico di Bari, Italy
Patil, Devidas Ramrao, R. L. College, Parola, India
Penza, Michele, ENEA, Italy
Pereira, Jose Miguel, Instituto Politecnico de Seteabal, Portugal
Pillarsetti, Anand, Sensata Technologies Inc, USA
Pogacnik, Lea, University of Ljubljana, Slovenia
Pullini, Daniele, Centro Ricerche FIAT, Italy
Qiu, Liang, Avago Technologies, USA
Reig, Candid, University of Valencia, Spain
Restivo, Maria Teresa, University of Porto, Portugal
Rodríguez Martínez, Angel, Universidad Politécnica de Cataluña, Spain
Sadana, Ajit, University of Mississippi, USA
Sadeghian Marnani, Hamed, TU Delft, The Netherlands
Sapozhnikova, Ksenia, D. I. Mendeleev Institute for Metrology, Russia
Singhal, Subodh Kumar, National Physical Laboratory, India
Shah, Kriyang, La Trobe University, Australia
Shi, Wendian, California Institute of Technology, USA
Shmaliy, Yuriy, Guanajuato University, Mexico
Song, Xu, An Yang Normal University, China
Srivastava, Arvind K., Systron Donner Inertial, USA
Stefanescu, Dan Mihai, Romanian Measurement Society, Romania
Sumridetchkajorn, Sarun, Nat. Electr. & Comp. Tech. Center, Thailand
Sun, Zhiqiang, Central South University, China
Sysoev, Victor, Saratov State Technical University, Russia
Thirunavukkarasu, I., Manipal University Karnataka, India
Thomas, Sadiq, Heriot Watt University, Edinburgh, UK
Tian, Lei, Xidian University, China
Tianxing, Chu, Research Center for Surveying & Mapping, Beijing, China
Vanga, Kumar L., ePack, Inc., USA
Vazquez, Carmen, Universidad Carlos III Madrid, Spain
Wang, Jiangping, Xian Shiyong University, China
Wang, Peng, Qualcomm Technologies, USA
Wang, Zongbo, University of Kansas, USA
Xu, Han, Measurement Specialties, Inc., USA
Xu, Weihe, Brookhaven National Lab, USA
Xue, Ning, Agiltron, Inc., USA
Yang, Dongfang, National Research Council, Canada
Yang, Shuang-Hua, Loughborough University, UK
Yaping Dan, Harvard University, USA
Yue, Xiao-Guang, Shanxi University of Chinese Traditional Medicine, China
Xiao-Guang, Yue, Wuhan University of Technology, China
Zakaria, Zulkarnay, University Malaysia Perlis, Malaysia
Zhang, Weiping, Shanghai Jiao Tong University, China
Zhang, Wenming, Shanghai Jiao Tong University, China
Zhang, Yudong, Nanjing Normal University China

Contents

Volume 207
Issue 12
December 2016

www.sensorsportal.com

ISSN 2306-8515
e-ISSN 1726-5479

Research Articles

Editorial

Sergey Y. Yurish 1

Novel Ultrasonic Instrumentation Developments for Real-time Monitoring of Binary Gas Mixtures and Flow: Description and Applications

M. Battistin, S. Berry, P. Bonneau, O. Crespo-Lopez, C. Deterre, M. Doubek, G. Favre, G. Hallewell, S. Katunin, D. Lombard, A. O'Rourke, A. Madsen, S. McMahan, K. Nagai, C. Rossi, B. Pearson, D. Robinson, A. Rozanov, E. Stanecka, M. Strauss, V. Vacek, R. Vaglio, J. Young..... 4

Study of Virtual Body Frames in Dodecahedron-Based Skew Redundant Inertial Measurement Units

Marius V. Gheorghe 15

Ultra-fast Sensor for Single-photon Detection in a Wide Range of the Electromagnetic Spectrum

Astghik Kuzanyan, Armen Kuzanyan, Vahan Nikoghosyan 21

Development of a Novel High Reliable Si-Based Trace Humidity Sensor Array for Aerospace and Process Industry

Shuyao Zhou, Q. C. Dao, Biswajit Mukhopadhyay, Piotr Mackowiak, Oswin Ehrmann, Klaus-Dieter Lang, Michael Woratz, Peter Herrmann, T. Weiland, Olaf Pohl, Volker Noack, Ha-Duong Ngo..... 30

Preliminary Studies on Capacitive Proximity Sensing for Touchless Interaction with a Human Finger

Leonhard Haslinger and Bernhard G. Zagar..... 36

Vector Magnetometer Application with Moving Carriers

Andrii Prystaj, Valery Korepanov, Fedir Dudkin and Borys Ladanivskyy..... 44

UWB Radar Signal Processing for Localization of Persons with the Changing Nature of Their Movement

Dušan Kocur, Daniel Novák and Mária Švecová..... 50

An Optical Processor for Data Error Detection and Correction Using a (9,5) Binary Code Generator and the Syndrome Decoding Process

M. A. Vieira, M. Vieira, P. Louro, V. Silva and J. Costa 58

Characterization and Compensation of the Fixed Pattern Noise in the Output of a CCD Camera

Andreas W. Winkler and Bernhard G. Zagar 65

Electrochemical Study of Delta-9-Tetrahydrocannabinol by Cyclic Voltammetry Using Screen Printed Electrode, Improvements in Forensic Analysis

Marco Antonio Balbino, Izabel Cristina Eleoterio, Marcelo Firmino de Oliveira and Bruce Royston McCord..... 73

Dual Approach to Amplify Anodic Stripping Voltammetric Signals Recorded Using Screen Printed Electrodes

Agnieszka Królicka..... 79

Authors are encouraged to submit article in MS Word (doc) and Acrobat (pdf) formats by e-mail: editor@sensorsportal.com. Please visit journal's webpage with preparation instructions: <http://www.sensorsportal.com/HTML/DIGEST/Submission.htm>

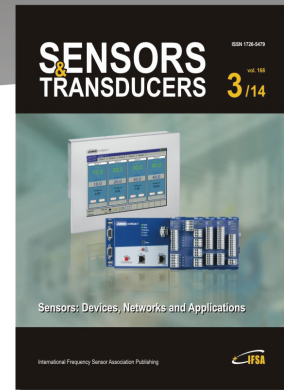
International Frequency Sensor Association (IFSA).

SENSORS & TRANSDUCERS

The Global Impact Factor of the journal is **0.987**

Open access, peer reviewed, established, international journal devoted to research, development and applications of sensors, transducers and sensor systems.

Published monthly by International Frequency Sensor Association (IFSA Publishing, S.L.) in print and electronic versions (ISSN 2306-8515, e-ISSN 1726-5479)



Submit your article at:
<http://www.sensorsportal.com/HTML/DIGEST/Submission.htm>



Online Experimentation: Emerging Technologies and IoT

Maria Teresa Restivo, Alberto Cardoso, António Mendes Lopes (Editors)

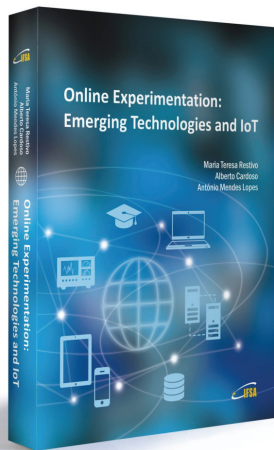
Online Experimentation: Emerging Technologies and IoT describes online experimentation, using fundamentally emergent technologies to build the resources and considering the context of IoT.

In this context, each online experimentation (OE) resource can be viewed as a "thing" in IoT, uniquely identifiable through its embedded computing system, and considered as an object to be sensed and controlled or remotely operated across the existing network infrastructure, allowing a more effective integration between the experiments and computer-based systems.

The various examples of OE can involve experiments of different type (remote, virtual or hybrid) but all are IoT devices connected to the Internet, sending information about the experiments (e.g. information sensed by connected sensors or cameras) over a network, to other devices or servers, or allowing remote actuation upon physical instruments or their virtual representations.

The contributions of this book show the effectiveness of the use of emergent technologies to develop and build a wide range of experiments and to make them available online, integrating the universe of the IoT, spreading its application in different academic and training contexts, offering an opportunity to break barriers and overcome differences in development all over the world.

Online Experimentation: Emerging Technologies and IoT is suitable for all who is involved in the development design and building of the domain of remote experiments.



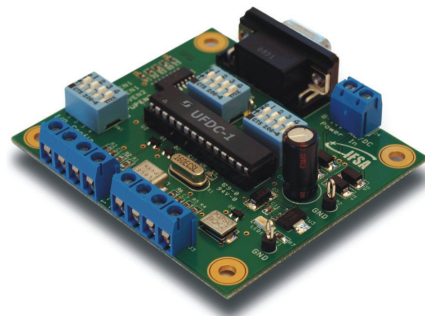
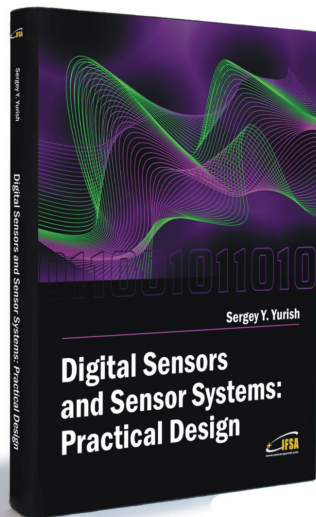
Hardcover: ISBN 978-84-608-5977-2
e-Book: ISBN 978-84-608-6128-7

Order: http://www.sensorsportal.com/HTML/BOOKSTORE/Online_Experimentation.htm

Digital Sensors and Sensor Systems: Practical Design

and

Development Board
EVAL UFDC-1/UFDC-1M-16



Buy book and Evaluation board together. **Save 30.00 EUR.**

Development Board EVAL UFDC-1 / UFDC-1M-16

Full-featured development kit for the Universal Frequency-to-Digital Converters UFDC-1 and UFDC-1M-16. 2 channel, 16 measuring modes, high metrological performance, RS232/USB interface, master and slave communication modes. On-board frequency reference (quartz crystal oscillator). Operation from 8 to 14 V AC/DC. Development board software is included.

All existing frequency, period, duty-cycle, time interval, pulse-width modulated, pulse number and phase-shift output sensors and transducers can be directly connected to this 2-channel DAQ system. The user can connect TTL-compatible sensors' outputs to the Development Board, measure any output frequency-time parameters, and test out the sensor systems functions.

Applications:

- Digital sensors and sensor systems
- Smart sensors systems
- Data Acquisition for frequency-time parameters of electric signals
- Frequency counters
- Tachometers and tachometric systems
- Virtual instruments
- Educational process in sensors and measurements
- Remote laboratories and distance education

Order online:

http://www.sensorsportal.com/HTML/BOOKSTORE/Digital_Sensors_and_Board.htm

Editorial



Dear Readers !

It is my great pleasure to introduce a new issue of *Sensors & Transducers* journal, Vol. 207, Issue 12, December 2016, titled '*Sensors and Electronic Instrumentation*'.

This issue contains selected and extended papers from *The 2nd International Conference on Sensors and Electronic Instrumentation Advances (SEIA' 2016)*, which taken place on 22–23 September 2016 in Barcelona, Castelldefels, Spain. The conference was organized by *International Frequency Sensor Association (IFSA)* and *Asian Society of Applied Mathematics and Engineering (ASAME)* in technical cooperation with *IFSA Publishing S. L.* and *Excelera, S.L.*

The SEIA' 2016 conference was focusing significant breakthrough and innovations in Sensors, Electronics, Measuring Instrumentation and Transducers Engineering Advances and its applications with broadest concept. It is a forum for presentation, discussion, and exchange of information and latest research and development results in both theoretical and experimental research and their related fields. It brings together researchers, developers, and practitioners from diverse fields including international scientists and engineers from academia, research institutes, and companies to present and discuss the latest results in the field of sensors and measurements. The first SEIA conference was held in Dubai (UAE), 21-22 November 2015.

SEIA' 2016 Conference Statistics

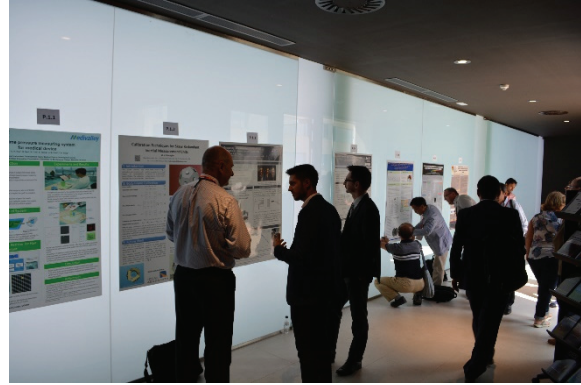
- Submitted papers: > 80
- Accepted papers: 44 (31 oral presentations & 13 posters)
- Countries: 26 (15 European and 11 non-European countries)
- Special Session: 1 (*Gas Sensors*)
- Industrial Presentation: 1
- Keynote Presentations: 4 (USA (2), Germany and China)

Table 1. Countries/Papers.

| Country | Papers | Country | Papers |
|----------------|--------|-------------|--------|
| Armenia | 1 | Mexico | 2 |
| Austria | 5 | Poland | 2 |
| China | 1 | Portugal | 4 |
| Czech Republic | 1 | Romania | 1 |
| Brazil | 1 | Russia | 4 |
| Finland | 1 | Slovakia | 1 |
| France | 1 | South Korea | 2 |
| Germany | 5 | Spain | 2 |
| Hungary | 1 | Sweden | 2 |
| India | 2 | Switzerland | 1 |
| Italy | 2 | UK | 1 |
| Japan | 6 | Ukraine | 1 |
| Malaysia | 1 | USA | 7 |

The Organizing Committee has selected 11 papers, presented on the SEIA' 2016 conference to be extended for journal's publications. Finally, these articles, written by authors from 15 countries are in this issue. A limited number of the best articles from this journal issue will be selected for extension

into book chapters for publication in our popular open access Book Series ‘*Advances in Sensors: Reviews*’ Vol. 5, which will be published in 2017. So, the authors will have a unique opportunity to get three publications in less than one year: conference paper, journal article and book chapter. Through the journal and book open access, the reach and impact of obtained research results can be substantially increased.



Photos from SEIA' 2016 Conference.

The 3rd *International Conference on Sensors and Electronic Instrumentation Advances (SEIA' 2017)* will take place in Moscow (Russia) on 20-22 September 2017. The conference will be organized by the *International Frequency Sensor Association (IFSA)* and *Asian Society of Applied Mathematics and Engineering (ASAME)* in technical cooperation with *National Research Center Kurchatov Institute, National Research Nuclear University (MEPhI)* and *General Physics Institute of Russian Academy of Sciences (GPI-RAS)*. Welcome to SEIA' 2017 !

I hope you will enjoy this issue.

With best wishes,

Sergey Y. Yurish
Editor-in-Chief



3rd International Conference on Sensors and Electronic Instrumentation Advances

20-22 September 2017
Moscow, Russia



The 3rd International Conference on Sensors and Electronic Instrumentation Advances (SEIA' 2017) is a forum for presentation, discussion, and exchange of information and latest research and development results in both theoretical and experimental research in sensors, transducers and their related fields. It brings together researchers, developers, and practitioners from diverse fields including international scientists and engineers from academia, research institutes, and companies to present and discuss the latest results in the field of sensors and measurements.

The conference is organized by the International Frequency Sensor Association (IFSA) and Asian Society of Applied Mathematics and Engineering (ASAME) in technical cooperation with National Research Center Kurchatov Institute and National Research Nuclear University (both from Moscow, Russia).

The conference is focusing any significant breakthrough and innovation in Sensors, Electronics, Measuring Instrumentation and Transducers Engineering Advances and its applications. Topics of Interest include any aspects of:

- Sensor Technology;
- Instruments and Measuring Technology.

Submission (2-page abstract) 20 March 2017
Notification of acceptance 20 April 2017
Registration 20 May 2017
Camera Ready 30 June 2017

Contribution Types:

Regular papers
Posters

One event - three publications !

1. All registered abstracts will be published in the conference proceedings.
2. Selected extended papers will be published in Sensors & Transducers journal.
3. The best full-page papers will be recommended to extend to book chapters for 'Advances in Sensors: Reviews' Book Series.



http://www.sensorsportal.com/SEIA_2017/

Novel Ultrasonic Instrumentation Developments for Real-time Monitoring of Binary Gas Mixtures and Flow: Description and Applications

³ M. Battistin, ³ S. Berry, ³ P. Bonneau, ³ O. Crespo-Lopez, ⁴ C. Deterre,
⁶ M. Doubek, ³ G. Favre, ⁷ G. Hallewell, ⁸ S. Katunin, ³ D. Lombard,
⁴ A. O'Rourke, ⁴ A. Madsen, ⁹ S. McMahon, ¹⁰ K. Nagai, ^{1,*} C. Rossi,
⁵ B. Pearson, ¹¹ D. Robinson, ⁷ A. Rozanov, ¹² E. Stanecka, ² M. Strauss,
⁶ V. Vacek, ³ R. Vaglio, ² J. Young

¹ INFN Genova, via Dodecaneso 33, 16146 Genova, Italy

^{2,5} Department of Physics and Astronomy, University of Oklahoma, Norman, OK 73019, USA

³ CERN, 1211 Geneva 23, Switzerland

⁴ DESY, Notkestraße 85, Hamburg 22607, Germany

⁶ Czech Technical University, Technická 4, 166 07 Prague 6, Czech Republic

⁷ Centre de Physique des Particules de Marseille, 163 Avenue de Luminy, 13288 Marseille, France

⁸ B.P. Konstantinov Petersburg Nuclear Physics Institute (PNPI), 188300 St. Petersburg, Russia

⁹ Rutherford Appleton Lab, Science & Technology Facilities Council, Chilton, OX110QX, UK

¹⁰ Department of Physics, Oxford University, Keble Road, Oxford OX1 3RH, UK

¹¹ Department of Physics, Cambridge University, J. J. Thomson Avenue, Cambridge, CB3 0HE, UK

¹² Institute of Nuclear Physics PAS, ul. Radzikowskiego 152, 31-342 Kraków, Poland

Tel.: +390103536236

* E-mail: cecilia.rossi@cern.ch

Received: 5 November 2016 / Accepted: 5 December 2016 / Published: 30 December 2016

Abstract: Custom ultrasonic instruments have been developed for continuous monitoring and real-time measurement of composition and flow in binary gas mixtures. These characteristics are derived from measurements of sound transit time along two opposite directions - parallel or tilted to the gas flow direction. The flow rate is then calculated from the transit time difference while the average is used to compute sound velocity by comparison with a sound velocity/composition database. Five devices are integrated in the Detector Control System of the ATLAS experiment at the CERN Large Hadron Collider. Three instruments monitor C₃F₈ and CO₂ coolant leaks into the nitrogen-purged envelopes of the inner silicon tracker; respectively with precisions better than $\pm 2 \times 10^{-5}$ and $\pm 10^{-4}$. Two further instruments are used to monitor the new thermosiphon C₃F₈ evaporative coolant recirculator. One of these measures C₃F₈ vapour return flow to the condenser while the other tracks air ingress into the condenser with a precision better than 10^{-3} . The precision of these instruments highlights their potential in other applications requiring continuous binary gas composition monitoring.

Keywords: Ultrasonic binary gas analysis, ATLAS Detector Control System, Sonar, thermosiphon, Evaporative cooling system.

1. Introduction

Custom ultrasonic (“sonar”) instruments have been developed for real-time monitoring and measurement of binary gas mixtures in the ATLAS experiment, one of the major experiments at the CERN Large Hadron Collider (LHC). ATLAS is a particle physics detector consisting of a series of concentric sub-detectors arranged around one of the LHC proton beam collision points [1]. The innermost sub-detector - the ATLAS Inner Detector (ID) - tracks charged particles in a solenoidal magnetic field using gas-based tracking elements and high resolution silicon detectors in microstrip and pixelated configurations. The silicon sub-detectors are closest to the beam collisions and

must be kept at low temperature ($-10\text{ }^{\circ}\text{C}$ or lower) to mitigate radiation damage. They are evaporatively cooled using C_3F_8 (octafluoropropane) and CO_2 . Three of five ultrasonic instruments monitor coolant leaks into the nitrogen-purged envelopes of these silicon tracking detectors. Two further instruments form part of the control system of the new thermosiphon C_3F_8 evaporative cooling recirculator plant [2], being commissioned to replace the present compressor-driven system. One (angled acoustic path) instrument was built to measure the C_3F_8 vapour flow returning to the thermosiphon condenser while another detects and eliminates (“degasses”) ingressed air from the condenser. The locations of the five instruments are shown in Fig. 1.

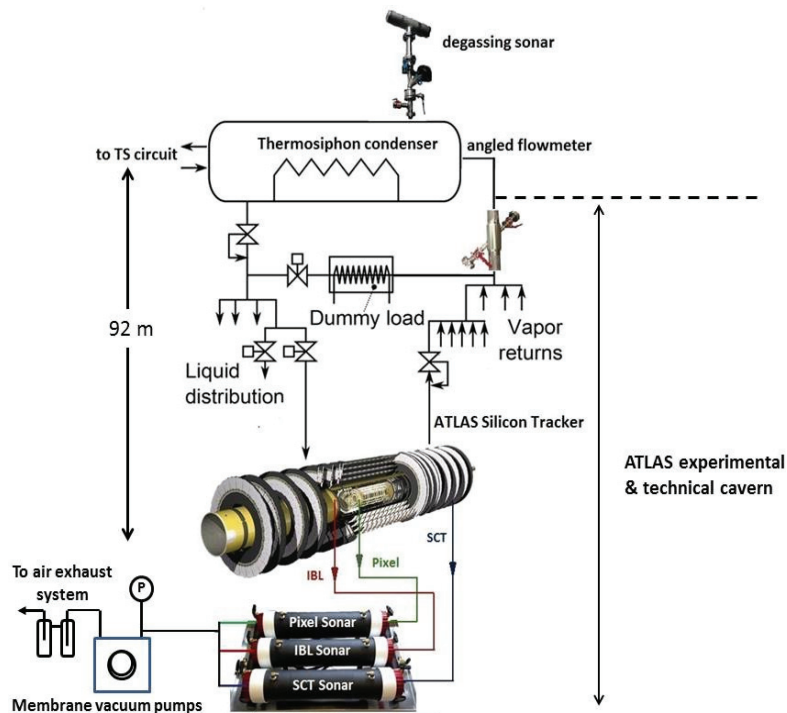


Fig. 1. Installations in the ATLAS Inner Detector. Three sonars monitor the N_2 envelopes of the (“Pixel”, “SCT” & “IBL”) silicon sub-detectors, while a degassing sonar and an angled flowmeter monitor the thermosiphon recirculator.

2. The Instrument and its Operating Principle

The instruments contain facing pairs of 50 kHz capacitive ultrasonic transducers [3] within flanged envelopes through which gas flows. When transmitting, a transducer is excited by $(300 \rightarrow 0\text{V})$ square pulses, generated from low-voltage precursors in a dsPIC33F microcontroller. A 40 MHz transit time clock is started synchronously with the leading edge of the first transmitted pulse. The acoustic signal received by the other transducer is passed through amplifiers and a comparator, stopping the clock when a user-defined threshold is crossed (Fig. 2).

The micro-controller also reverses the transmission direction for the transit time to be

measured in both directions (Fig. 2). These transit times are then used with geometrical parameters to evaluate the gas flow rate.

The ultrasonic instruments can be used for simultaneous gas flow measurement and composition analysis, exploiting the physical phenomenon whereby - at known temperature and pressure - the sound velocity in a binary gas mixture depends on the molar concentration of its components. For binary gas analysis, the sound velocity is calculated from the average of the transit times in opposite directions and then compared in real-time to a stored concentration vs. sound velocity database for a given temperature and pressure. This database can be generated from theoretical models and/or from previously-made calibration mixtures [4].

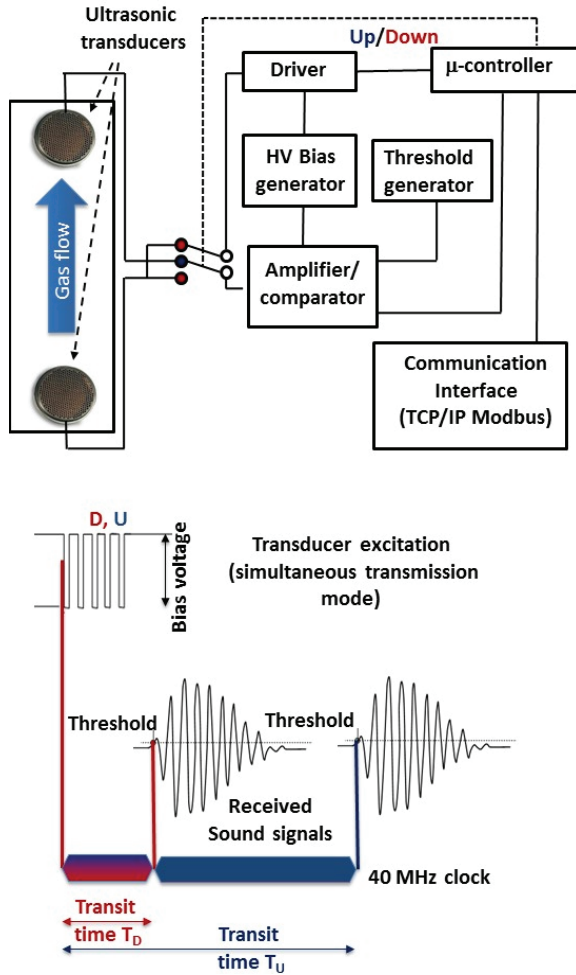


Fig. 2. Principle of operation of bi-directional ultrasonic transmission and detection in the instrument.

The software employs sound velocity *vs.* concentration look-up tables using the general formalism for the speed of sound in a gas mixture, combining the thermodynamic properties of pairs of component gases:

$$v_s = \sqrt{\frac{\gamma_m \cdot R \cdot T}{M_m}}, \quad (1)$$

where R is the molar gas constant ($8.3145 \text{ J} \cdot \text{mol}^{-1} \cdot \text{K}^{-1}$), T is the absolute temperature in Kelvin, M_m is the combined molar mass of the mixture and γ_m is the adiabatic index for the mixture.

M_m and γ_m are given respectively by

$$M_m = \sum_i \omega_i M_i \quad \text{and} \quad \gamma_m = \frac{\sum_i \omega_i C_{P_i}}{\sum_i \omega_i C_{V_i}}, \quad (2)$$

where ω_i is the molar fraction of component i in the mixture while C_{P_i} and C_{V_i} are the component's molar specific heats at constant pressure and volume respectively. The C_P and C_V values for the individual mixture components are calculated using the NIST REFPROP package [5] over the expected range of

operating temperature and pressure. Examples of these calculations are shown in in Fig. 3, Fig. 4 and Fig. 5 for C_3F_8 and N_2 .

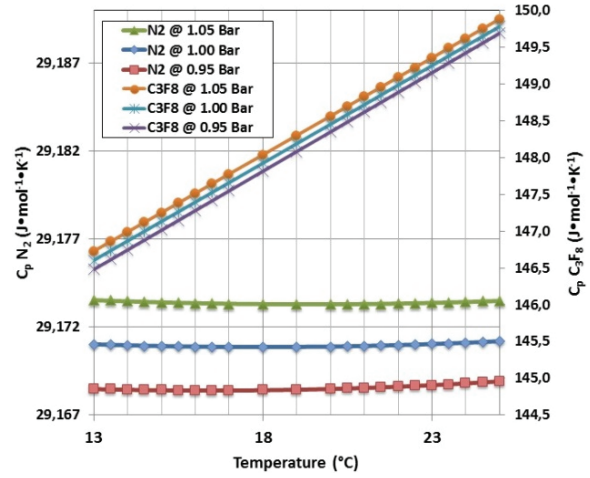


Fig. 3. Molar specific heat at constant pressure *vs.* temperature for N_2 (left vertical axis) and C_3F_8 (right vertical axis) at a range of temperatures and pressures.

For each pair of gases a database is created of sound velocity *vs.* concentration of the components, covering the expected range of temperature and pressure. Sound velocity *vs.* concentration is stored as a series of polynomial fit parameters at each temperature and pressure. These fit parameters can be thought of as being vertically-suspended above the intersections of a 2-D grid of temperature and pressure points. For the $\text{C}_3\text{F}_8/\text{N}_2$ and CO_2/N_2 gas combinations this grid runs from 13-25°C in 1°C steps and from 900-1100 mbar_{abs} in 20 mbar steps. In the case of the degassing sonar of the thermosiphon condenser (Section 3) the range is from 10-45°C in 1°C steps and from 300-1500 mbar_{abs} in 100 mbar steps.

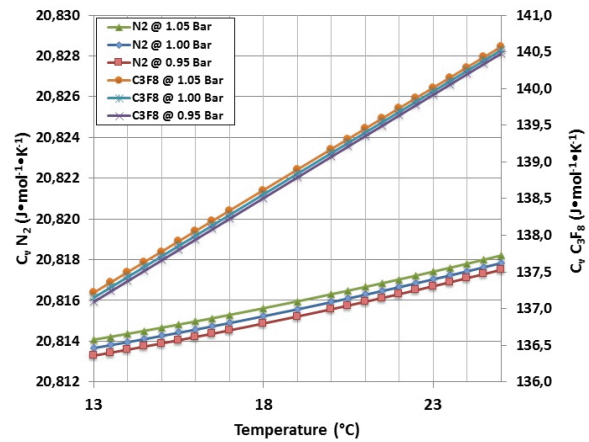


Fig. 4. Molar specific heat at constant volume *vs.* temperature for N_2 (left vertical axis) and C_3F_8 (right vertical axis) at a range of temperatures and pressures.

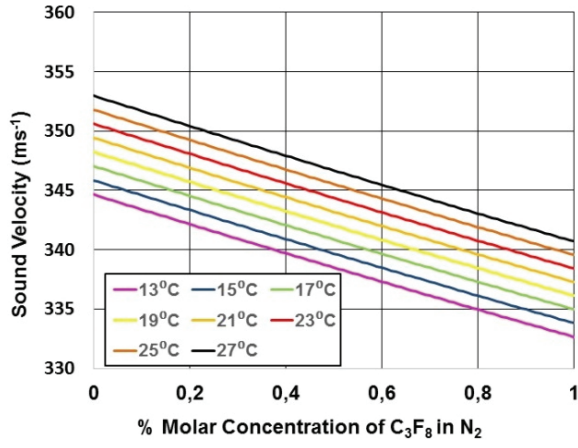


Fig. 5. Variation of Sound velocity in the range 0-0.1 % C_3F_8 in N_2 .

In practice the temperature and pressure (measured simultaneously with transit times) will fall between the grid: sound velocity vs. concentration fit parameters are first interpolated to intermediate values corresponding to the measurement temperature at grid pressures immediately above and below the measurement pressure. In a second step a linear interpolation between the intermediate fit parameters is made along the orthogonal (pressure) direction to calculate the final parameters corresponding to both the measured temperature and pressure. From these parameters the relative concentrations of the two components are calculated.

The precision of the instrument for measurements of sound velocity is better than $0.05 \text{ m}\cdot\text{s}^{-1}$. Contributions to this uncertainty, δc , are due to:

- $\pm 0.2 \text{ }^\circ\text{C}$ temperature stability in the sonar tube (equivalent to $\pm 0.044 \text{ m}\cdot\text{s}^{-1}$);
- $\pm 4 \text{ mbar}$ pressure stability ($\pm 0.012 \text{ m}\cdot\text{s}^{-1}$);
- $\pm 0.1 \text{ mm}$ transducer inter-foil measurement uncertainty ($\pm 0.018 \text{ m}\cdot\text{s}^{-1}$);
- $\pm 100 \text{ ns}$ electronic transit time measurement uncertainty ($0.002 \text{ m}\cdot\text{s}^{-1}$).

The precision of mixture determination, $\delta(\text{mix})$, at any concentration of the N_2 and C_3F_8 components is given by:

$$\delta(\text{mix}) = \frac{\partial c}{m}, \quad (3)$$

where m is the local slope of the *sound velocity vs. concentration* curve ($\text{m}\cdot\text{s}^{-1}[\%C_3F_8]^{-1}$).

As an example, the average gradient of the sound velocity vs. concentration curve is $-12.55 \text{ m}\cdot\text{s}^{-1}[\%C_3F_8]^{-1}$ for C_3F_8 concentrations in the range 0-0.1 % in N_2 . The intrinsic sound velocity measurement uncertainty of $\pm 0.05 \text{ m}\cdot\text{s}^{-1}$ yields, via Eq. (3) a corresponding mixture uncertainty of $\pm 0.004 \text{ } \%$.

To accurately measure the distance, L , between the membranes of the ultrasonic transducers a calibration based on two gases with different sound velocities can be used. This method takes into account the possibility

that the measured transit times (tt) in the two gases might include a transit time offset, tt_{offset} , for the time taken for the signals from the detected sound pulses to rise sufficiently to cross the comparator thresholds (Fig. 2). The real transit time (tt') in each gas has therefore to be corrected with an offset time (e.g. $tt'_{C_3F_8} = tt_{C_3F_8} - tt_{offset}$). It is also necessary to know the true sound velocity, V_s , in each component gas at the temperature and pressure where the calibration is carried out. These can be also calculated using the NIST-REFPROP package [5].

Taking as an example a two-gas calibration based on real component sound velocities and measured transit times in pure C_3F_8 and pure N_2 :

$$V_{sC_3F_8} = \frac{L}{tt'_{C_3F_8}}; V_{sN_2} = \frac{L}{tt'_{N_2}}, \quad (4)$$

$$L = \frac{V_{sC_3F_8} \cdot V_{sN_2} \cdot (tt_{C_3F_8} - tt_{N_2})}{V_{sN_2} - V_{sC_3F_8}}, \quad (5)$$

$$tt'_{N_2} = \frac{V_{sC_3F_8} \cdot (tt_{C_3F_8} - tt_{N_2})}{V_{sN_2} - V_{sC_3F_8}} \quad (6)$$

$$tt'_{C_3F_8} = \frac{V_{sN_2} \cdot (tt_{C_3F_8} - tt_{N_2})}{V_{sN_2} - V_{sC_3F_8}}, \quad (7)$$

$$tt_{offset} = \frac{V_{sC_3F_8} \cdot tt_{C_3F_8} - V_{sN_2} \cdot tt_{N_2}}{V_{sN_2} - V_{sC_3F_8}} \quad (8)$$

Each of the five sonar instruments integrated into the Detector Control System (DCS) of the ATLAS experiment (Fig. 1) has local electronics consisting of an acoustic timing module, analog input modules for the acquisition of temperatures and pressures and an external communication module, communicating with each other through a local bus running a custom 2-wire communication protocol. A schematic of the 2-wire protocol electronics is shown in Fig. 6 and an implementation photograph in Fig. 7. The 2-wire bus can also house additional modules for 4-20 mA DAC outputs and for the control of sampling valves and aspirating pumps. The external communication interface is based on an MBED module [6]. Due to the long distances (hundreds of meters) between the dispersed instruments, communication to the central Dell R610 SCADA (Supervisory, Control And Data Acquisition) computer uses the TCP/IP Modbus protocol over Ethernet (Fig. 8).

The data acquisition software is implemented in Siemens Symantic WINCC-OA version 3.11 [8] running on Linux. The WINCC project runs the Graphical User Interface (GUI) and also handles the continuous archiving of speed of sound, transit time, concentration, temperature and pressure data from each sonar to the ATLAS DCS oracle database. The software also controls the system through a finite state machine (FSM). Out-of-range alarms can be generated and are propagated through the FSM to an external GSM and e-mail alert system.

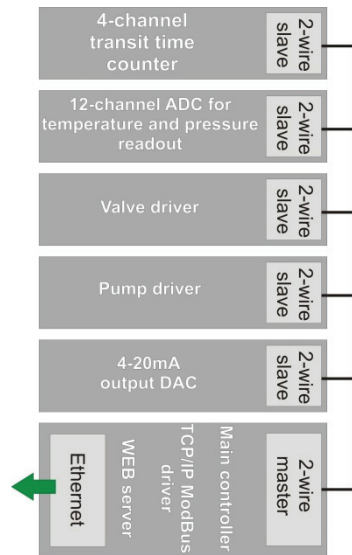


Fig. 6. Diagram of the 2-wire protocol electronics [7].

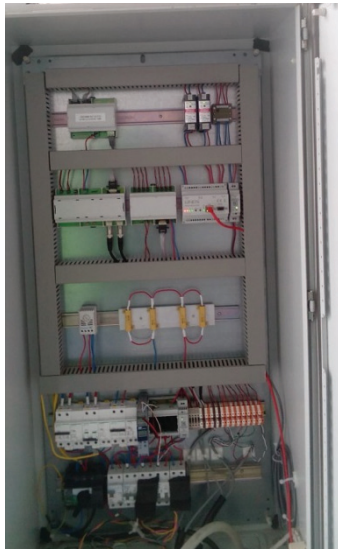


Fig. 7. Electronic implementation in weatherproof cabinet (degassing sonar).

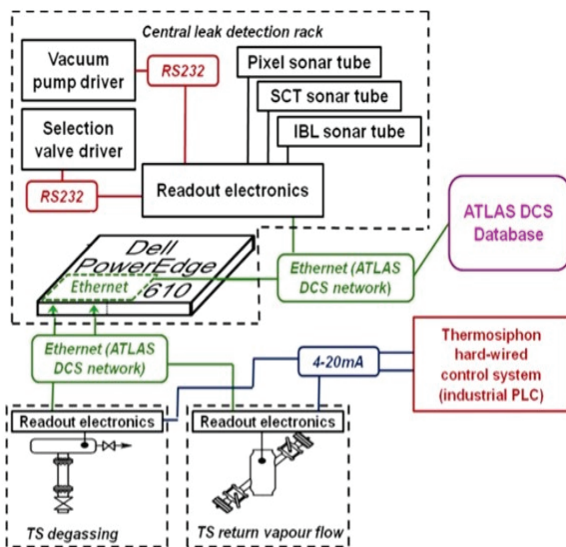


Fig. 8. Readout architecture of the full sonar system [9].

Fig. 9 illustrates part of the WINCC-OA GUI which handles the gas selection for the sonar tubes used to monitor coolant leaks into the N_2 -purged volumes surrounding the sub-elements of the ATLAS silicon tracker.

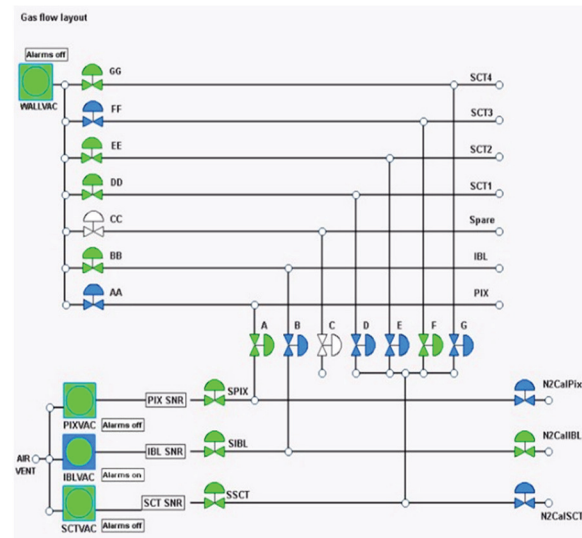


Fig. 9. Part of the sonar system graphical user interface implemented in Siemens Symantec ® WinCC-OA [8].

3. Application and Commissioning of the Instruments in the ATLAS Thermosiphon Cooling Recirculator

3.1. Degassing Sonar

Two instruments are directly implemented in the new ATLAS thermosiphon C_3F_8 evaporative coolant circulation system shown in Fig. 1. The thermosiphon takes advantage of the typical configuration of the LHC experiments located around 100 m underground. It is based on the physical phenomenon of natural circulation: C_3F_8 is condensed at the lowest temperature/pressure ($-60^\circ C$, 309 mbar_{abs}) but at the highest elevation in the system. In ATLAS the driving force of the circuit is given by the 92 m liquid column, starting from the condenser. The C_3F_8 refrigerant exits the detector as a vapour at $-25^\circ C$ and 1.67 bar_{abs} and returns to the condenser against gravity due to pressure differential. The thermosiphon system must provide 60 kW of on-detector cooling capacity, and guarantee a vapour pressure of 1.67 bar_{abs} at the end of the on-detector cooling loops for stable operation of the silicon tracking detector components in the high radiation zone near the LHC beams. To achieve 60 kW cooling capacity 1.2 kg·s⁻¹ of C_3F_8 must be circulated and condensed. A diagram of the thermosiphon plant is shown in Fig. 10. The purpose of the new cooling system is to replace the compressors of the present cooling plant recirculator, removing “active” (reciprocating) components from the primary cooling loop, leading to a more reliable system requiring less maintenance.

The “degassing” sonar (Fig. 1) represents the key tool for the detection and elimination of air leaks into the thermosiphon plant. The instrument is placed on the top of the thermosiphon condenser, at the lowest temperature and pressure of the cooling system, and therefore at the point where any air leaks will accumulate. The ingress of air must be avoided since an increase in condenser pressure will erode the pressure differential needed to circulate the $1.2 \text{ kg}\cdot\text{s}^{-1}$ C_3F_8 vapour flow back to the condenser against gravity. Fig. 11 illustrates the sound velocity dependence on air concentration in C_3F_8 vapour at three temperatures of the degassing sonar and a

pressure of $300 \text{ mbar}_{\text{abs}}$. For example, for 0-10 % air contamination in C_3F_8 where the average slope of the velocity/concentration curve is $\sim 0.56 \text{ ms}^{-1}[\% \text{air}]^{-1}$, a sound velocity measurement precision of $\pm 0.05 \text{ ms}^{-1}$ would yield an uncertainty in air concentration of $\pm 0.09 \%$.

During the commissioning of the thermosiphon with C_3F_8 circulation through a dummy load in July 2016 several tests were performed on the degassing sonar. Fig. 12 shows a direct shot taken from the GUI. The variation of air concentration in C_3F_8 and the speed of sound during a condenser cool-down test (July 08-11, 2016) are displayed.

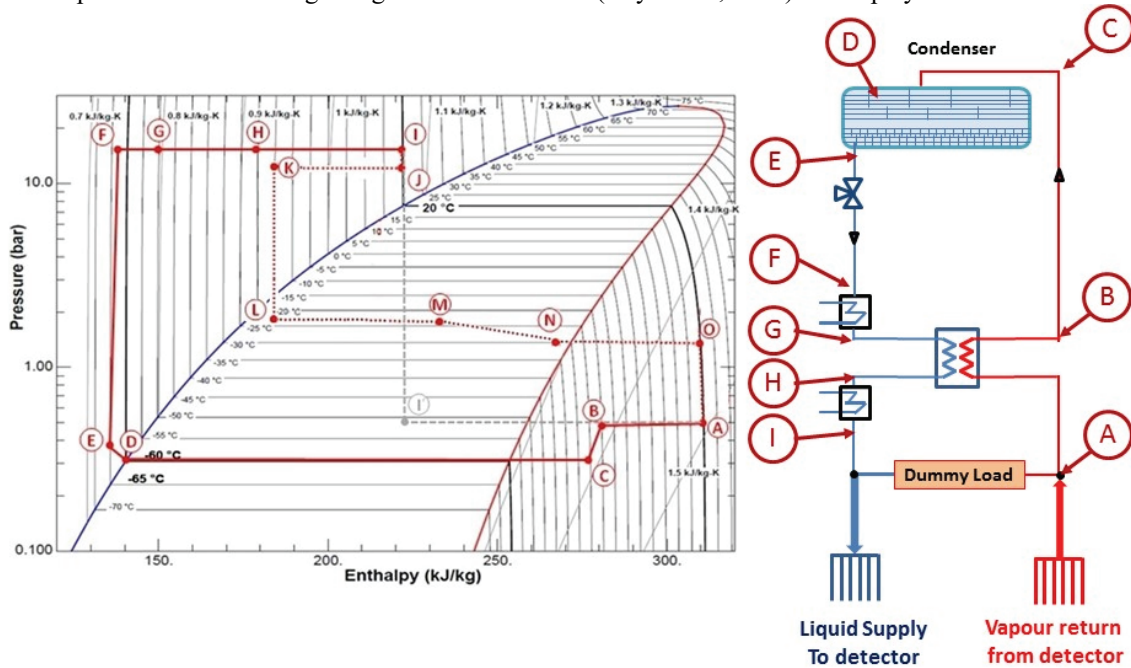


Fig. 10. Schematic and thermodynamic phase diagram of the new thermosiphon cooling system [2].

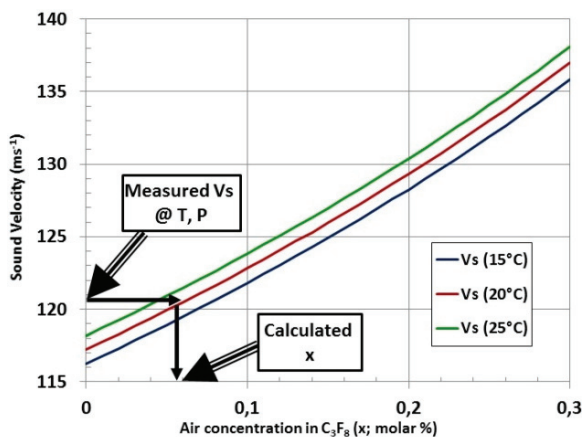


Fig. 11. Sound velocity dependence on air concentration in C_3F_8 vapour at three temperatures of the degassing sonar and a pressure of $300 \text{ mbar}_{\text{abs}}$.

The pressure in the degassing sonar envelope is also shown, which reflects that of the condenser since both volumes are connected. During the test the

condenser temperature was decreased from $-20 \text{ }^\circ\text{C}$ to $-55 \text{ }^\circ\text{C}$ leading to a decrease in the saturated vapour pressure of the C_3F_8 liquid in the condenser. A consequent increase in the speed of sound and apparent air concentration is therefore noticeable. Air is not entering the condenser but the ratio between C_3F_8 vapour and air is changing in the headspace above the C_3F_8 liquid. The regular fluctuations of speed of sound are related to the day/night temperature variation. The rise in apparent air concentration is however not affected by these fluctuations, and is indicative of the robustness of the *air-in- C_3F_8* concentration-finding algorithm.

Fig. 13 illustrates results with the condenser containing liquid C_3F_8 with a starting pressure of $410 \text{ mbar}_{\text{abs}}$.

Around 12.00 on July 12, 2016 20 normal litres of N_2 were injected into the lowest point of the vapour side of the thermosiphon recirculator (around 90 metres below the condenser) to simulate an air ingress. A rise in apparent air concentration of 2.6 % in the vapour seen by the degassing sonar was observed over the next 24 hours as the N_2 gas migrated

through C_3F_8 vapour in the chicane and baffle structure of the condenser toward the degassing sonar. This increase was relative to a baseline level of around

26 % from previous N_2 injections and the unvented accumulation from small leaks encountered and repaired over several weeks of running.

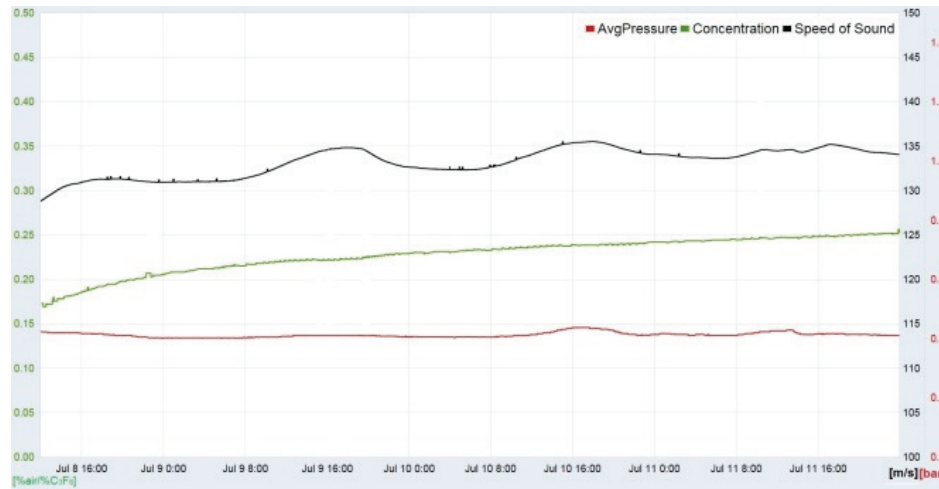


Fig. 12. Variation of concentration and speed of sound during the cool-down test (July 08-11, 2016). Sonar pressure is also shown.

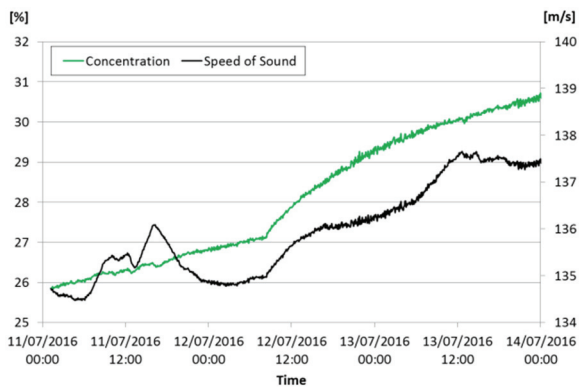


Fig. 13. Effect on concentration (in green), speed of sound (in black), of adding 20 litres of N_2 to the vapour side of the ATLAS thermosiphon system (July 11-14, 2016).

As mentioned above, the main purpose of the degassing sonar is to detect and eliminate air ingress to avoid an increase in the condenser pressure which would reduce the return vapour flow to the condenser. Due to their density difference, N_2 (or air) will accumulate in the headspace of the condenser volume (N_2 : MW = 28, C_3F_8 : MW = 188). If air accumulates in the degassing sonar a sequence of valves is opened to evacuate or “release” it. The results of releasing tests made on July 14, 2016 are shown in Fig. 14. The starting apparent air concentration of 30.6 % is due to the N_2 introduced in previous tests, including those shown in Fig. 12 and Fig. 13. While N_2 is diffusing into the degassing sonar volume, the air concentration is seen to be slightly increasing. In order to remove the N_2 from the condenser, a release of the system is required.

The degassing sonar volume is evacuated and a new mixture from the condenser headspace enters the

sonar. The abrupt increase in concentration corresponds to the entry of additional N_2 from the condenser headspace. Each subsequent release shows a decrease in the measured “air” concentration, confirming that the degassing sonar is working properly by removing the accumulated N_2 . If more releases had been made, the concentration would have continued to decrease.

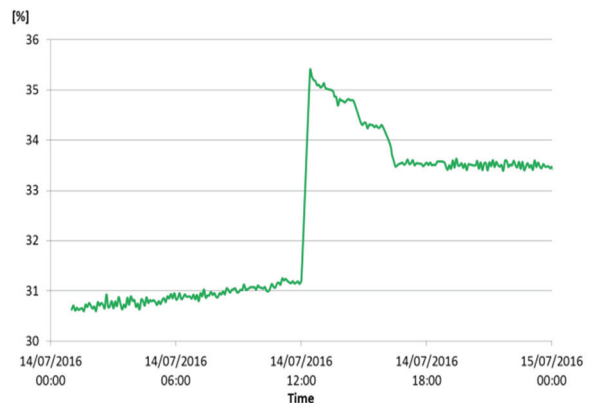


Fig. 14. Measurement of the apparent air concentration in the degassing sonar during the “releasing” tests made on July 14, 2016.

3.2. Angled Flowmeter

The precise measurement of high C_3F_8 vapour return flows (up to $1.2 \text{ m}\cdot\text{s}^{-1}$) to the ATLAS thermosiphon condenser is ensured with a custom angled ultrasonic flowmeter (Fig. 1 and Fig. 15).

The device was constructed in stainless steel with the acoustic path crossing the gas flow at 45° . Quarter

turn ball valves in the acoustic tubes can be closed to allow ultrasonic transducer replacement without interrupting the main gas flow. The instrument has been calibrated against an anemometer in air (Fig. 15) and has demonstrated a flow precision of $\pm 2.3\%$ full scale for flows up to $10.5 \text{ m}\cdot\text{s}^{-1}$ [4]. Operation of the device in high returning flows of C_3F_8 vapour is planned soon.

The difference between the transit times in opposite directions is used to calculate the gas flow rate. In the angled ultrasonic flowmeter the acoustic path segment is at an angle α of 45° to the gas flow, with a “moving gas” length, L , defined as $D_{Main}/\sin\alpha$, where D_{Main} is the diameter of the return gas tube (135 mm). The remaining length of the sound path, L' , is in static gas, and has components L_1 and L_2 on either side of the flow tube (Fig. 16).

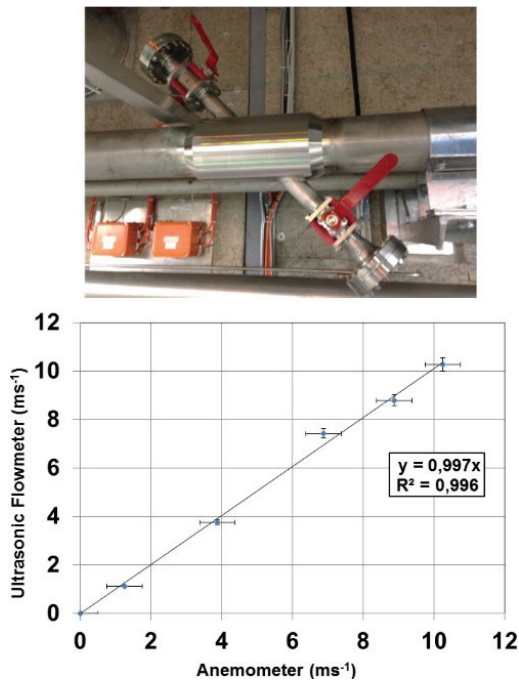


Fig. 15. Calibration in air of the 45° angled ultrasonic flowmeter prior to installation in the ATLAS thermosiphon recirculator (vs. an Amprobe TMA10A anemometer) [4].

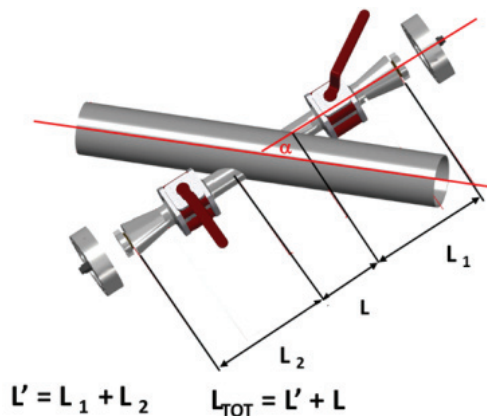


Fig. 16. Geometrical layout of the angled flowmeter.

The gas flow velocity, v_g ($\text{m}\cdot\text{s}^{-1}$), can be calculated using the measured sound velocity, v_s , as

$$v_g = \frac{v_s \left(\frac{D_{Main}}{\sin\alpha} + L' - v_s t_{down} \right)}{\cos\alpha (v_s t_{down} - L')} \quad (9)$$

and

$$v_g = \frac{v_s \left(v_s t_{up} - \frac{D_{Main}}{\sin\alpha} - L' \right)}{\cos\alpha (v_s t_{up} - L')} \quad (10)$$

The sound velocity can be calculated as the physical root of:

$$v_s = \frac{A \pm \sqrt{A^2 - 16L't_{up}t_{down} \left(L' + \frac{D_{Main}}{\sin\alpha} \right)}}{4t_{up}t_{down}} \quad (11)$$

where the definition of A is:

$$A = (t_{up} + t_{down}) \left(2L' + \frac{D_{Main}}{\sin\alpha} \right) \quad (12)$$

The algebra of equations (9)-(12) can be adapted to ultrasonic flowmeters in the other common geometries illustrated in Fig. 17. In each case the total acoustic path length can be expressed as distances, L , in moving gas and L' in static (or closed circulating vortices of) gas. In some cases these lengths are best found in Computational Fluid Dynamics (CFD) calculations. Fig. 18 illustrates such a study made with the OpenFoam® CFD package [10] for a pinched axial flowmeter geometry built by this group [11].

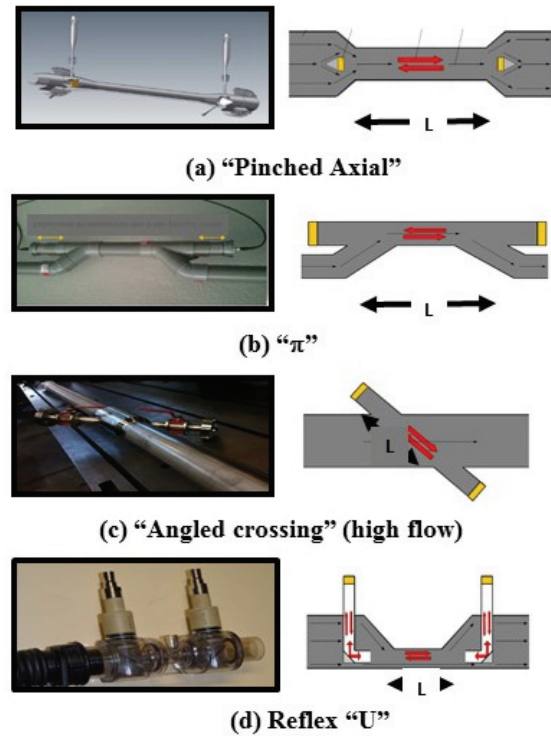


Fig. 17. Illustration of four principal geometries of ultrasonic flowmeters with illustration of the acoustic path segment, L , in uniformly moving gas.

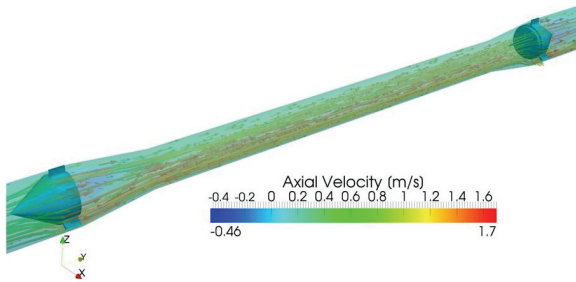


Fig. 18. Stream lines and contours of the axial component of gas flow velocity (ms^{-1}) in a pinched axial geometry flowmeter geometry [11].

4. Measurements in the Triple Sonar Instrumentation

The triple sonar instrumentation (Fig. 1) monitors coolant leaks from the ATLAS SCT, Pixel and IBL silicon tracking subsystems into their separate N_2 -purged anti-humidity envelopes.

Fig. 19 illustrates the change in effective C_3F_8 concentration in the N_2 -purged envelope surrounding the ATLAS Pixel subsystem following the start-up of its C_3F_8 evaporative cooling on January 28, 2016. The sensitivity to molar concentration changes was better than $2 \cdot 10^{-5}$. An increase in C_3F_8 concentration was seen, from $< 5 \cdot 10^{-5}$ to around $1.3 \cdot 10^{-3}$, allowing identification of leaking cooling sub-circuits.

The four zones of the much larger N_2 -purged environmental volume of the ATLAS SCT sub-system are sequentially monitored in a 16-hour supercycle by

aspiration through a single sonar instrument. Sample extraction points (“End-caps “A” & “C”); “Barrel levels” “1” & “7”) are chosen to maximize sensitivity to expected localized hydrostatic pooling of heavy C_3F_8 vapour.

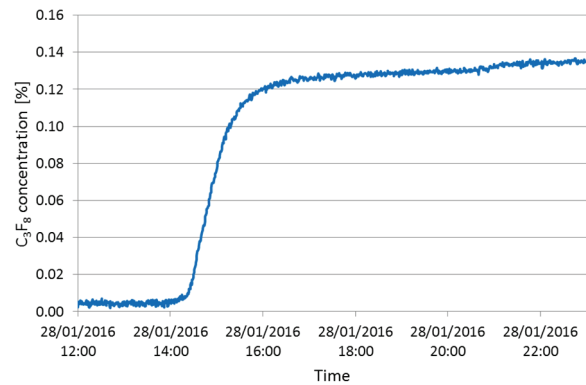


Fig. 19. C_3F_8 concentration sampled from the N_2 -purged volume of the ATLAS Pixel detector before and following cooling system turn-on: January 28, 2016.

Fig. 20 illustrates the apparent C_3F_8 concentration preceding and following the SCT cooling system restart on January 27th 2016. This restart occurred while zone “Barrel 7” was being measured: the sharp spike here is due to the higher evaporation pressure at which the evaporative cooling was initially operated. After the cooling system start-up a significant change in concentration was also visible in zone “Barrel 1”, as in the Pixel detector (Fig. 19).

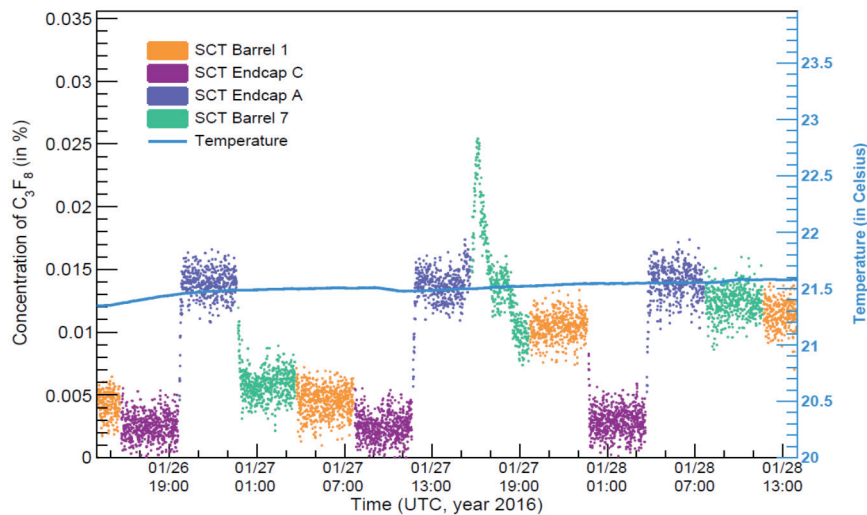


Fig. 20. Increase in the C_3F_8 concentration sampled at four points from the N_2 purged volumes of the SCT detector following turn on of its C_3F_8 evaporative cooling on January 27, 2016 [6].

The sampling sequence continues to “End Cap C”, then to “End Cap A”, then “Barrel level 7”. No significant increase was seen for the zones “Endcap C” and “Endcap A”. In the latter zone, however, there was already a high apparent C_3F_8 concentration due to

known dry air ingress from the ATLAS ID external envelope purge system at this time. Since binary gas analysis is a rapid hypothesis-dependent diagnostic, contamination increases in a heavy “search” gas can be mimicked by higher concentrations of a lighter

contaminant. Warnings given by a continuously-sensitive sonar instrument can however indicate the need for further investigation with more expensive multi-gas sensitive instrumentation, including gas chromatography.

Fig. 21 illustrates the time history of the molar concentration of C_3F_8 coolant leaks into the N_2 environment of the SCT and Pixel sub-detectors over a 4-day period in May 2016.

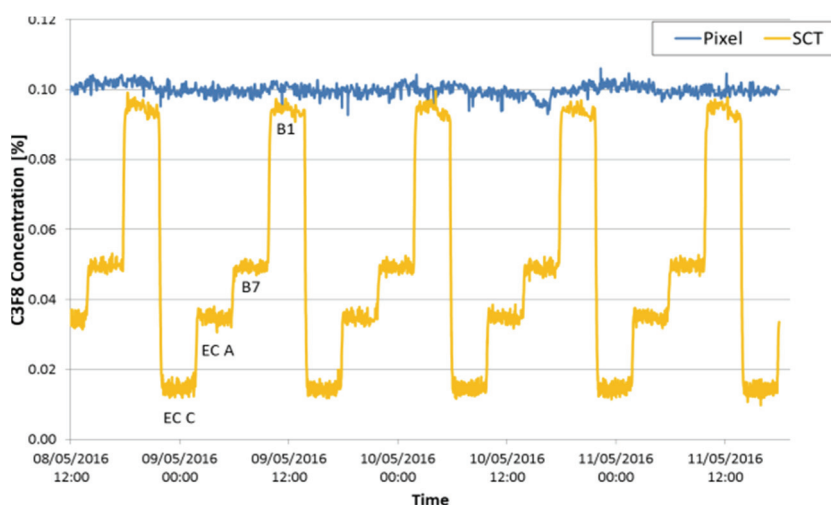


Fig. 21. Variation of the C_3F_8 concentration in the N_2 environment surrounding the ATLAS Pixel and SCT sub-detectors recorded for a period of 4 days in May 2016.

For the SCT, the highest C_3F_8 concentration is seen at the lowest of the points monitoring the SCT N_2 environmental volume (“Barrel level 1”) where more heavy C_3F_8 vapour leaking from the evaporative cooling circuits has had more time to pool after several months of operation. The increased apparent C_3F_8 concentration, particularly in the “Endcap A” zone is also in part due to a change of the ATLAS ID external envelope purge gas from nitrogen to heavier CO_2 .

5. Conclusions

We have developed ultrasonic instruments that have provided high-precision real-time measurements both for flow measurement and binary gas composition analysis.

For binary gas analysis, the precision of mixture determination also depends on the difference between the molecular weights of the two components: the larger the difference the greater the precision. In the case of C_3F_8 (m.w. = 188) leaks into N_2 (m.w. = 28) envelopes of the ATLAS Pixel and SCT silicon tracker subdetectors a mixture precision is $\pm 0.002\%$ was demonstrated for C_3F_8 concentration for the 0 – 0.1% range, of most interest in leak detection.

A pair of ultrasonic instruments is included in the controls of the new ATLAS thermosiphon C_3F_8 evaporative cooling recirculator. Numerous measurements were performed before and during the recent commissioning of the thermosiphon plant. For flow measurement, a precision of $< 2.3\%$ for flows up to $10\text{ m}\cdot\text{s}^{-1}$ was measured in a custom angled flowmeter. Another instrument built to measure air

ingress into a C_3F_8 condenser operating below atmospheric pressure has demonstrated a precision better than 10^{-3} .

References

- [1]. G. Aad, *et al.*, The ATLAS experiment at the CERN Large Hadron Collider, *Journal of Instrumentation*, Vol. 3, August 2008.
- [2]. M. Battistin, *et al.*, The thermosiphon cooling system of the ATLAS experiment at the CERN Large Hadron Collider, *International Journal of Chemical Reactor Engineering*, 2015, pp. 13511–13521.
- [3]. Originally designed by Polaroid® for autofocus cameras: now available and marketed as the SensComp model 600 transducer. <http://www.senscomp.com/ultrasonic-sensors/>
- [4]. R. Bates, *et al.*, A Custom Online Ultrasonic Gas Mixture Analyzer With Simultaneous Flowmetry, Developed for the Upgraded Evaporative Cooling System of the ATLAS Silicon Tracker, *IEEE Transactions on Nuclear Science*, Vol. 61, Issue 4, August 2014, pp. 2059-2065.
- [5]. Lemmon E., Huber M., McLinden M., REFPROP Standard reference database 23, version 9.0, *U.S. National Institute of Standards and Technology*, 2010.
- [6]. <http://mbed.org/platforms/mbed-LPC1768>.
- [7]. C. Rossi, *et al.*, Application of New Ultrasonic Instrumentation to Real-time Monitoring and Analysis of Binary Gases Mixtures, in *Proceedings of the 2nd International Conference on Sensors and Electronic Instrumentation Advances (SEIA' 2016)*, Barcelona, Castelldefels, Spain, 22-23 September 2016, pp. 22-27.
- [8]. <http://w3.siemens.com/mcms/human-machine-interface/en/visualization-software/scada/simatic-wincc/Pages/default.aspx>

- [9]. M. Alhoob, *et al.*, Implementations of Custom Sonar Instruments for Binary Gas Mixture and Flow Analysis in the ATLAS Experiment at the CERN LHC, *IEEE Transactions on Nuclear Science*, Vol. 63, Issue 3, June 2016, pp. 1659–1667.
- [10]. OpenFOAM®, The open source computational fluid dynamics toolbox, version 2.1.0 (2011).
- [11]. R. Bates, *et al.*, A combined ultrasonic flow meter and binary vapour mixture analyzer for the ATLAS silicon tracker, *Journal of Instrumentation*, Vol. 8, Issue 02, 2013, p. 02006.



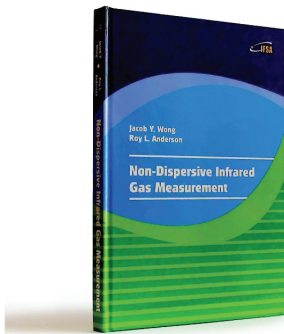
Published by International Frequency Sensor Association (IFSA) Publishing, S. L., 2016 (<http://www.sensorsportal.com>).



International Frequency Sensor Association (IFSA) Publishing

Jacob Y. Wong, Roy L. Anderson

Non-Dispersive Infrared Gas Measurement



Formats: printable pdf (Acrobat) and print (hardcover), 120 pages

ISBN: 978-84-615-9732-1,
e-ISBN: 978-84-615-9512-9

Written by experts in the field, the *Non-Dispersive Infrared Gas Measurement* begins with a brief survey of various gas measurement techniques and continues with fundamental aspects and cutting-edge progress in NDIR gas sensors in their historical development.

- It addresses various fields, including:
- Interactive and non-interactive gas sensors
- Non-dispersive infrared gas sensors' components
- Single- and Double beam designs
- Historical background and today's of NDIR gas measurements

Providing sufficient background information and details, the book *Non-Dispersive Infrared Gas Measurement* is an excellent resource for advanced level undergraduate and graduate students as well as researchers, instrumentation engineers, applied physicists, chemists, material scientists in gas, chemical, biological, and medical sensors to have a comprehensive understanding of the development of non-dispersive infrared gas sensors and the trends for the future investigation.

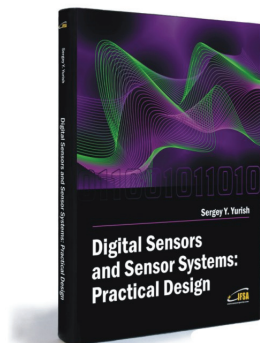
http://sensorsportal.com/HTML/BOOKSTORE/NDIR_Gas_Measurement.htm



International Frequency Sensor Association (IFSA) Publishing

Digital Sensors and Sensor Systems: Practical Design

Sergey Y. Yurish



Formats: printable pdf (Acrobat) and print (hardcover), 419 pages

ISBN: 978-84-616-0652-8,
e-ISBN: 978-84-615-6957-1

The goal of this book is to help the practitioners achieve the best metrological and technical performances of digital sensors and sensor systems at low cost, and significantly to reduce time-to-market. It should be also useful for students, lectures and professors to provide a solid background of the novel concepts and design approach.

Book features include:

- Each of chapter can be used independently and contains its own detailed list of references
- Easy-to-repeat experiments
- Practical orientation
- Dozens examples of various complete sensors and sensor systems for physical and chemical, electrical and non-electrical values
- Detailed description of technology driven and coming alternative to the ADC a frequency (time)-to-digital conversion

Digital Sensors and Sensor Systems: Practical Design will greatly benefit undergraduate and at PhD students, engineers, scientists and researchers in both industry and academia. It is especially suited as a reference guide for practitioners, working for Original Equipment Manufacturers (OEM) electronics market (electronics/hardware), sensor industry, and using commercial-off-the-shelf components

http://sensorsportal.com/HTML/BOOKSTORE/Digital_Sensors.htm

Study of Virtual Body Frames in Dodecahedron-Based Skew Redundant Inertial Measurement Units

Marius V. GHEORGHE

Ideal Aerosmith Inc., 2205 W Lone Cactus Dr., Ste. 7, Phoenix, AZ, 85027, USA

Tel.: +1.623.847.8933, fax: +1.623.587.5863

E-mail: mgheorghe@idealaero.com

Received: 5 November 2016 / Accepted: 5 December 2016 / Published: 30 December 2016

Abstract: Dodecahedron-based skew redundant inertial measurement units are one of the favored configurations employed in high-reliability inertial navigation applications. In its classical configuration, where the XYZ body axes bisect the angles between pairs of sensors, the dodecahedron-based skew redundant inertial measurement unit poses disadvantages from a packaging perspective. At least two United States patents that provide mechanical packaging solutions to this problem exist, however both solutions suffer from some drawbacks. Alternate body frames that favor a more compact mechanical packaging are possible, however they may negatively impact the mathematical model and computation of the parity vectors. This paper aims to offer an original solution, based on a virtual body frame that allows both an efficient mechanical packaging and ease of computation for the parity vectors. Furthermore, the properties of the proposed virtual body frame are studied and compared to those of the real body frame with the end goal of assessing the performance of the skew redundant inertial measurement unit in its final configuration.

Keywords: Virtual body frame, Skew redundant, IMU, SRIMU.

1. Introduction

The dodecahedron-based skew redundant measurement unit (SRIMU) is one of the favored configurations employed in high-reliability inertial navigation applications. In its classical configuration, the $X_2Y_2Z_2$ body axes bisect the angles between pairs of sensors as shown in Fig. 1.

As shown in prior art, this configuration poses some advantages, such as balanced shape matrix [1] resulting in a higher figure of merit [2] than other orientations, ease of computation for the parity vectors [3] and improved end of life performance [4].

However, as noted in [1] and [2] the classical configuration is less than optimal from a mechanical packaging perspective. Various attempts have been

made to improve the packaging while retaining the classical body frame.

For example, in [5], the author relies on sensors that have specially rotated sensing axes, mounted on a rectangular prism block. However, modern, high-performance gyroscopes and accelerometers, such as [6] and [7], have shapes that are not conducive to such packaging. Even with the specially oriented sensing axes, the packaging is not optimal.

An improved packaging that relies on the classical body frame is addressed in [8]. In this case the packaging trades its compactness for the fact that the sensing axes of the accelerometers and gyroscopes do not intersect in the center of the dodecahedron.

This paper will explore the usage of a virtual body frame in conjunction with a reduced volume SRIMU.

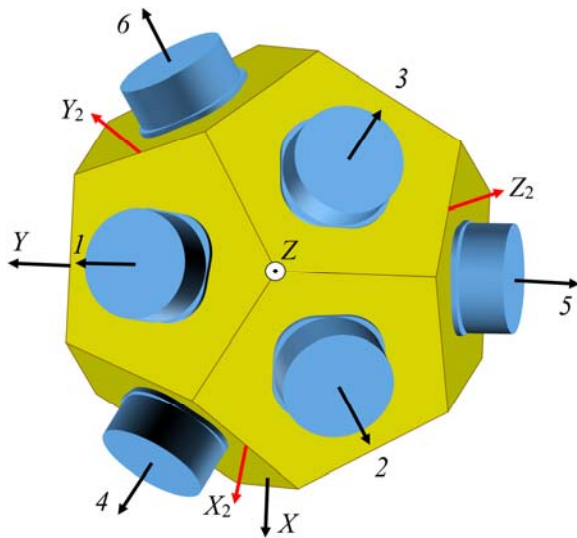


Fig. 1. Classical dodecahedron SRIMU body frame.

2. Reduced Volume SRIMU

A reduced volume notional SRIMU was suggested in [1] and was included here for reference (see Fig. 2). In this concept the dodecahedron was truncated and hollowed to reduce its volume and mass, and its body frame was rotated such that the XY plane is parallel to the truncated SRIMU base. In Fig. 2 the rotated body frame XYZ is identified as the real body frame while the classical frame $X_2Y_2Z_2$ is identified as the virtual body frame.

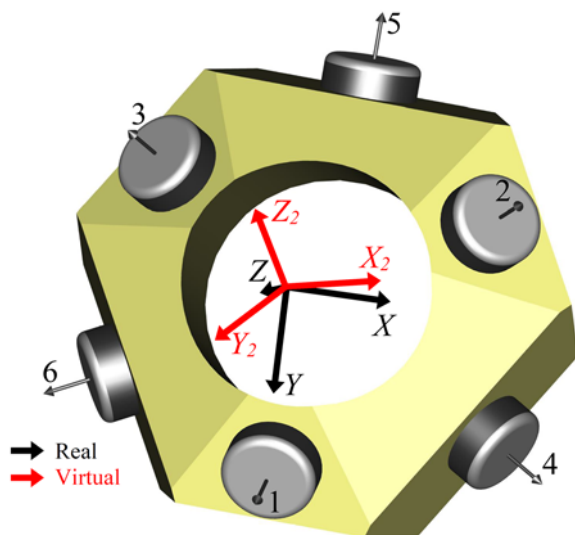


Fig. 2. Reduced volume SRIMU concept.

In Fig. 2 only six notional sensors are shown, however for each such notional sensor there is a gyroscope/accelerometer pair which can be mounted coaxially, like the mounting used in [8], such that their sensing axes are collinear. A suggested such mounting for the Emcore EMP-1.2K fiber optic gyroscope [6] and the Honeywell Q-Flex® QA-750 accelerometer

[7] is shown in Fig. 3. These devices were selected for illustration only and no representation is attempted with regards to the final performance of the resulting SRIMU.

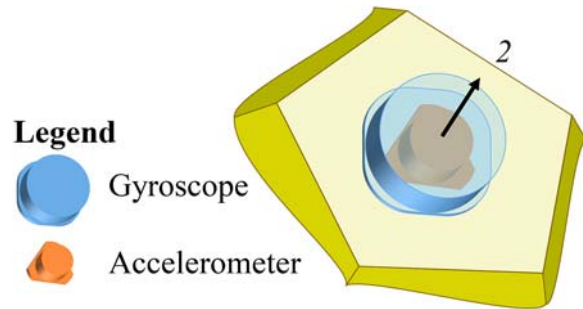


Fig. 3. Illustration of coaxial mounting of gyroscopes and accelerometers.

If the gyroscope/accelerometer pairs are kept in the center of the pentagons while the dodecahedron truncation and hollowing take place, all sensing axes intersect in the center of the dodecahedron.

If it is acceptable to have more than one inertial center for the SRIMU assembly, like in [8], then a further reduction of the assembly volume can be achieved. Positioning the gyroscope/accelerometer pairs off-center on the surfaces of the dodecahedron allows a more aggressive dodecahedron truncation and hollowing to take place, therefore further reducing the resulting volume and mass.

3. Body Frames

The SRIMU shape matrix H for the real body frame selected in [1] and illustrated as XYZ in Fig. 1 is shown below:

$$H = \begin{bmatrix} 0 & \sqrt{\frac{10-2\sqrt{5}}{15}} & \sqrt{\frac{5+2\sqrt{5}}{15}} \\ \sqrt{\frac{5-\sqrt{5}}{10}} & -\sqrt{\frac{5-\sqrt{5}}{30}} & \sqrt{\frac{5+2\sqrt{5}}{15}} \\ -\sqrt{\frac{5-\sqrt{5}}{10}} & -\sqrt{\frac{5-\sqrt{5}}{30}} & \sqrt{\frac{5+2\sqrt{5}}{15}} \\ \sqrt{\frac{5+\sqrt{5}}{10}} & \sqrt{\frac{5+\sqrt{5}}{30}} & \sqrt{\frac{5-2\sqrt{5}}{15}} \\ 0 & -\sqrt{\frac{10+2\sqrt{5}}{15}} & \sqrt{\frac{5-2\sqrt{5}}{15}} \\ -\sqrt{\frac{5+\sqrt{5}}{10}} & \sqrt{\frac{5+\sqrt{5}}{30}} & \sqrt{\frac{5-2\sqrt{5}}{15}} \end{bmatrix} \quad (1)$$

This matrix reflects the orientation of the Z axis pointing out of the vertex defined by the dodecahedron faces 1, 2, and 3. No special consideration was given up to this point to the orientation of axes X , and Y other than their plane is parallel to the base of the SRIMU.

By contrast, the shape matrix H_2 for the body frame illustrated as $X_2Y_2Z_2$ in Fig. 1 is shown in (2).

This matrix is widely used in literature and reflects the general acceptance of the classical body frame $X_2Y_2Z_2$ in the vast majority of dodecahedron-based SRIMU studies.

$$H_2 = \begin{bmatrix} \sqrt{\frac{5+\sqrt{5}}{10}} & 0 & \sqrt{\frac{5-\sqrt{5}}{10}} \\ -\sqrt{\frac{5+\sqrt{5}}{10}} & 0 & \sqrt{\frac{5-\sqrt{5}}{10}} \\ \sqrt{\frac{5-\sqrt{5}}{10}} & \sqrt{\frac{5+\sqrt{5}}{10}} & 0 \\ \sqrt{\frac{5-\sqrt{5}}{10}} & -\sqrt{\frac{5+\sqrt{5}}{10}} & 0 \\ 0 & \sqrt{\frac{5-\sqrt{5}}{10}} & \sqrt{\frac{5+\sqrt{5}}{10}} \\ 0 & \sqrt{\frac{5-\sqrt{5}}{10}} & -\sqrt{\frac{5+\sqrt{5}}{10}} \end{bmatrix} \quad (2)$$

4. Fault Detection and Isolation

Fault detection and isolation in SRIMUs often relies on parity vectors. Various techniques for determining parity vectors have been developed, however they generally rely on invariants that are violated when sensor faults occur.

For example, in [9] and [10], parity vectors are determined using null spaces, called *left null spaces* in [9] and *parity matrices* in [10].

In [11] the authors use an algorithm based on the singular value decomposition (SVD) while in [12] and [13] the authors rely on simple arithmetic expressions.

The approach used in [12] and [13] is attractive due to its small computational burden, and motivated the idea of using a virtual body frame. Therefore, this approach is explored in the following paragraphs.

From Fig. 4 it can be observed that axis X_2 is coplanar with the sensing axes of Sensors 2 and 4, axis Y_2 is coplanar with the sensing axes of Sensors 1 and 6, and axis Z_2 is coplanar with the sensing axes of Sensors 3 and 5.

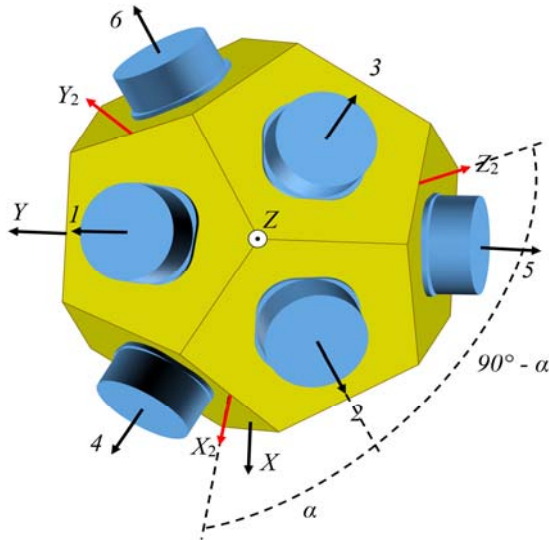


Fig. 4. Relation between sensing axes and virtual body frame.

Furthermore, each body frame axis gets contributions from four different sensors, as it can be seen in (2). This property of the dodecahedron configuration guarantees the redundancy for this type of SRIMU.

The dodecahedron dihedral angle is:

$$\beta = \cos^{-1} \left(-\frac{1}{\sqrt{5}} \right) \approx 116.57^\circ \quad (3)$$

Therefore, the angle between each one of the sensors in a pair and the corresponding axis is:

$$\alpha = \frac{180^\circ - \beta}{2} = 90^\circ - \frac{1}{2} \cos^{-1} \left(\frac{1}{\sqrt{5}} \right) \approx 31.72^\circ \quad (4)$$

The relevant trigonometric functions of α are:

$$\sin \alpha = \sqrt{\frac{5-\sqrt{5}}{10}} \approx 0.5257 \quad (5)$$

$$\cos \alpha = \sqrt{\frac{5+\sqrt{5}}{10}} \approx 0.8507 \quad (6)$$

These values also appear repeated in various positions in (2).

Fig. 4 shows the relation between the sensing axis 2 and the X_2 and Z_2 virtual body frame axes. Similar relations exist between other sensor sensing axes and the virtual body frame axes. These relations are captured in analytical form in (7) for the accelerations with the mention that the same relations exist for the rates as well.

$$\begin{aligned} \tilde{a}_1 &= a_{Y_2} \cos \alpha + a_{X_2} \sin \alpha \\ \tilde{a}_2 &= a_{X_2} \cos \alpha + a_{Z_2} \sin \alpha \\ \tilde{a}_3 &= a_{Z_2} \cos \alpha + a_{Y_2} \sin \alpha \\ \tilde{a}_4 &= a_{X_2} \cos \alpha - a_{Z_2} \sin \alpha \\ \tilde{a}_5 &= a_{Z_2} \cos \alpha - a_{Y_2} \sin \alpha \\ \tilde{a}_6 &= a_{Y_2} \cos \alpha - a_{X_2} \sin \alpha, \end{aligned} \quad (7)$$

where \tilde{a}_i represent the nominal outputs of sensors $i = 1 \dots 6$; a_{X_2} , a_{Y_2} and a_{Z_2} represent the accelerations (or rates) in the virtual body frame axes X_2 , Y_2 and Z_2 ; and $\sin \alpha$ and $\cos \alpha$ are the trigonometric functions defined in (5) and (6), respectively.

In [10], the author explains that the linear dependence of the sensors in a redundant configuration allows the output of any sensor to be reconstructed from the outputs of other sensors. This property allows the construction of expressions that should evaluate to zero or, more realistically, almost zero, when all sensors are working properly.

Starting from the observation stated above and using (7), we can derive the ${}^6C_4 = 15$ relations in (8a) and (8b) that can be used as parity vectors:

$$\begin{aligned} p_{1234} &= (\tilde{a}_1 + \tilde{a}_2) \sin \alpha - (\tilde{a}_3 + \tilde{a}_4) \cos \alpha \approx 0 \\ p_{1235} &= (\tilde{a}_2 + \tilde{a}_3) \sin \alpha - (\tilde{a}_1 + \tilde{a}_5) \cos \alpha \approx 0 \\ p_{1236} &= (\tilde{a}_1 + \tilde{a}_3) \sin \alpha - (\tilde{a}_2 + \tilde{a}_6) \cos \alpha \approx 0 \\ p_{1245} &= -(\tilde{a}_1 + \tilde{a}_4) \sin \alpha + (\tilde{a}_2 - \tilde{a}_5) \cos \alpha \approx 0 \\ p_{1246} &= -(\tilde{a}_2 + \tilde{a}_4) \sin \alpha + (\tilde{a}_1 - \tilde{a}_6) \cos \alpha \approx 0 \\ p_{1256} &= (\tilde{a}_5 - \tilde{a}_6) \sin \alpha + (\tilde{a}_1 - \tilde{a}_2) \cos \alpha \approx 0 \end{aligned} \quad (8a)$$

$$\begin{aligned}
 p_{1256} &= (\tilde{a}_5 - \tilde{a}_6) \sin \alpha + (\tilde{a}_1 - \tilde{a}_2) \cos \alpha \approx 0 \\
 p_{1345} &= (\tilde{a}_4 - \tilde{a}_5) \sin \alpha - (\tilde{a}_1 - \tilde{a}_3) \cos \alpha \approx 0 \\
 p_{1346} &= -(\tilde{a}_3 + \tilde{a}_6) \sin \alpha + (\tilde{a}_1 - \tilde{a}_4) \cos \alpha \approx 0 \\
 p_{1356} &= -(\tilde{a}_1 + \tilde{a}_6) \sin \alpha + (\tilde{a}_3 - \tilde{a}_5) \cos \alpha \approx 0 \\
 p_{1456} &= (\tilde{a}_1 - \tilde{a}_5) \sin \alpha - (\tilde{a}_4 + \tilde{a}_6) \cos \alpha \approx 0 \\
 p_{2345} &= -(\tilde{a}_3 + \tilde{a}_5) \sin \alpha + (\tilde{a}_2 - \tilde{a}_4) \cos \alpha \approx 0 \\
 p_{2346} &= (\tilde{a}_4 - \tilde{a}_6) \sin \alpha - (\tilde{a}_2 - \tilde{a}_3) \cos \alpha \approx 0 \\
 p_{2356} &= -(\tilde{a}_2 + \tilde{a}_5) \sin \alpha + (\tilde{a}_3 - \tilde{a}_6) \cos \alpha \approx 0 \\
 p_{2456} &= (\tilde{a}_2 - \tilde{a}_6) \sin \alpha - (\tilde{a}_4 + \tilde{a}_5) \cos \alpha \approx 0 \\
 p_{3456} &= (\tilde{a}_3 - \tilde{a}_4) \sin \alpha - (\tilde{a}_5 + \tilde{a}_6) \cos \alpha \approx 0,
 \end{aligned} \tag{8b}$$

where p_{ijkl} represent the parity equations; \tilde{a}_i represent the ideal outputs of sensors $i = 1 \dots 6$; and $\sin \alpha$ and $\cos \alpha$ are the trigonometric functions defined in (5) and (6), respectively.

However, in a real application the values $\tilde{a}_1 - \tilde{a}_6$ are not known. Instead, the corrected sensor outputs $\hat{a}_1 - \hat{a}_6$, are used in equation (8a) and (8b) to compute the parity vectors. The corrected sensor outputs can be obtained as shown further in this section.

Since α is fixed and known, the parity vectors (8a) and (8b) can be computed using just elementary mathematical operations (addition, subtraction, and multiplication).

It can be seen in (8a) and (8b) that each corrected sensor reading is employed in ten different expressions. Therefore, if a sensor fails it will cause all those expressions to yield values above the threshold, signaling the failure condition.

Discriminating which sensor has failed can be performed using the bitwise AND function over the binary masks shown in Table 1.

Table 1. Suggested binary masks for fault isolation.

| Parity Vector p_{ijkl} | Mask for $ p_{ijkl} < \varepsilon$ | Mask for $ p_{ijkl} > \varepsilon$ |
|--------------------------|-------------------------------------|-------------------------------------|
| p_{1234} | FF ₁₆ | * 0F ₁₆ |
| p_{1235} | FF ₁₆ | 17 ₁₆ |
| p_{1236} | FF ₁₆ | 27 ₁₆ |
| p_{1245} | FF ₁₆ | * 1B ₁₆ |
| p_{1246} | FF ₁₆ | * 2B ₁₆ |
| p_{1256} | FF ₁₆ | 33 ₁₆ |
| p_{1345} | FF ₁₆ | * 1D ₁₆ |
| p_{1346} | FF ₁₆ | * 2D ₁₆ |
| p_{1356} | FF ₁₆ | 35 ₁₆ |
| p_{1456} | FF ₁₆ | * 39 ₁₆ |
| p_{2345} | FF ₁₆ | * 1E ₁₆ |
| p_{2346} | FF ₁₆ | * 2E ₁₆ |
| p_{2356} | FF ₁₆ | 36 ₁₆ |
| p_{2456} | FF ₁₆ | * 3A ₁₆ |
| p_{3456} | FF ₁₆ | * 3C ₁₆ |

For example, if Sensor 4 fails, it will cause the parity vectors using \hat{a}_4 to be greater than the threshold ε . The corresponding masks are marked with * (asterisk) in Table 1. Therefore, the bitwise AND of all these masks will yield 08₁₆:

$$\begin{aligned}
 &0F_{16} \wedge FF_{16} \wedge FF_{16} \wedge 1B_{16} \wedge 2B_{16} \wedge \\
 &1D_{16} \wedge 2D_{16} \wedge FF_{16} \wedge 39_{16} \wedge 1E_{16} \wedge \\
 &FF_{16} \wedge 2E_{16} \wedge FF_{16} \wedge 3A_{16} \wedge 3C_{16} = 08_{16},
 \end{aligned} \tag{9}$$

where pq_{16} , with $p, q = 1 \dots F$ represent hexadecimal digits; and \wedge is the bitwise AND operator.

Per Table 2, the right-hand side value from (9) identifies Sensor 4 as being faulty.

Table 2. Binary masks for sensor identification.

| Sensor | Sensor Mask |
|--------|------------------|
| 1 | 01 ₁₆ |
| 2 | 02 ₁₆ |
| 3 | 04 ₁₆ |
| 4 | 08 ₁₆ |
| 5 | 10 ₁₆ |
| 6 | 20 ₁₆ |

The corrected sensor outputs $\hat{a}_1 - \hat{a}_6$, can be obtained from the raw sensor outputs by performing sensor frame corrections, for example using the sensor frame correction method described in [1]:

$$\hat{\mathbf{A}}_{SX} = \left(\mathbf{H}_{SX}^T \mathbf{H}_{SX} \right)^{-1} \mathbf{H}_{SX}^T \mathbf{A}_{SX}, \tag{10}$$

where $\hat{\mathbf{A}}_{SX}$ (11) is the extended vector of corrected sensor readings; \mathbf{H}_{SX} (12) is the extended sensor frame shape matrix; and \mathbf{A}_{SX} (13) is the extended vector of raw sensor readings.

$$\hat{\mathbf{A}}_{SX} = [\hat{a}_1 \ \hat{a}_2 \ \dots \ \hat{a}_6 \ 1]^T = \begin{bmatrix} \hat{\mathbf{A}}_S \\ 1 \end{bmatrix}, \tag{11}$$

where $\hat{a}_i, i = 1 \dots 6$, are the corrected sensor readings.

$$\mathbf{H}_{SX} = \begin{bmatrix} h_{11} & h_{21} & \dots & h_{61} & b_1 \\ h_{12} & h_{22} & \dots & h_{62} & b_2 \\ \dots & \dots & \dots & \dots & \dots \\ h_{16} & h_{26} & \dots & h_{66} & b_6 \\ 0 & 0 & \dots & 0 & 1 \end{bmatrix}, \tag{12}$$

where $h_{ij}, i, j = 1 \dots 6$, are the sensor frame correction coefficients; and $b_i, i = 1 \dots 6$ are the sensor biases.

$$\mathbf{A}_{SX} = [a_1 \ a_2 \ \dots \ a_6 \ 1]^T = \begin{bmatrix} \mathbf{A}_S \\ 1 \end{bmatrix} \tag{13}$$

where $a_i, i = 1 \dots 6$, are the raw sensor readings.

The accelerations or rates in the virtual body frame are obtained with the following equation:

$$\mathbf{A}_{B2} = \left(\mathbf{H}_2^T \mathbf{S}_e \mathbf{H}_2 \right)^{-1} \mathbf{H}_2^T \mathbf{S}_e \hat{\mathbf{A}}_S, \tag{14}$$

where \mathbf{A}_{B2} (15) is the vector with the virtual body frame accelerations or rates $a_{i2}, i = X, Y, Z$; \mathbf{H}_2 (2) is the virtual body frame shape matrix; \mathbf{S}_e (16) is a steering diagonal matrix with elements $s_i = 1$ for a good sensor and $s_i = 0$ for a faulty sensor, and with index $e = 1, 2, \dots, 6$ denoting a one-sensor fault, $e = 12, 13, \dots, 56$ denoting a two-sensor fault, and $e = 123, 124, \dots, 456$ denoting a three-sensor fault; and

\hat{A}_S is the subset of \hat{A}_{SX} (13) containing just the corrected sensor readings.

$$A_{B2} = [a_{X2} \ a_{Y2} \ a_{Z2}]^T \quad (15)$$

$$S_e = \begin{bmatrix} s_1 & 0 & 0 & 0 & 0 & 0 \\ 0 & s_2 & 0 & 0 & 0 & 0 \\ 0 & 0 & s_3 & 0 & 0 & 0 \\ 0 & 0 & 0 & s_4 & 0 & 0 \\ 0 & 0 & 0 & 0 & s_5 & 0 \\ 0 & 0 & 0 & 0 & 0 & s_6 \end{bmatrix} \quad (16)$$

Similarly, the accelerations or rates in the real body frame are obtained with:

$$A_B = (H^T S_e H)^{-1} H^T S_e \hat{A}_S, \quad (17)$$

where A_B (18) is the vector with the real body frame accelerations or rates a_i , $i = X, Y, Z$; H (1) is the virtual body frame shape matrix; S_e (16) is a steering diagonal matrix; and \hat{A}_S is the subset of \hat{A}_{SX} (13) containing just the corrected sensor readings.

$$A_B = [a_X \ a_Y \ a_Z]^T \quad (18)$$

5. Performance Factors

In [2] and [4] the authors mention the determinant of the information matrix as being one of the performance factors that can be used for evaluating the performance of SRIMUs. The information matrix for the virtual body frame is shown below:

$$M_2 = H_2^T H_2, \quad (19)$$

where H_2 is defined in (2).

Similarly, the information matrix for the real body frame is shown in (20).

$$M = H^T H, \quad (20)$$

where H is defined in (1).

The information matrices are deemed to contain *more* information if their determinants have higher values. As faults are introduced, the determinant values are expected to become smaller.

To evaluate the determinant of the information matrix in the presence of faults, we need to find the equivalent information matrix for (14) and (17) when S_e has one or more diagonal elements equal to 0.

For this, we introduce two helper matrices:

$$h_{2e} = (H_2^T S_e H_2)^{-1} H_2^T S_e \quad (21)$$

$$h_e = (H^T S_e H)^{-1} H^T S_e, \quad (22)$$

where h_e and h_{2e} are the helper matrices, with $e = 1, 2, \dots, 6$ for one-sensor faults, $e = 12, 13, \dots, 56$ for two-sensor faults, and $e = 123, 124, \dots, 456$ for three-sensor faults; S_e is the steering matrix with the e diagonal element(s) zeroed out; and H (1) and H_2 (2) are the shape matrices.

Using the h_e and h_{2e} helper matrices, we define the equivalents of H and H_2 in the presence of sensor faults:

$$H_{2e} = \left((h_{2e} h_{2e}^T)^{-1} h_{2e} \right)^T \quad (23)$$

$$H_e = \left((h_e h_e^T)^{-1} h_e \right)^T \quad (24)$$

Having H_e and H_{2e} , we can compute the equivalent information matrices in the presence of faults:

$$M_{2e} = H_{2e}^T H_{2e} \quad (25)$$

$$M_e = H_e^T H_e \quad (26)$$

The worst case determinant values for the equivalent information matrices M_{2e} and M_e are listed in Table 3. Based on these values, no performance degradation occurs in the real body frame versus the virtual body frame.

In [4] the authors suggest that another method of measuring the performance of the SRIMU in the presence of faults is by observing the minimum eigenvalue of the information matrix. The worst case minimum eigenvalues are listed in Table 4. No performance degradation is observed in the real body frame with this performance evaluation either.

Table 3. Worst case determinant values of information matrices.

| Sensor Faults | det(M_{2e}) | det(M_e) |
|---------------|-----------------|--------------|
| 0 | 8 | 8 |
| 1 | 4 | 4 |
| 2 | 1.6 | 1.6 |
| 3 | 0.221115 | 0.221115 |

Table 4. Worst case eigenvalues of information matrices.

| Sensor Faults | min(spec(M_{2e})) | min(spec(M_e)) |
|---------------|-----------------------|--------------------|
| 0 | 2 | 2 |
| 1 | 1 | 1 |
| 2 | 0.552786 | 0.552786 |
| 3 | 0.105573 | 0.105573 |

6. Future Work

The fault isolation approach described in Section 5, is not analyzed in depth in this paper. Therefore, one topic for future work would be a study of its suitability for multiple sensor failures and for real-life applications (i.e. selection criteria for ϵ).

In Section 2, the real body frame was selected such that the XY plane was parallel to the base of the truncated SRIMU. However, no consideration was given to the orientation of X and Y with regards to the

sensor frame. It is possible that a more balanced H shape matrix can be achieved by inducing a further rotation about the Z axis. However, the study on finding the optimal rotation angle, if such an angle axis exists, is also left for future work.

9. Conclusions

Dodecahedron-based SRIMUs have properties that make them attractive in high-reliability inertial navigation environments. However, the classical body reference frame (herein referenced as the virtual body frame) imposes packaging challenges, primarily because Sensors 1 and 4 are located below the X_2Y_2 plane (see Fig. 4). This generally causes the SRIMU assembly to be raised and to result in a higher volume and mass.

The possibility of using a flattened assembly structure, obtained by rotating the original body frame, and the usage of an associated virtual body frame were introduced in [1], however the analysis of these concepts was left for future work.

The first original contribution of this paper is that the virtual body frame was leveraged to perform the low-burden computations of the parity vector used in fault detection. A transformation from the virtual body frame to the real body frame was also provided for convenience.

A second original contribution consisted in a novel low-computational burden method of performing the fault isolation by means of bitwise AND operations. This method supplements the low-computational burden fault detection mentioned above. The proposed fault isolation method is appropriate for the isolation of single faults in the current embodiment with further expansion to the isolation of multiple faults left for future work.

Finally, the performance of the real body frame was compared against the performance of the virtual body frame by means of two accepted methods: the determinant of the information matrix and the eigenvalues of the information matrix. No performance degradation was found using these two methods and it was left to future work to determine if other metrics are more appropriate and whether an optimal body frame can be found.

Acknowledgements

Many thanks to Ideal Aeromsmith Inc., <http://www.ideal-aeromsmith.com>, for facilitating the

studies that led to the development of this paper, Mr. Jim RICHTSMEIER for reviewing the abstract and full-length papers, Mr. Dustan LARSON for reviewing early work that led to this paper and to Ms. Jennifer STORM and Mr. Bryon BISCHOFF for preparing and consulting on the SRIMU 3D CAD model, respectively.

References

- [1]. M. V. Gheorghe, Calibration Techniques for Skew Redundant Inertial Measurement Units, in *Proceedings of the 2nd International Conference on Sensors Engineering and Electronics Instrumental Advances (SELA'16)*, Barcelona, Castelldefels, Spain, 22-23 September 2016, pp. 72-78.
- [2]. L. Fu, X. Yang, L. L. Wang, A Novel Optimal Redundant Inertial Sensor Configuration in Strapdown Inertial Navigation System, in *Proceedings of the IEEE/ION Position Location and Navigation Symposium (PLANS)*, 2012, pp. 240-246.
- [3]. J. P. Gilmore, R. A. McKern, A Redundant Strapdown Inertial Reference Unit (SIRU), *Journal of Spacecraft*, Vol. 9, No. 1, Jan. 1972, pp. 39-47.
- [4]. P. K. Mazaika, Orientation of Measurement Sensors for Optimum End-of-Life Performance, *IEEE Transactions on Aerospace and Electronic Systems*, Vol. AES-17, No. 2, Mar. 1981, pp. 281-287.
- [5]. M. Epstein, Redundant Inertial Measurement System Configuration, *US Patent 4 020 702*, 3 May 1977.
- [6]. Emcore Corp., EMP-1.2K Lithium-Niobate Fiber Optic Gyroscope (FOG), Datasheet, Jan. 2016.
- [7]. Q-Flex® QA-750 Accelerometer, Datasheet, *Honeywell*, 2005.
- [8]. L. E. Joly, M. A. Knipfer, M. J. Miller, G. O. Nitzchke, M. T. Weinberger, Skewed Axis Inertial Sensor Assembly, *US Patent 5 363 700*, 15 Nov. 1994.
- [9]. M. Basseville, I. Nikiforov, Fault isolation for diagnosis: nuisance rejection and multiple hypotheses testing, *Annual Reviews in Control*, Vol. 26, Issue 2, 2002, pp. 189-202.
- [10]. F. E. DeAngelis, A Threshold Redundancy Management Algorithm for Skewed Sensor Arrays, in *Proceedings of the IEEE/AIAA/NASA 9th Conference Digital Avionics Systems*, 1990, pp. 133-140.
- [11]. D. S. Shim, C. K. Yang, Geometric FDI based on SVD for Redundant Inertial Sensor Systems, in *Proceedings of the 5th Asian Control Conference*, Vol. 2, 2004, pp. 1094-1100.
- [12]. J. P. Gilmore, R. J. Cooper, SIRU Development, Final Report, *Massachusetts Institute of Technology*, Vol. 1, 1973.
- [13]. S. Sun, R. Liu, Error Calibration and FDI Technology of Gyros in Redundant IMU, in *Proceedings of the First International Workshop on Database Technology and Applications*, 2009, pp. 398-401.



Ultra-fast Sensor for Single-photon Detection in a Wide Range of the Electromagnetic Spectrum

* **Astghik KUZANYAN, Armen KUZANYAN, Vahan NIKOGHOSYAN**

Institute for Physical Research NAS of Armenia, Ashtarak-2, Ashtarak, 0203, Republic of Armenia

*Tel.: +37410288150, fax: +34723231172

*E-mail: akuzanyan@yahoo.com

Received: 5 November 2016 / Accepted: 5 December 2016 / Published: 30 December 2016

Abstract: The results of computer simulation of heat distribution processes taking place after absorption of single photons of 1 eV-1 keV energy in three-layer sensor of the thermoelectric detector are being analyzed. Different geometries of the sensor with tungsten absorber, thermoelectric layer of cerium hexaboride and tungsten heat sink are considered. It is shown that by changing the sizes of the sensor layers it is possible to obtain transducers for registration of photons within the given spectral range with required energy resolution and count rate. It is concluded that, as compared to the single layer sensor, the three-layer sensor has a number of advantages and demonstrate characteristics that make possible to consider the thermoelectric detector as a real alternative to superconducting single photon detectors.

Keywords: Thermoelectric, Single-photon detector, Multi-layer sensor.

1. Introduction

The increased interest in recent years to sources and detectors of single photons is due to remarkable progress in different areas of science and technology. Single photon detectors capable to determine the photon energy and to provide high count rates are demanded in quantum electronics, astrophysics, high energy physics, quantum informatics, telecommunication systems, quantum metrology, measuring systems for applications in medicine, homeland security and other fields [1-4]. A revolution in photon detection took place in connection with the development of detectors based on superconductivity [5-6]. These tools significantly improved the sensitivity of measurements across the electromagnetic spectrum, from radio waves through visible light to gamma rays. Superconducting Single-Photon Detectors (SSPD) come in two main types: thermal (TES) and pair-breaking (STJ). With both

types, the energy of an individual photon (and hence its frequency) is revealed by the strength of the device's output signal. Among the developments of the last 15 years, superconducting nanowire single-photon detectors (SNSPD) are considered as the most promising [7]. In terms of characteristics they compare favorably all earlier known detectors, possess a low dark-count rate, gigahertz count rate and are able to register photons in a wide range of the electromagnetic spectrum [8-10]. The thermoelectric single-photon detector (TSPD) possesses very close characteristics. The physical concept of the TSPD has been suggested in 2000 [11-12] being the only new approach in single photon detection methods introduced during quite a long time period [13]. The next investigations have shown that TSPD may compete with SNSPD, since in some properties and characteristics they are better [14-19]. Computer simulation of heat distribution processes in a single layer sensor of TSPD has revealed a number of peculiarities of TSPD, in

particular the dependence of the response on the area of the photon thermalization in the absorber [20-23]. Recently, the idea of a three-layer TSPD sensor was proposed [24] providing for independence of the response on the thermalization region [25]. In the present work the results of computer simulation of the heat distribution processes in a three-layer sensor of the TSPD occurring after absorption of photons with energies from 1 eV to 1 keV are presented.

2. Detection Pixels of TSPD

The design, peculiarities and characteristics of the single layer TSPD sensor were investigated in [11-12, 26]. The sensor contains two absorbers made of a heavy metal which are deposited on a dielectric substrate and coupled to each other by a thermoelectric bridge (Fig. 1(a)). When a photon enters the absorber its temperature rises, in comparison to that of the second absorber, leading to appearance of a voltage; by measuring this voltage the fact of absorption can be registered and the energy of the photon determined. Operation of such a sensor does not require any additional power source or applied voltage and, hence, no additional contacts. The TSPD sensor has remarkably simple design and provides for possibility to create detector matrix consisting of assemblage of sensors with very simple electronic structure. Such a sensor has, however, deficiencies limiting its application. The photon energy is being determined taking integral of the signal timing dependence. If the time decay of the signal to the background value is higher than the time of heat propagation through the metal-dielectric boundary, the so called Kapitza boundary, then a part of the heat extracted by the photon will pass to the substrate making impossible to determine the photon energy. The photon energy cannot be determined by the maximal value of the arising signal, since the temporal behavior depends on the area of the photon thermalization. The three-layer design of the TPSD sensor (Fig. 1(b)) avoids such dependence and the possibility of heat draft from absorber to the substrate.

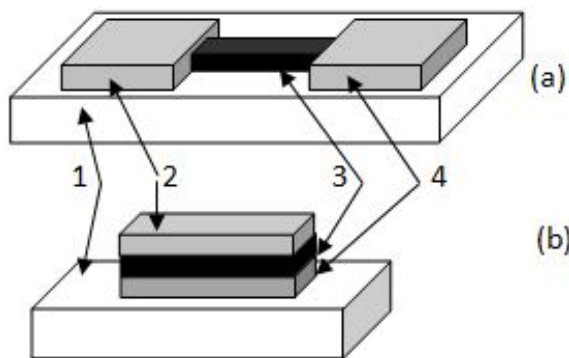


Fig. 1. Single layer (a), and three-layer (b) sensors design:
1 – substrate; 2 – absorber; 3 – thermoelectric layer;
4 – heat sink.

3. Computing Technique

The calculations were based on the heat conduction equation and were carried out by the matrix method for differential equations. For the function of three spatial variables (x, y, z) and the time variable t , the heat conduction equation is

$$\rho c \frac{\partial T}{\partial t} + \frac{\partial q_x}{\partial x} + \frac{\partial q_y}{\partial y} + \frac{\partial q_z}{\partial z} = 0, \quad (1)$$

Where ρ is the heat-conducting material's density, c is the specific heat capacity, and q_x, q_y and q_z are the projections of the heat flux density vector

$$q_x = -\lambda \frac{\partial T}{\partial x}, \quad q_y = -\lambda \frac{\partial T}{\partial y}, \quad q_z = -\lambda \frac{\partial T}{\partial z} \quad (2)$$

Here λ is the thermal conductivity. The specific heat capacity at liquid-helium temperatures is determined by the equation

$$c = \gamma T + AT^3, \quad (3)$$

Where the coefficient A indicates the contribution of phonons and γ (Sommerfeld coefficient) presents the contribution of electrons. For simplicity of calculations, the phonon contribution to the heat capacity is not taken into account ($A = 0$). The operating temperature of the detector was taken to be 9 K, since at this temperature CeB_6 crystals have the highest value of thermoelectric Fig. of merit. The used in calculations parameters are given in Table 1.

Table 1. Parameters of used materials at 9 K [27-30].

| Parameters | Material | |
|--|----------|----------------|
| | W | CeB_6 |
| Density, kg/m^3 | 19250 | 4800 |
| Specific heat capacity, $\text{J/kg}\cdot\text{K}$ | 0.197 | 7.3 |
| Sommerfeld coefficient, $\text{J/kg}\cdot\text{K}^2$ | 0.022 | 0.8 |
| Thermal conductivity, $\text{W/m}\cdot\text{K}$ | 9680 | 1.5 |
| Seebeck coefficient, $\mu\text{V/K}$ | - | 150 |

The thermal processes were modeled according to the following algorithm.

- The entire volume of the absorber and the bridge was broken down into the cells with the dimensions $\Delta x, \Delta y$ and $\Delta z \leq 0.1 \mu\text{m}$. Obviously, the enlargement of the number of cells will provide more accurate calculations, but it will lead to more time consuming.

- The initial temperature for the all cells was set 9 K. In the absorber was chosen the cell where the photon is absorbed.

- According to the formula $\Delta T = E/V\rho c$, where E is the energy of the absorbed photon and V is the cell volume, the initial temperature of the cell $T_0 = 9 \text{ K} + \Delta T$ was calculated.

The temperature of the all cells for each time point it was determined by the equation:

$$T_{ijk}(t_{n+1}) = T_{ijk}(t_n) + \frac{\Delta t}{\rho c} \left[\frac{\lambda(T_{i+1}) + \lambda(T_i)}{2} \cdot \frac{T_{i+1} - T_i}{\Delta x^2} + \frac{\lambda(T_{j+1}) + \lambda(T_j)}{2} \cdot \frac{T_{j+1} - T_j}{\Delta y^2} + \frac{\lambda(T_{k+1}) + \lambda(T_k)}{2} \cdot \frac{T_{k+1} - T_k}{\Delta z^2} \right] \quad (4)$$

Here i, j, k are the coordinates of the cell, n is the number of time interval from the beginning of the process, Δt is the time interval. Obviously, the value of Δt also determines the accuracy and speed of the calculation.

The absorber thickness is the most important parameter of the TSPD sensor. We were selecting this parameter proceeding from the demand to provide for high probability of photon absorption in the absorber. Taking the Bouguer-Lambert law and using the values for the coefficient of linear attenuation in W for 1 keV, 100 eV and 10 eV energy photons equal to respectively $5.775 \mu\text{m}^{-1}$, $28.875 \mu\text{m}^{-1}$ and $115.5 \mu\text{m}^{-1}$ [31], it is easy to calculate that the probability of absorption in $1.5 \mu\text{m}$ thick W of a photon of 1 keV energy will be 0.9998. The absorption probability for 100 eV and 10 eV photons in respectively $0.5 \mu\text{m}$ and $0.1 \mu\text{m}$ thick W will exceed 0.9999. It is obvious that thinner tungsten absorbers or absorbers fabricated from not heavy metals can be used to provide for absorption of photons with energies less than 10 eV with the same probability. However, we shall not consider the characteristics of such sensors for the following three reasons. We do not want to enlarge the volume of the article, as well as to complicate its perception. The third reason is that a sensor with $0.1 \mu\text{m}$ thick tungsten absorber can be successfully used for detection of 1 - 10 eV photons. The obtained results give evidence for that.

Fig. 2 shows the graphs for the probability of reaching by photons of 1 keV, 100 eV and 10 eV energies definite depths in the W absorber and showing that the probability for absorption in upper layers of the absorber is the highest.

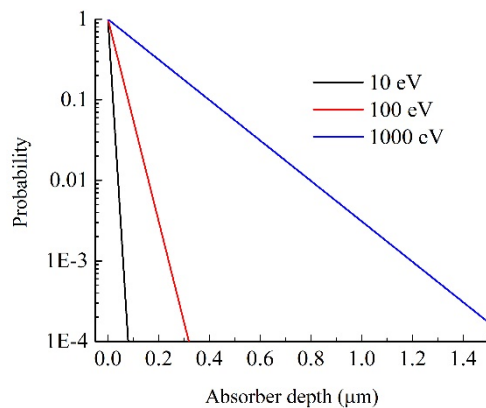


Fig. 2. Probability of reaching by a photon a definite depth in the tungsten absorber.

The calculations for heat propagation processes in the three-layer TSPD sensor are therefore carried out

for the cases of photon absorption close to surface of the absorber.

Let us also mention that in the multilayer option of the sensor the heat removal may be provided by using not heavy metal. In the case of necessity, the multilayer sensor versions employing various materials for the heat sink can be considered.

4. Results

The geometrical dimensions of sensors and results of calculations of heat propagation in the three-layer sensor are presented in Table 2.

The columns in the table give the calculation number, the geometric dimensions of absorber (X, Y, Z_1), the thickness of thermoelectric layer (Z_2), the thickness of heat sink (Z_3), the distance from surface of absorber in which photon is absorbed (h), the photon energy (E), the maximum temperature difference on the thermoelectric layer after photon absorption (ΔT_m), time duration to achieve the ΔT_m (t_m), the maximum of voltage on the sensor (U_m), the time of recession ΔT to the background 10^{-4}K (t_b), its inverse (count rate) (R). In accordance with Fig. 1, the geometric dimensions X and Y of the thermoelectric layer and of the heat sink are similar to those of absorber. In the calculations it was assumed that the photon is thermalized in the center of the absorber surface.

We shall start the discussion of the obtained results with consideration of X-ray photon absorption. Let us investigate the temporal behavior of the temperature difference $\Delta T(t)$ between the two surfaces of the thermoelectric layer in five different parts of the sensor which are at different distances from the sensor center.

The graphs of this dependence for the calculation 1 M from Table 2 are given on Fig. 3. As expected, the highest values for the temperature difference are reached in region 1, i.e. in the center of the sensor, directly under the point of photon thermalization. With distancing from the center the signal weakens and in the point 5 (which is the most far) the maximum is reached in 3 ps from the moment of photon absorption; it is of the order of the background value, 10^{-4}K . A similar result is seen for the rest of calculations, and since the value of arising voltage on the sensor is determined by the maximal temperature difference on the thermoelectric layer, we shall consider further only the dependences $\Delta T(t)$ calculated for region 1.

Note that the graphs shown on Fig. 3 practically merge after 4 ps from the process start. During this time period the heat generated by the photon has already spread throughout the absorber volume.

Table 2. W/CeB₆/W three-layer sensor geometry and calculated parameters.

| No | X, Y, Z ₁ , μm | Z ₂ , μm | Z ₃ , μm | h, μm | E, eV | ΔT _m , mK | t _m , ps | U _m , μV | t _b , ps | R, GHz |
|-----|------------------------------|------------------------|------------------------|----------|----------|-------------------------|------------------------|------------------------|------------------------|-----------|
| 1M | 10, 10, 1.5 | 1 | 1 | 0.1 | 1000 | 6.78 | 0.162 | 1.017 | >10000 | <0.1 |
| 2M | 10, 10, 1.5 | 0.5 | 1 | 0.1 | 1000 | 6.78 | 0.162 | 1.017 | >10000 | <0.1 |
| 3M | 10, 10, 1.5 | 0.1 | 1 | 0.1 | 1000 | 6.75 | 0.156 | 1.013 | 420 | 2.4 |
| 4M | 10, 10, 1.5 | 0.05 | 1 | 0.1 | 1000 | 6.75 | 0.156 | 1.013 | 186.6 | 5.4 |
| 5M | 10, 10, 1.5 | 0.01 | 1 | 0.1 | 1000 | 5.64 | 0.156 | 0.846 | 4.8 | 208 |
| 6M | 10, 10, 1.5 | 0.01 | 2 | 0.1 | 1000 | 5.64 | 0.156 | 0.846 | 4.8 | 208 |
| 7M | 10, 10, 1.5 | 0.01 | 5 | 0.1 | 1000 | 5.64 | 0.156 | 0.846 | 4.8 | 208 |
| 8M | 10, 10, 1.5 | 0.01 | 1 | 0.1 | 1100 | 6.2 | 0.156 | 0.93 | 5.1 | 196 |
| 9M | 10, 10, 1.5 | 0.01 | 1 | 0.1 | 900 | 5.07 | 0.156 | 0.761 | 4.5 | 222 |
| 10M | 10, 10, 1.5 | 0.01 | 1 | 0.1 | 1010 | 5.69 | 0.156 | 0.854 | 4.8 | 208 |
| 11M | 20, 20, 1.5 | 0.01 | 1 | 0.1 | 1000 | 5.64 | 0.156 | 0.846 | 3.9 | 256 |
| 12M | 5, 5, 1.5 | 0.01 | 1 | 0.1 | 1000 | 5.64 | 0.156 | 0.846 | 8.7 | 114 |
| 13M | 10, 10, 0.5 | 0.05 | 1 | 0.1 | 100 | 36.8 | 0.012 | 5.52 | 21.9 | 45.7 |
| 14M | 10, 10, 0.5 | 0.05 | 1 | 0.1 | 110 | 40.48 | 0.012 | 6.072 | 25.5 | 39.2 |
| 15M | 10, 10, 0.5 | 0.05 | 1 | 0.1 | 90 | 33.12 | 0.012 | 4.968 | 18 | 55.5 |
| 16M | 10, 10, 0.5 | 0.01 | 1 | 0.1 | 100 | 33.71 | 0.012 | 5.057 | 2.97 | 337 |
| 17M | 10, 10, 0.5 | 0.01 | 2 | 0.1 | 100 | 33.71 | 0.012 | 5.057 | 3 | 333 |
| 18M | 10, 10, 0.5 | 0.01 | 5 | 0.1 | 100 | 33.71 | 0.012 | 5.057 | 3 | 333 |
| 19M | 10, 10, 0.1 | 0.01 | 1 | 0.01 | 10 | 114.7 | 0.0015 | 17.2 | 1.32 | 758 |
| 20M | 10, 10, 0.1 | 0.01 | 1 | 0.01 | 11 | 126.1 | 0.0015 | 18.9 | 1.44 | 694 |
| 21M | 10, 10, 0.1 | 0.01 | 1 | 0.01 | 9 | 103.3 | 0.0015 | 15.5 | 1.2 | 833 |
| 22M | 10, 10, 0.1 | 0.01 | 1 | 0.01 | 7 | 80.3 | 0.0015 | 12.05 | 0.963 | 1038 |
| 23M | 10, 10, 0.1 | 0.01 | 1 | 0.01 | 4 | 45.9 | 0.0015 | 6.885 | 0.651 | 1536 |
| 24M | 10, 10, 0.1 | 0.01 | 1 | 0.01 | 1 | 11.5 | 0.0015 | 1.725 | 0.303 | 3300 |
| 25M | 10, 10, 0.1 | 0.01 | 1 | 0.01 | 1.1 | 12.6 | 0.0015 | 1.89 | 0.321 | 3115 |
| 26M | 10, 10, 0.1 | 0.01 | 1 | 0.01 | 0.9 | 10.3 | 0.0015 | 1.545 | 0.282 | 3546 |
| 27M | 10, 10, 0.5 | 0.01 | 1 | 0.2 | 100 | 71.3 | 0.0069 | 10.695 | 2.1 | 476 |
| 28M | 10, 10, 0.5 | 0.01 | 1 | 0.3 | 100 | 179.7 | 0.004 | 26.955 | 2.1 | 476 |
| 29M | 10, 10, 1 | 0.01 | 1 | 0.1 | 100 | 3.4 | 0.06 | 0.51 | 1.671 | 598 |
| 30M | 10, 10, 1 | 0.01 | 1 | 0.2 | 100 | 4.0 | 0.045 | 0.6 | 1.659 | 602 |
| 31M | 10, 10, 1 | 0.01 | 1 | 0.3 | 100 | 5.6 | 0.033 | 0.84 | 1.644 | 608 |
| 32M | 10, 10, 0.5 | 0.01 | 0.5 | 0.1 | 100 | 33.7 | 0.012 | 5.057 | 2.85 | 351 |
| 33M | 10, 10, 0.5 | 0.01 | 0.1 | 0.1 | 100 | 33.7 | 0.012 | 5.057 | 2.191 | 456 |
| 34M | 10, 10, 0.5 | 0.01 | 0.05 | 0.1 | 100 | 33.7 | 0.012 | 5.057 | 1.699 | 589 |
| 35M | 10, 10, 0.1 | 0.01 | 0.5 | 0.01 | 1 | 11.5 | 0.0015 | 1.722 | 0.30561 | 3272 |
| 36M | 10, 10, 0.1 | 0.01 | 0.1 | 0.01 | 1 | 11.5 | 0.0015 | 1.722 | 0.30705 | 3257 |
| 37M | 10, 10, 0.1 | 0.01 | 0.05 | 0.01 | 1 | 11.5 | 0.0015 | 1.722 | 0.30711 | 3256 |

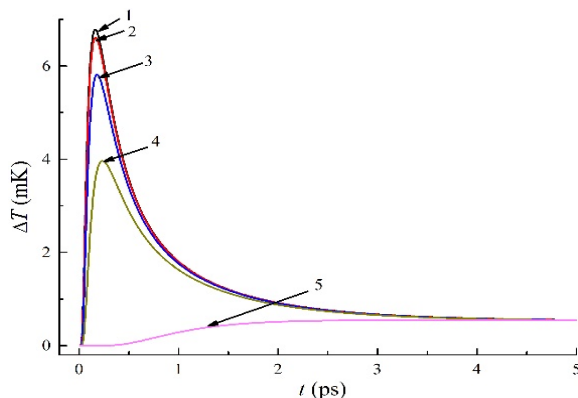


Fig. 3. ΔT(t) dependence of the calculation 1M measured in five different areas of the thermoelectric layer: in the center (1), at different distances from the center: 0.2 μm (2), 0.5 μm (3), 1 μm (4), 5 μm (5).

After that, the heat must pass through the thermoelectric layer.

It follows from the table data that for the calculation 1M decay time to the background level is above 10 ns. The reason for this is in the low value of thermal conductivity coefficient of CeB₆. Acceleration of the heat transfer from absorber to the heat sink can be achieved by decreasing the thickness of the thermoelectric layer. In calculations 1 M – 5 M, the thermoelectric latter was gradually decreased from 1 μm to 0.01 μm. The graphs of ΔT(Z₂) and t_b(Z₂) dependencies of these calculations are presented on Fig. 4.

We can see that parameter t_b is decreasing upon decreasing of the thickness of the thermoelectric layer, while the values of the parameter ΔT_m remain practically unchanged up to 0.05 μm thicknesses. Parameter ΔT_m is somewhat smaller for the 0.01 μm thick thermoelectric layer but at the same time the

signal is going down to the background value much faster thus providing for counting rate of the order of 200 GHz. In further calculations we shall use this value for the thickness of the thermoelectric layer.

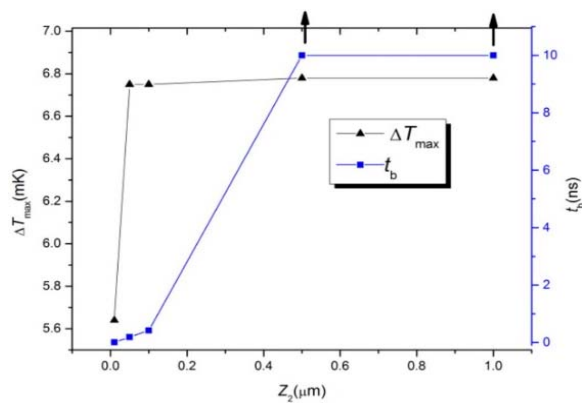


Fig. 4. Dependence of the ΔT_m and t_b parameters of calculations 1 M – 5 M on the thickness of the thermoelectric layer.

Let compare the results of calculations 5-7 for sensors with 1-5 μm thicknesses of the W heat sink. It is seen from Table 2 that variation of the heat sink thickness does not influence the value of maximum signal and the count rate. It can be concluded that the thickness of the heat sink does not have a significant influence on the characteristics of the sensor and can be selected taking into account other constructional demands.

Fig. 5 shows $\Delta T(t)$ graphs for the cases of 1 keV and 1 ± 0.1 keV photon absorption. It can be seen that change of photon energy leads to change in the ΔT_m value, while t_m does not change. It follows from Table 2 that the U_m values differ by 85 nV, if the photon energies differ by 10 %, and by 8 nV, if they differ by 1 %. It should be also mentioned that change in photon energy leads to some change of the count rate. Parameter R is smaller in the case of higher photon energies, since after thermalization in the absorber of the photon with a higher energy the temperature difference resulting on the thermoelectric layer is going down slower to the background value.

The next calculations in Table 2 are performed for sensors having twice larger dimensions on X and Y coordinates (11 M) and twice smaller dimensions (12 M). Comparison of their characteristics with those for calculation number 5 M shows that in the first case the count rate increases from 208 GHz to 256 GHz, while in the second case it decreases down to 114 GHz. Their ΔT_m values in the meantime do not differ. From comparison of these data with those graphs of Fig. 3 it can be stated that in a three-layer sensor the TSPD absorber carries out not only the task of transformation of the photon energy to heat, but also of heat transfer from the thermalization zone of the photon. It is evident that these fact favors a remarkable increase of the count rate.

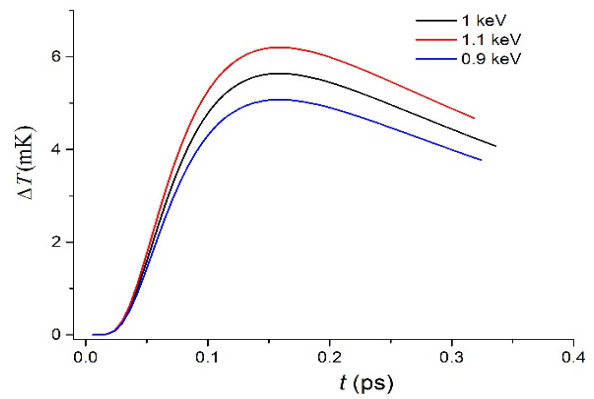


Fig. 5. $\Delta T(t)$ dependencies of calculation numbers 5 M, 8 M, 9 M for the cases of absorption of photons with 1000 eV, 1100 eV and 900 eV energies.

Now let us consider the calculations on detection of UV photons with energies above 100 eV, which border with X-ray energies, to 4 eV, or to the border of the visible range. Absorption of photons in calculations 13 M – 15 M is considered with energies of 100 eV and 100 ± 10 eV in 0.5 μm thick tungsten absorber. It follows from Table 2 that the voltages corresponding to maximums of these dependences differ by 0.55 μV . Registration of signals differing by nanovolts will prove achievement of 0.1 eV energy resolution.

Comparison of ΔT_m parameters for 4 M and 13 M calculations shows that as a result of a 100 eV photon absorption this parameter is bigger almost by one order, than in the case of X-ray photons. Explanation of this fact will be given later. Now we shall consider the results of 16 M – 18 M calculations which have been carried out for the sensor geometries with different thicknesses of the tungsten heat sink and the thermoelectrics thickness of 0.01 μm . In this case, as it follows from the table, the thickness of the heat sink does not influence the parameters ΔT_m , t_m , U_m , t_b and R . However, in comparison to the previous 3 calculations, when the thickness of the thermoelectric layer was 0.05 μm , the count rate is remarkably higher. It goes up to 333 GHz that exceeds the known to us literature values for this parameter in superconducting detectors.

Calculations presented in Table 2 for 11 eV and smaller photon energies were done for the sensor with 0.1 μm absorber thickness. As mentioned above, such a thickness of the W absorber provides for photon absorption in the given energy range with probability close to 1. Calculations 19 M – 21 M were carried out for the case of photon absorption with energy 10 eV and 10 ± 1 eV. Parameter ΔT_m for these calculations is also much bigger, as compared to the value of this parameter in calculations 8 M – 10 M, although the photon energy is decreased by one order. This seems strange, as in the above case, when comparing the calculation results for the cases of 1 keV and 100 eV photons absorption. The situation is cleared if taking into account the change of the absorber thickness. When going from X-ray photons to UV photons with

100 eV energy we had decreased the absorber thickness Z_1 from 1.5 μm to 0.5 μm , or by a factor of 3, and correspondingly by a factor of 5, up to 0.1 μm upon changing the photon energy from 100 eV to 10 eV. Calculations of ΔT to which the tungsten hemisphere will be heated by a photon of energy E give for the 3 considered cases the following values: $E = 1 \text{ keV}$, $Z_1 = 1.5 \mu\text{m}$, $\Delta T = 0.008 \text{ K}$; $E = 100 \text{ eV}$, $Z_1 = 0.5 \mu\text{m}$, $\Delta T = 0.022 \text{ K}$; $E = 10 \text{ eV}$, $Z_1 = 0.1 \mu\text{m}$, $\Delta T = 0.352 \text{ K}$. These values of ΔT correspond to the values of ΔT_m in calculations 5 M, 16 M and 19 M.

From the data of Table 2 for absorption of photons of 10 eV, 11 eV and 9 eV energies, the values of the U_m parameter are equal correspondingly to 17.2 μV , 18.9 μV and 15.5 μV . The 1 eV difference in energy, at the level of 10 eV, corresponds to the voltage of 1.7 μV , or the registration of the signal with 0.17 μV accuracy will provide for a 0.1 eV energy resolution. At the same time it is a pleasure to state that parameter R of calculations 19 M – 21 M constitutes a few hundreds of gigahertz.

Dependence of the U_m parameter on energy of the absorbed photon for calculations 19 M – 26 M is presented on Fig. 6. These calculations were carried out at similar geometric sizes of the sensor layers. The observed in this case linearity shows that the U_m parameter, or the measured in the experiment maximum of arising voltage on the sensor, can be used for exact determination of the energy of the absorbed photon.

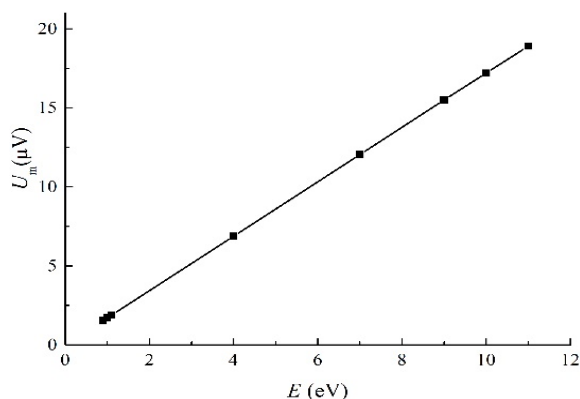


Fig. 6. Dependence of the U_m parameter from calculations 19 M – 26 M on the energy of absorbed photon.

According to data of Table 2, for IR photons with energies of 0.9 eV, 1 eV and 1.1 eV (calculations 24 M – 26 M) the U_m parameter is equal respectively to 1.545 μV , 1.725 μV and 1.89 μV . Thus, the 0.1 eV energy difference at 1 eV level corresponds to U_m parameter difference by 0.18 μV . It can be stated, that for the IR photons the accuracy of the photon energy valuation can also be better than 1 %.

Let us pay attention to the count rate parameter for the calculations 22 M – 26 M given in Table 2. The data show that for the near UV range, as well as for the IR, the photon count rate may reach terahertz values. The count rate of the single layer sensor of TSPD, as

well as of superconducting detectors, is by orders of magnitude lower [20-23].

Let us consider the case, when the photon is absorbed at some distance below the absorber surface. As it has been shown above (Fig. 2) the probability for a photon to reach a certain depth in the absorber is strongly reduced with increasing this depth. Nevertheless, we have done calculations for processes of heat distribution in a three-layer sensor of TSPD upon absorption of a 100 eV energy photon at different depths from the absorber surface. At the same dimensions of the sensor, calculations 4 M, 27 M and 28 M were done for the cases of photon absorption at 0.1 μm , 0.2 μm and 0.3 μm distances from 0.5 μm thick absorber surfaces. Fig. 7 shows $\Delta T(t)$ graphs for these calculations. Calculations 29 M, 30 M and 31 M were done for photon absorption at the same depths, but in a 1 μm thick absorber. As it can be seen from Fig. 7 the signal, as expected, is amplified and the maximum is reached faster when the point of photon thermalization is approaching the thermoelectric layer. Similar results are obtained for calculations 29 M – 31 M (see Table 2). With increasing h , higher values of parameter ΔT_m are reached, while parameter t_m is decreasing.

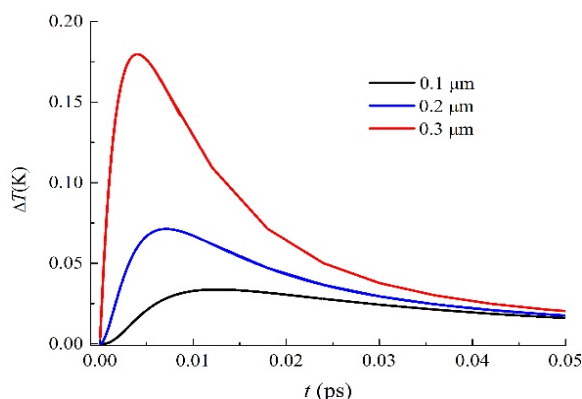


Fig. 7. $\Delta T(t)$ dependencies of calculation numbers 4 M, 27 M, 28 M for the cases of absorption of photons with 100 eV energy at 0.1 μm , 0.2 μm and 0.3 μm distances from absorber surface.

Analysis of data of Table 2 allows concluding that, at the same architecture of the sensor, parameter t_m depends on the distance from absorber surface at which photon is absorbed (h), while t_m and ΔT_m parameters uniquely define the energy of the absorbed photon.

Finally, let us consider sensors with the heat sink thinner than 1 μm . The characteristics of sensors with a thin heat sink may differ from the results of previous calculations. The need for such sensors may arise for solution of some specific tasks. The thickness of the heat sink in calculations 1 M – 31 M was varied in the range 1 - 5 μm , and we came to the conclusion that such a change of the heat sink thickness did not change the characteristics of the signal obtained after photons

absorption. Calculations 32 M – 37 M reveal that the t_m and ΔT_m signal parameters do not change when the thickness of the heat sink becomes less than 1 μm . Parameters t_b , and therefore the count rate are changing. Moreover, as it follows from the data given in Table 2, this change is different for photons of different energies. Fig. 8 clearly shows that with decreasing of the heat sink thickness, parameter R increases for calculations describing the absorption of photons with 100 eV energy, while it decreases in the case of absorption of 1 eV photons. This strongly different behavior becomes understandable after a more detailed consideration of processes of heat propagation in a three-layer sensor.

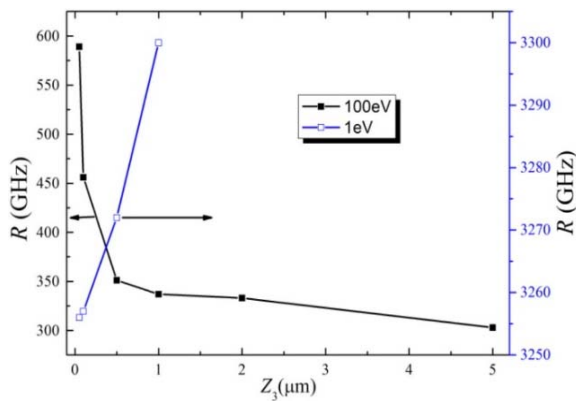


Fig. 8. Dependence of parameter R from calculations for 1 eV and 100 eV energy photons on the thickness of heat sink.

Let us check how is changing with time the temperature at the thermoelectric-heat sink boundary (T_1) directly under the zone of photon thermalization. Fig. 9 shows $T_1(t)$ graphs for the cases of 1 eV (calculation 37 M) and 100 eV (calculation 34 M) photon absorption in the sensor with a 50 nm thick heat sink for time interval 0 – t_b .

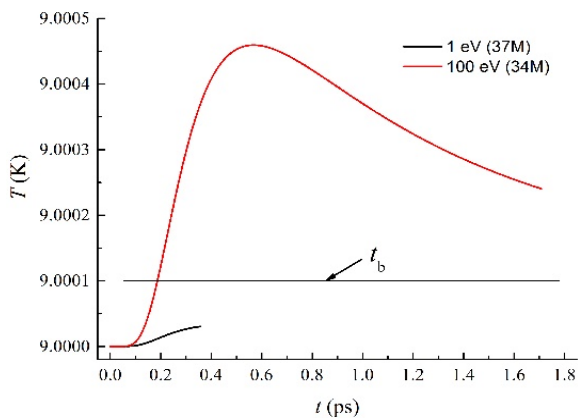


Fig. 9. $T_1(t)$ dependence for 1 eV and 100 eV photons absorptions in the sensors with heat sink of 50 nm thickness.

As seen, these graphs largely differ. While upon absorption of 100 eV photons this zone is heated to T_1 which is exceeding by 4 times the background temperature (T_b), in the case of 1 eV photon absorption the value of T_1 is significantly lower than T_b . At the same time we see different dynamics of heat propagation processes for the two calculations which is the reason for the differences shown in Fig. 8.

Note that the changes of parameter R versus the thickness of the heat sink is small. According to calculations, for 100 eV photons the decrease in thickness of the heat sink by a factor of 100 leads to increase of the parameter R by less than two times; for the case of 1 eV photons the decrease in thickness of the heat sink by a factor of 20 leads to reduction of the parameter R by 1.3 %.

Is it realistic to measure the signal from the thermoelectric sensor considered in the present work?

1) The following results or data were considered in previous papers [11, 16] concerning the principal possibility of conversion of the thermoelectric energy to electrical voltage and digital superconducting readout:

- Experimental registration of the signal coming from thermoelectric single layer sensor consisting of Sb absorber and heat-sink with an Au-Fe thermoelectric bridge between them;
- Signal acquisition scheme in single-pixel experiments.

Thermoelectric sensors can function as either voltage or current sources. The low working temperatures and low impedance of the sensors facilitate using SQUIDs as preamps for the lowest noise. SQUIDs measure current and transform it into voltage. Three important conclusions on the signal registration chain are apparent from this scheme:

- a) Any parasitic resistance should be eliminated (in devices, interconnections, etc.).
- b) Input/output impedances should match in cold stage (detector unit and superconductor electronics), and in room temperature stage, the amplifier input noise should be lower than the output noise level from the SQUID preamplifier.
- c) Signal acquisition bandwidth should be optimized.

Concluding this part, we can state that the signal of the thermoelectric detector operating at helium temperatures can be registered.

2) As it is shown in the present work, the voltage appearing on the sensor can reach micro-volts; to provide an energy resolution of better than 1 %, it is necessary to have resolution of a few nanovolts. Registration of such a signal of sensor of TSPD can be realized without difficulties for signal of nanosecond durations [11].

3) For shorter duration signals the approaches commonly used in superconducting detectors can be used in registration of the signal of the thermoelectric sensor, since despite of very different physical processes underlying these two types of detectors, the final stage is the registration of the out-coming electrical signal, while electronics is indifferent to the

origin of the signal and as a result of which physical processes it is originating.

In conclusion, summing these arguments we can give a positive answer to the above raised question on possibility of signal registration coming from the thermoelectric sensor considered in this work.

5. Conclusions

The obtained results allow the following conclusions to be done:

1) The three-layer sensor of TSPD may register individual photons in a wide range of the electromagnetic spectrum from 1 eV to 1 keV, providing energy resolution of not less than 1 % and count rate from tens gigahertz to terahertz.

2) For solution of a wide range of different tasks the ratio (energy resolution)/(count rate) can be varied by changing the geometric sizes of the sensor.

3) Taking into account several features of the thermoelectric detector, such as simple design, high position resolution and absence of strict requirements to operating conditions, it can be argued that thermoelectric detectors with multi-layer sensor can be a real competitor to superconducting detectors.

The superconducting single photon detectors have a longer history of development, as compared to thermoelectric ones. A big number of research groups have been involved and continue the studies on superconducting detectors at present in many countries that resulted in remarkable improvement of SSPD characteristics. The authors hope that the present publication will attract attention to thermoelectric detectors and that the experimental results on TSPD research will appear soon, since following the results of computer simulation this is quite a perspective direction.

Acknowledgements

This work was supported by the RA MES State Committee of Science and Russian Foundation for Basic Research (RF) in the frames of the joint research projects SCS 15RF-018 and RFBR 15-53-05047 accordingly.

The authors would like to thank Dr. A.M. Gulian for the helpful discussions.

References

- [1]. R. H. Hadfield, Single-photon detectors for optical quantum information applications, *Nature Photonics*, Vol. 3, No. 12, 2009, pp. 696-705.
- [2]. J. J. Renema, Q. Wang, R. Gaudio, I. Komen, K. Hoog Op't, D. Sahin, A. Schilling, M. P. van Exter, A. Fiore, A. Engel, M. J. A. de Dood, Position-Dependent Local Detection Efficiency in a Nanowire Superconducting Single-Photon Detector, *Nano Letters*, Vol. 15, No. 7, 2015, pp. 4541-4545.
- [3]. M. Kaniber, F. Flassig, G. Reithmaier, R. Gross, J. J. Finley, Integrated superconducting detectors on semiconductors for quantum optics applications, *Applied Physics B*, Vol. 122, No. 115, 2016, pp. 1-2.
- [4]. T. Yamashita, S. Miki, H. Terai, Z. Wang, Low-filling-factor superconducting single photon detector with high system detection efficiency, *Optics Express*, Vol. 21, Issue 22, 2013, pp. 27177-27184.
- [5]. K. D. Irwin, Seeing with Superconductors, *Scientific American*, Vol. 295, 2006, pp. 86-95.
- [6]. J. N. Ullom, D. A. Bennett, Review of superconducting transition-edge sensors for X-ray and gamma-ray spectroscopy, *Superconductor Science and Technology*, Vol. 28, No. 8, 2015, 084003.
- [7]. G. N. Gol'tsman, O. Okunev, G. Chulkova, A. Lipatov, A. Semenov, K. Smirnov, B. Voronov, A. Dzardanov, C. Williams, R. Sobolewski, Picosecond superconducting single-photon optical detector, *Applied Physics Letters*, Vol. 79, No. 6, 2001, pp. 705-707.
- [8]. H. A. Atikian, A. Eftekharian, J. A. Salim, M. J. Burek, J. T. Choy, H. A. Majedi, M. Lončar, Superconducting nanowire single photon detector on diamond, *Applied Physics Letters*, Vol. 104, Issue 12, 2014, 122602.
- [9]. D. Liu, S. Miki, T. Yamashita, L. You, Z. Wang, H. Terai, Multimode fiber-coupled superconducting nanowire single-photon detector with 70 % system efficiency at visible wavelength, *Optics Express*, Vol. 22, Issue 18, 2014, pp. 21167-21174.
- [10]. J. J. Renema, R. Gaudio, Q. Wang, Z. Zhou, A. Gaggero, F. Mattioli, R. Leoni, D. Sahin, M. J. A. de Dood, A. Fiore, M. P. van Exter, Experimental test of theories of the detection mechanism in a nanowire superconducting single photon detector, *Phys. Rev. Lett.*, Vol. 112, No. 11, 2014, 117604.
- [11]. G. G. Fritz, K. S. Wood, D. van Vechten, A. L. Gyulamiryan, A. S. Kuzanyan, N. J. Giordano, T. M. Jacobs, H.-D. Wu, J. S. Horwitz, A. M. Gulian, Thermoelectric single-photon detectors for X-ray/UV radiation, *Proc. SPIE*, Vol. 4140, 2000, pp. 459-469.
- [12]. D. Van Vechten, K. Wood, G. Fritz, J. Horwitz, A. Gyulamiryan, A. Kuzanyan, V. Vartanyan, A. Gulian, Imaging detectors based on anisotropic thermoelectricity, *Nuclear Instruments and Methods in Physics Research*, Vol. 444, Issue 1-2, 2000, pp. 42-45.
- [13]. S. N. Song, S. R. Maglic, C. D. Thomas, M. P. Ulmer, J. B. Ketterson, High energy resolution X-ray detection based on a coupled Fiske cavity and Josephson junction oscillator, *Applied Physics Letters*, Vol. 69, No. 11, 1996, pp. 1631-1633.
- [14]. K. Wood, D. Van Vechten, G. Fritz, H.-D. Wu, S. Bounnak, K. Bussman, K. Winzer, S. Kunii, V. Gurin, M. Korsukova, C. Mitterer, M. Corlsson, F. Golf, A. Kuzanyan, G. Badalyan, S. Horutyunyan, S. Petrosyan, V. Vardanyan, T. Paronyan, V. Nikoghosyan, A. Gulian, Toward Ultimate Limits of Performance of the QVD Detector, *Nuclear Instruments and Methods in Physics Research*, Vol. 520, Issue 1-3, 2004, pp. 56-59.
- [15]. A. Gulian, K. Wood, D. VanVechten, G. Fritz, H.-D. Wu, S. Bounnak, K. Bussman, K. Winzer, S. Kunii, V. Gurin, M. Korsukova, C. Mitterer, M. Corlsson, F. Golf, A. Kuzanyan, G. Badalyan, S. Horutyunyan, S. Petrosyan, V. Vardanyan, T. Paronyan, V. Nikoghosyan, Current developmental status of thermoelectric (QVD) detectors, *Nuclear Instruments*

- and Methods in Physics Research, Vol. 520, Issue 1-3, 2004, pp. 36-40.
- [16]. A. Gulian, K. Wood, D. Van Vechten, G. Fritzdet, Cryogenic thermoelectric (QVD) detectors: Emerging technique for fast single-photon counting and non-dispersive energy characterization, *Journal of Modern Optics*, Vol. 51, Issue 9-10, 2004, pp. 1467-1490.
- [17]. V. A. Petrosyan, Hexaborides of Rare Earths as a Sensor Material for Thermoelectric Single-Photon Detectors, *J. Contemp. Phys. (Arm. Acad. Sci.)*, Vol. 46, 2011, pp. 125-128.
- [18]. A. A. Kuzanyan, V. A. Petrosyan, A. S. Kuzanyan, Thermoelectric single-photon detector, *Journal of Physics: Conference Series*, Vol. 350, No. 1, 2012, 012028.
- [19]. A. A. Kuzanyan, A. S. Kuzanyan, Thermoelectric Nanowire Single-Photon Detector, *Proc. of SPIE*, Vol. 8773, 2013, 87730L-1.
- [20]. A. A. Kuzanyan, Nanosensor for Thermoelectric Single-Photon Detector, *Nano Studies*, Vol. 9, 2014, pp. 93-102.
- [21]. A. Kuzanyan, V. Nikoghosyan, A. Kuzanyan, Modeling of Kinetic Processes in Thermoelectric Single Photon Detectors, *Proc. of SPIE*, Vol. 9504, 2015, 950400.
- [22]. A. Kuzanyan, V. Nikoghosyan, A. Kuzanyan, CeB₆ Sensor for Thermoelectric Single-Photon Detector, *Sensors & Transducers*, Vol. 191, Issue 8, August 2015, pp. 57-62.
- [23]. A. A. Kuzanyan, A. S. Kuzanyan, V. R. Nikoghosyan, Ultrafast TSPD on the basis of CeB₆ sensor, *Journal of Physics: Conference Series*, Vol. 673, 2016, p. 012007.
- [24]. A. Kuzanyan, A. Kuzanyan, V. Nikoghosyan, Multi-layer sensor of thermoelectric detector, Patent of Armenia № 2946, 2015.
- [25]. A. A. Kuzanyan, A. S. Kuzanyan, V. R. Nikoghosyan, V. N. Gurin, M. P. Volkov, Investigation of processes of heat propagation in multilayer sensor of thermoelectric single-photon detector, *Journal of Contemporary Physics (Arm. Acad. Sci.)*, Vol. 51, Issue 2, 2016, pp. 181-190.
- [26]. K. S. Wood, G. G. Fritz, A. M. Gulian, D. Van Vechten, Photon detector, *US Patent US 6,710,343 B2*, 2004.
- [27]. V. Petrosyan, V. Vardanyan, V. Kuzanyan, M. Konovalov, V. Gurin, A. Kuzanyan, Thermoelectric properties and chemical composition of CeB₆ crystals obtained by various methods, *Solid State Sciences*, Vol. 14, Issue 11-12, 2012, pp. 1653-1655.
- [28]. T. R. Waite, R. S. Craig, W. E. Wallace, Heat Capacity of Tungsten between 4 and 15°K, *Phys. Rev. Lett.*, Vol. 104, Issue 5, 1956, pp. 1240-1241.
- [29]. S. R. Harutyunyan, V. H. Vardanyan, A. S. Kuzanyan, V. R. Nikoghosyan, S. Kunii, K. S. Wood, A. M. Gulian, Thermoelectric cooling at cryogenic temperatures, *Applied Physics Letters*, Vol. 83, Issue 11, 2003, pp. 2142-2144.
- [30]. Y. Peysson, C. Ayache, B. Salce, J. Rossat-Mignod, S. Kunii, T. Kasuya, Thermal conductivity of CeB₆ and LaB₆, *Journal of Magnetism and Magnetic Materials*, Vol. 59, 1986, pp. 33-40.
- [31]. C. T. Chantler, Theoretical Form Factor, Attenuation and Scattering Tabulation for Z=1-92 from E=1-10 eV to E=0.4-1.0 MeV, *Journal of Physical and Chemical Reference Data*, Vol. 24, Issue 1, 1995, pp. 71-643.



Published by International Frequency Sensor Association (IFSA) Publishing, S. L., 2016
(<http://www.sensorsportal.com>).

10 Top Reasons

to Publish Open Access Books with IFSA Publishing



Publish your Open Access Book with IFSA Publishing
and get a tablet for free!

More details are available on IFSA Publishing's web site:
http://www.sensorsportal.com/HTML/IFSA_Publishing.htm

Today, many big and small publishers propose open access books publication. How IFSA Publishing open access books differ? Let to be focused on the main benefits:

- **The maximum number of pages is not limited.** Now you should not spend a lot of time and can eliminate additional efforts to put your manuscript in the limited number of page (for example, 350 pages). Create without limitations!
- **Very reasonable fixed price**, which does not dependent on the number of book pages. The publication fee is lower in comparison with other established publishers and is constant regardless of the number of pages.
- **High visibility.** All IFSA Publishing's books are listed on Sensors Web Portal (3,000 visitors per day) a primary Internet sensors related resource, increasing visibility and discoverability for your work. Information about published books also included in IFSA Newsletter (55, 000+ subscribers) and announced in professional LinkedIn Sensors Group (2,600+ members) at no additional charge to ensure the maximum possible distribution. As a result, citation rates of our authors are increased.
- **All book types accepted.** IFSA Publishing accepts complete monographs, edited volumes, proceedings, handbooks, textbooks, technical references and guides.
- **Available in different formats.** The open access eBook is freely available online and accessible to anyone with an internet connection at anytime. In addition to this free electronic version, a print (paper) edition (hardcover, paperback or dust jacket hardcover) in full color is offered for those who still wish to buy a printed book. Various book sizes are possible for print books. The book format is preliminary discussed together with authors. IFSA Publishing is the first publisher in the World who have started publish full-colour, print, sensors related books.
- **Freely available online.** IFSA Publishing's books are freely and immediately available online at Sensors Web Portal's web links upon publication and are clearly labeled as 'Open Access'. They are accessible to anyone worldwide, which ensures distribution to the widest possible audience.
- **Authors retain copyright.** IFSA Publishing's books are published under the Creative Commons Non-Commercial (CC BY-NC) license. It can be reused and redistributed for non-commercial purposes as long as the original author is attributed.
- **High quality standards.** IFSA Publishing's open access books are subject to the same high level peer-review, production and publishing processes followed by traditional IFSA Publishing's books.
- **Authors benefit from our IFSA Membership Program.** IFSA Publishing books charge an open access fee at the beginning of the publication process. Our payment IFSA Members receive a 10 % loyalty discount on this publication fee.
- **Authors free book copies and tablet.** Authors will get free print (paper) book copies (in full colour and one tablet 'Fire' from Amazon (Quad-Core processor, 1.3 GHz, 1 Gb RAM, 7" (17.7 cm), (1024 x 600), Wi-Fi, 8 GB) free of charge

Development of a Novel High Reliable Si-Based Trace Humidity Sensor Array for Aerospace and Process Industry

¹ Shuyao Zhou, ¹ Q. C. Dao, ¹ Biswajit Mukhopadhyay, ¹ Piotr Mackowiak, ^{1,4} Oswin Ehrmann, ^{1,4} Klaus-Dieter Lang, ² Michael Woratz, ² Peter Herrmann, ¹ T. Weiland, ³ Olaf Pohl, ³ Volker Noack, ^{1,3,*} Ha-Duong Ngo

¹ Fraunhofer Institute of Reliability and Microintegration, Berlin, Germany

² ACI GmbH, Berlin, Germany

³ University of Applied Sciences, Microsystems Engineering, Berlin, Germany

⁴ Technical University Berlin, Germany

* E-mail: ngo@izm.fraunhofer.de

Received: 5 November 2016 / Accepted: 5 December 2016 / Published: 30 December 2016

Abstract: In this paper we present high reliable and accurate silicon-based trace humidity sensors for use in aerospace and process industry. The sensors have been realized by using simple MEMS technology in this work. One is a single sensor (sensor cell) for monitoring of humidity, and sensor array is able to measure the total trace humidity in the atmosphere. It's very suitable for aerospace and process industry such pharmacy applications.

Keywords: MEMS, Micro sensors, Humidity sensor.

1. Introduction

Pressure, temperature and humidity are the three most measured physical properties. The question of moisture determination and control is an important one in many scientific and industrial disciplines. Trace humidity sensors are needed in many applications, such as Mars mission, semiconductor technologies, pharmaceutical processes.

The coulometric sensor principle [1] is normally used in trace humidity sensing (Fig. 1). This is one of the best techniques available for measuring water content of gases at very low concentration. Many liquids can also be analyzed by this technique after vaporization.

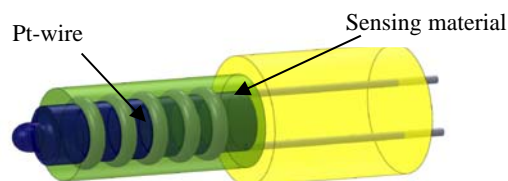


Fig. 1. Schematic view of a sensor on the market on glass carrier with Pt-wire and sensing material.

Other methods are generally unsuccessful when water concentrations to be measured are under a few thousand parts per millions. The common sensor concept is using glass carrier with Pt-wire and sensing material (phosphoric pentoxide P_2O_5). It is based on

the absorption of water vapour from the atmosphere by the highly hygroscopic phosphoric pentoxide (P_2O_5), which is located on the sensor between platinum electrodes. Realized sensors using glass carrier and thick film technology are robust but bulky and have some limitations such as reliability [1]. Another disadvantage of the concept is that – just one part of the water can be absorbed and electrolyzed.

2. Sensor Concept, Design and Technology

The single sensor concept is shown Fig. 2. The sensing Pt-electrode is deposited on a 3D silicon surface etched in silicon substrate in KOH-solution. The idea behind it is to increase the active surface of the sensing electrode in compare to a planar concept. The other advantage of this 3D concept is to use the capillary force to get the sensing material into the silicon trenches. The very smooth trench surface is very suitable for a thin high quality Pt electrode. The Pt layer shows no defects and non-perfections such as in standard sensors. Main disadvantage of this single sensor cell concept is the nonability to have exact information about the total humidity in the air like the concept in Fig. 1. Just one part of the water in the air can be absorbed and converted into charges. Sensors on the market need therefore a calibration. Fig. 3 shows the array concept. The sensor surfaces are exposed to the air flow. By adjusting the sensors voltages the signal of the last sensor can be adjusted toward zero – it means that the humidity in air is fully absorbed by the sensors. So it's very easy to measure the absolute humidity in the air without calibration. Another advantage of the array concept is a better redundancy.

The designed single sensor (sensor cell) has a size of $11.5 \text{ mm} \times 20 \text{ mm} \times 525 \mu\text{m}$, and the sensor array has dimensions of $60 \text{ mm} \times 20 \text{ mm} \times 525 \mu\text{m}$ [2-3]. The manufacturing technology is very simple using standard silicon MEMS processes. First the substrate is passivated by using double layers SiN and SiO. The thicknesses of SiO and SiN layer are 100 nm and 180 nm respectively. After that the double layer is structured as etching mask for following KOH etching (33 % KOH solution, 80°C). The etching rate is constant at $1 \mu\text{m}/\text{min}$. After KOH etching the mask is remove. Before Pt deposition by using sputtering a thin SiO was grown by using thermal oxidation. Purpose of this SiO layer is an isolation of Pt layer. Spray coating is used to make a lift-off mask for Pt deposition. After Pt sputtering the resist layer is removed.

The chemical reaction that takes place is an equilibrium process (Equation (1) and (2)).

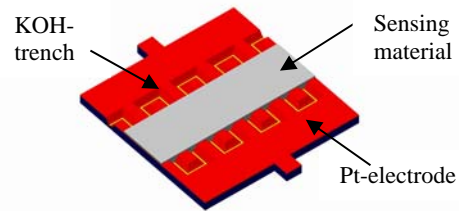
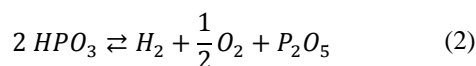


Fig. 2: Schematic view – single silicon-based humidity sensor in this work.

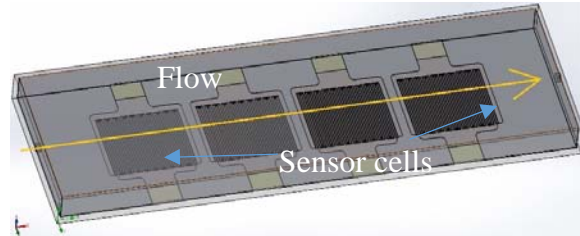


Fig. 3. Schematic design of the sensor array containing 4 single sensor cells for measurement of absolute humidity.

According to Faraday's law of electrolysis, 0.5 g/mole of water (9.01 g) requires 95.500 C of electricity for its electrolytic decomposition. The electrolysis current is proportional to the number of moles of water absorbed per unit time. Thus, measurement of water vapor mass is traced back to an electric current measurement [1]:

$$Q = I\Delta t = Fa = F \frac{m_{water}}{M_{water}} z, \quad (3)$$

where Q is the electric charge, I is the electric current, a is the absolute humidity, z is the number of exchange electrons, F is the Faraday constant 96484 As/mol, m_{water} is the mass of absorbed water vapor, M_{water} is the molar mass of water vapor.

The sensor current (charges) can be calculated by using the simple equation:

$$I = 1.0712104 * a * \dot{V}, \quad (4)$$

where a is the absolute humidity, \dot{V} is the gas flow.

A single measurement cell with a length of several meters would be necessary to achieve complete electrolysis of water in the carrying gas. Realized sensors have a conversion rate of $>30\%$. Normally calibration of these sensors is necessary because less than 100 % of the water vapor present take part in the reaction. In our array concept a calibration is not needed. The total amount of water in the air is the sum of the currents of all single sensor cells. Fig. 2 shows a concept with 4 sensor cells. One easy indicator for total reaction of water is the zero current in the last sensor cell in flow direction.

The sensor cells in this work are realized on a 3D surface etched in silicon substrate by using KOH. Such surface is much larger than 2D sensor surface typically

realized in thick film technology. The capillary effect on such 3D surface is also high which suitable to improve adhesion and contact between Pt- and P_2O_5 coating [2-3].

Another advantage of this concept is the better redundancy. Fail of one or more sensor cells do not affect the whole system function. The wearout of material on the first sensor is normally higher than on the other sensors. According to the absorbed mass of water from the air.

3. Fabrication

The sensor cells are fabricated by using standard silicon technology. First the alignment marks were etched in (100) silicon wafer. In the next step the deep trenches (100 μm) were etched by using KOH. After KOH etching the surface was passivated by a thick SiO_2 layer. For lift-off a spray coating for photo resist was necessary. Pt layer of 100 nm was sputtered. Fig. 4 shows briefly process steps for fabrication of the sensor array in silicon.

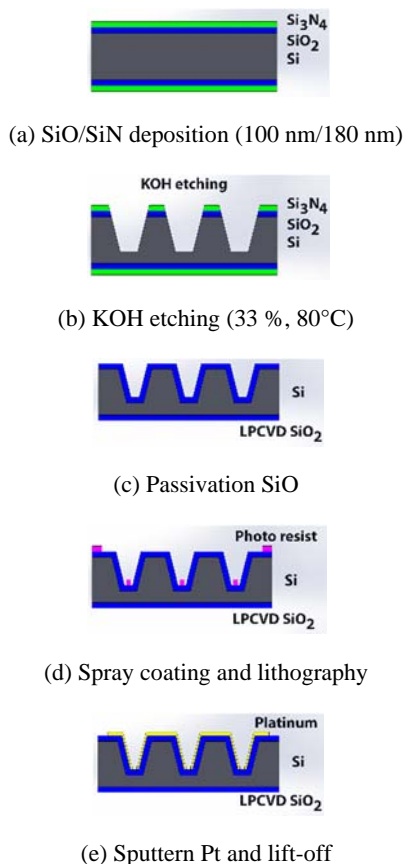


Fig. 4. Main process steps to fabricate the sensor array [3].

4. Characterization

Fig. 5 shows the top view of a realized sensor array with KOH-trenches and Pt-electrodes on top.

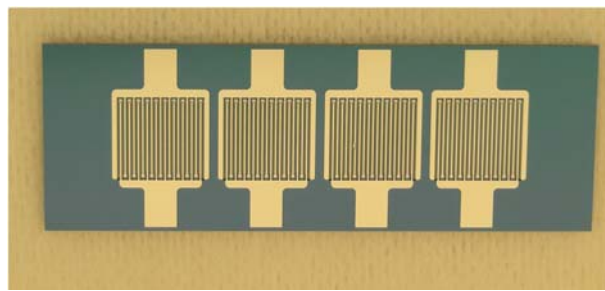


Fig. 5. Top view of the realized silicon-based sensor array without sensing material on top (60 mm \times 20 mm \times 525 μm).

Tests have been done to characterize the realized sensors. A special package has been realized to meet the requirements for monitoring of humidity [2]. In figure below the design of the package is shown. The design has totally four level. The first and second levels are the base plate and substrate to provide the stability and the sealing for the sensors. The third layer is a sealing membrane to create a hermetic in the flow channel over the sensor surface. The top level is a massive part over the sensor with the integrated channel. This part contains the connectors for supply gas flow and the pins for electrical contacts/interface. The design allows a laminar flow directly over the sensor surface. The Au pins are sealed and provide an easy electrical contact for sensor signal. The connector pins are equipped with springs to ensure an electrical connection at all times without damaging the sensors. Due to requirement for chemical resistance, the materials have to be chemically stable. The gas connection is created via stainless steel ports on the lateral edges of the structured plate. The structured plate is made of Polyethylene, the base substrate is made of FR-4 glass epoxy and the sealing layer is made of Viton. The realized system can be seen in Fig. 6. The system has a total size of 96 \times 50 \times 25 mm³ [2].

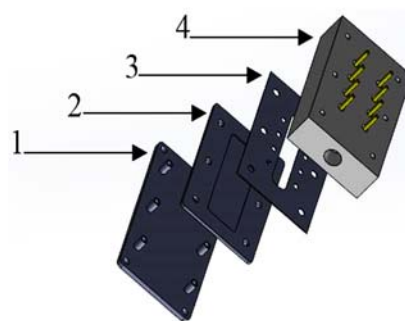


Fig. 6. Exploded view of the realized sensor package: (1) base plate; (2) base substrate; (3) sealing layer, and (4) plate with integrated flow path.

The realized sensor system is shown in Fig. 7.

The principle measurement set up in this work can be seen in Fig. 8.

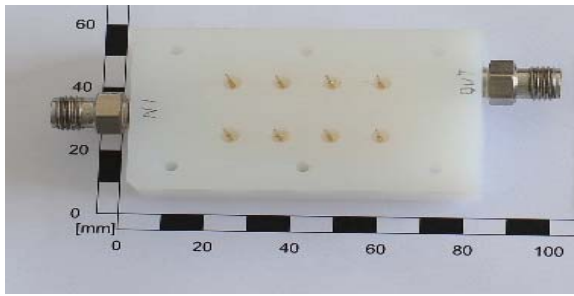


Fig. 7. Package for the sensor array.

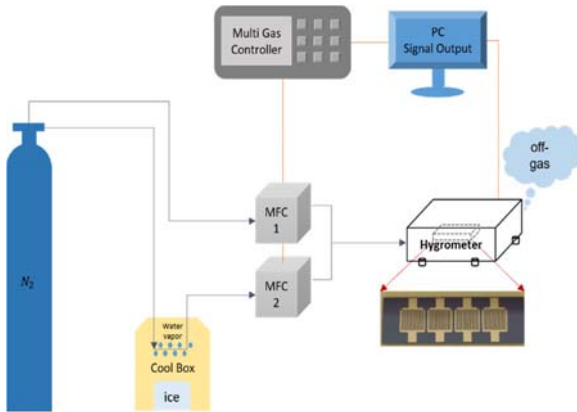


Fig. 8. Principle setup for characterization of the realized sensor arrays.

For the characterization nitrogen gas (N_2) with 99,999 % purity is used as gas supply based on its ideal behavior which follows Dalton's law of partial pressure at standard atmosphere. The dry nitrogen gas flow through Teflon tubing in two directions separately. One of them flow through the cool box with ice, which keep the condition of low humidity approx. 1000 ppm. In this case the humidity concentration can be calculated according to DIN 4108 [4]. The reference flow is mixed with dry air to create an air steam with specific humidity concentration for the characterization. The Fig. 9 shows the used set up.

The principle of generation of dew point in cool box is described in DIN 4108. For an ideal gas ($pV = nRT$) in thermal equilibrium is it possible to generate a reference gas steam with a dew point of about $t \sim -20^\circ C$ and a humidity concentration of 1000 ppm, as shown in Equation (5).

$$P_s [Pa] = 4.689 [Pa] \cdot \left(1.486 + \frac{t}{100^\circ C} \right)^{12.30} \quad (5)$$

$$(-20^\circ C < t < 0^\circ C, s. t. p.) \quad (6)$$

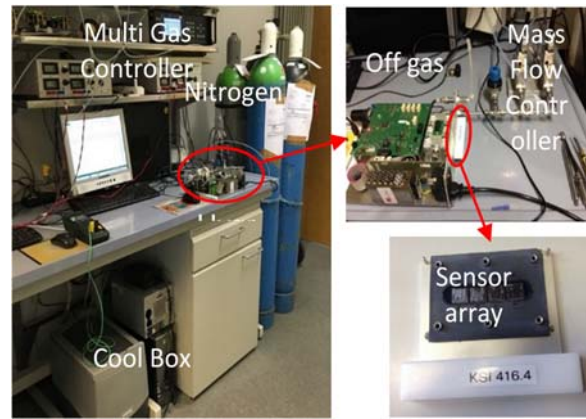


Fig. 9. Measurement setup for the sensor array.

Based on the Dalton's law of partial pressures shown in Equation (7), the reference gas flow is then mixed with dry air to create a gas flow with a specific humidity concentration. It is well known that the total pressure of a mixed gas is the sum of partial pressure of the individual gases.

$$P_{total} = P_1 + P_2 + \dots + P_n \quad (7)$$

If the mixture of gases containing water vapor, the total pressure is equal to the sum of the partial pressure of the dry gas and the partial pressure of the water vapor. The Equation (7) can be rewritten as:

$$P_{total} = P_d + P_w \quad (8)$$

The relationship between the total pressure (P_t) and the partial pressure of water vapor (P_w) can be expressed as follows [1]:

$$P_{t1}/P_{t2} = P_{w1}/P_{w2} \quad (9)$$

The quantity of any gas in a mixture can be expressed as a pressure. Controlling the gas pressure and temperature (cool box) is an easy way to control the water content. With the help of compressed air, the existing dew point can be converted to the dew point under atmospheric pressure – according to dew point diagram below (Fig. 10). It can be clearly seen in Fig. 10, for a temperature (cool box) of $-2^\circ C$ and a pressure of 4,2 bar a dew point of $-20^\circ C$ is achieved.

The ratio of dry gas and moist gas is well-controlled by using multi gas controller and mass flow controller. The mixture of gases flow over the sensor array, which was installed in hygrometer, to participate in chemical reaction. Therefore, the performance of sensor array with implementation from quantity of water vapor can be tested and determined.

The Table 1 shows the possible parameters set in this work.

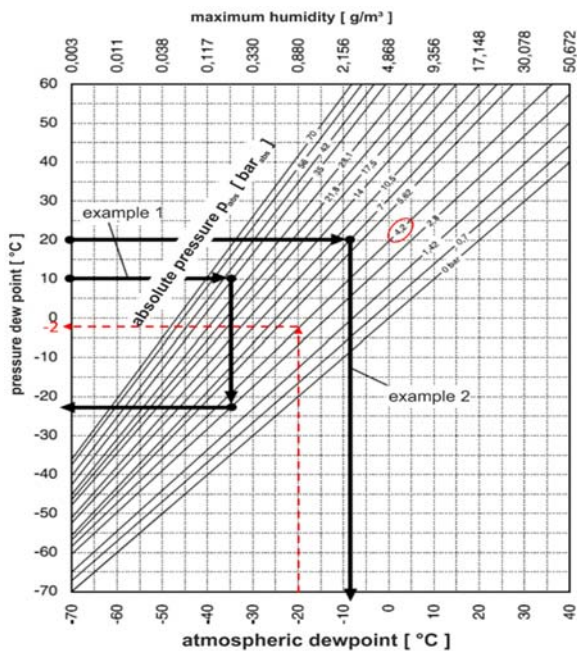


Fig. 10. Conversion diagram of dew point [1, 4].

Table 1. Parameters used in the characterization of the realized sensor arrays.

| Parameter | Value |
|--------------------------|---|
| Humidity measuring range | 10-1000 ppm _v |
| Dew point range | -60 ~ -20 °C |
| Ambient pressure | Approx. 1000 mbar |
| Ambient temperature | 24-29 °C |
| Flow rate | 20-150 ml/min |
| Mixture of gas | 99,999 % N ₂ H ₂ O < 2 ppm/mol |
| Cool box temperature | ca. -2 °C |
| Operating voltage | 40 V |

Coating of Sensor Material

The coating solution used in this work was phosphoric acid H₃PO₄ with 85 % concentration. For the characterization an amount of 0.5 μL phosphoric acid was dosed on each sensor cell. The sensor cells with coating were then cured at 50 °C for 30 min. Fig. 11 shows sensor array with coating after curing. In order to get the sensing materials better into the trenches a wetting step in O₂-plasma (5 min) was conducted prio coating.

For the characterization a flow rate of 50 ml/min was used. The electrical voltage was 40 V. Theory and measurement results are shown in Fig. 12. The electrolytic current behavior was a linear function of absolute humidity. At low absolute humidity till approx. 100 ppm, the agreement between theory and test results was excellent. Increasing the absolute humidity increases the difference of experimental current from theoretical current, which in accord with faraday's law. However, the range of deviation is acceptable. Discrepancy can be explained in the non-perfect setup.

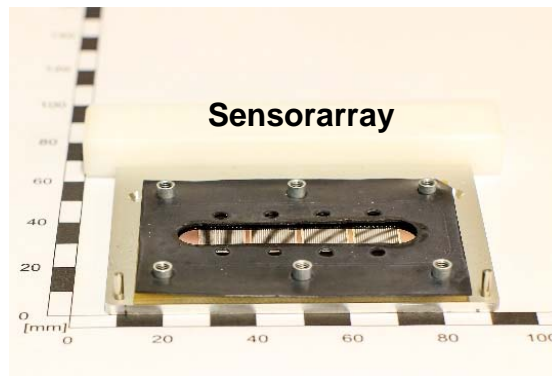


Fig. 11. Sensor array with coating ready for measurement.

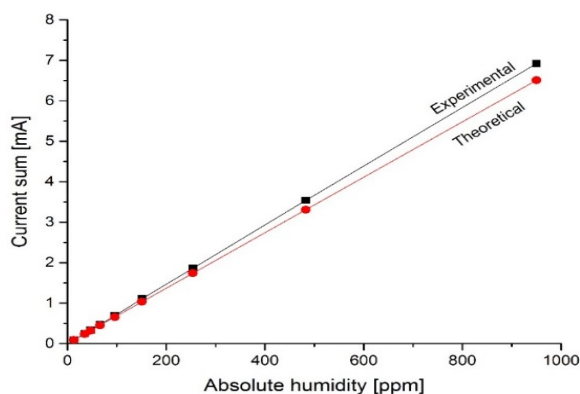


Fig. 12. Comparison of results of test and theory.

Fig. 13 shows the individual currents of individual sensor cells as functions of humidity. The current of the first sensor cell is the highest due to the higher absorbed humidity. The current of the last sensor cell is low indicating a very low humidity in the air flow above the last sensor cell. It shows that a complete electrolysis of water in the air is possible with the sensor array. Same effect could be achieved by adjusting the voltages for the individual sensor cells.

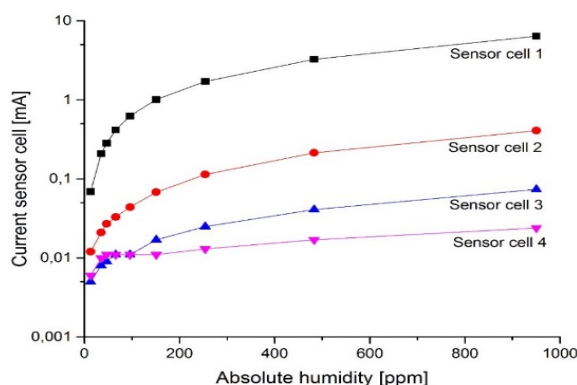


Fig. 13. Signals of individual sensor cells.

Many sensor arrays have been characterized in order to test the repeatability and robustness of the

technology. The Fig. 14 shows the output signals of three sensors as function of humidity. It shows a good repeatability.

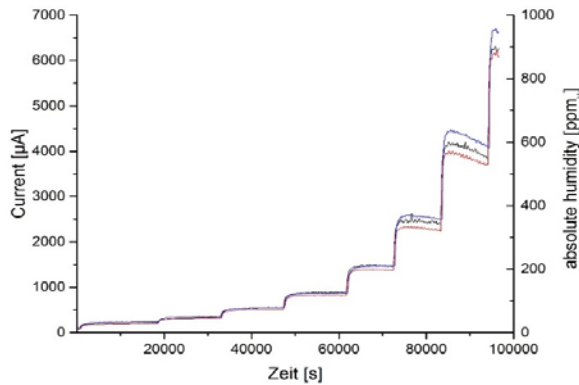


Fig. 14. Output signals of three sensors as function of humidity concentration up to 1000 ppm.

4. Conclusions

We present a novel reliable silicon-based sensor solutions for trace humidity. The single sensor cell can be used to monitor trace humidity as well as the sensor array. The sensor array can be used to monitor absolute water content in the air without calibration. The measurement results are verified and show quite good agreement with theory. The sensor package has been optimized by using simulation. The realized

prototype has a geometry of $96 \times 50 \times 25 \text{ cm}^3$. The simulation results show some limitation within the package. Improvements have been made to get better flow behavior over first sensor cell by modifying the flow path. The long flow path could be integrated in the package and can avoid backlash from air surrounded.

Acknowledgements

The authors would thank the BMWI and ZIM for founding of this project.

References

- [1]. R. Wernecke, Industrielle Feuchtemessung: Grundlagen, Messmethoden, technische Anwendungen, Wiley-VCH Verlag, 2005.
- [2]. H.-D. Ngo, *et al.*, Packaging solution for a novel silicon-based trace humidity sensor using coulometric method, in *Proceedings of the 18th IEEE Electronics Packaging Technology Conference*, Singapore, Dec. 2016, pp. 50-55.
- [3]. H.-D. Ngo, *et al.*, Novel High Reliable Si-Based Trace Humidity Sensor Array for Aerospace and Process Industry, in *Proceedings of the 2nd International Conference on Sensors and Electronic Instrumental Advances (SEIA'16) Conference*, Barcelona, Castelldefels, 22-23 September 2016, pp. 100-103.
- [4]. Dew Point Air Compressed Air Note B210991EN-B-LOW-v1.



Published by International Frequency Sensor Association (IFSA) Publishing, S. L., 2016 (<http://www.sensorsportal.com>).



International Frequency Sensor Association (IFSA) Publishing

ADVANCES IN SENSORS:
REVIEWS **1**

Modern Sensors, Transducers and Sensor Networks

Sergey Y. Yurish, Editor



Formats: printable pdf (Acrobat) and print (hardcover), 422 pages

ISBN: 978-84-615-9613-3,
e-ISBN: 978-84-615-9012-4

Modern Sensors, Transducers and Sensor Networks is the first book from the Advances in Sensors: Reviews book Series contains dozen collected sensor related state-of-the-art reviews written by 31 internationally recognized experts from academia and industry.

Built upon the series Advances in Sensors: Reviews - a premier sensor review source, the *Modern Sensors, Transducers and Sensor Networks* presents an overview of highlights in the field. Coverage includes current developments in sensing nanomaterials, technologies, MEMS sensor design, synthesis, modeling and applications of sensors, transducers and wireless sensor networks, signal detection and advanced signal processing, as well as new sensing principles and methods of measurements.

Modern Sensors, Transducers and Sensor Networks is intended for anyone who wants to cover a comprehensive range of topics in the field of sensors paradigms and developments. It provides guidance for technology solution developers from academia, research institutions, and industry, providing them with a broader perspective of sensor science and industry.

http://sensorsportal.com/HTML/BOOKSTORE/Advance_in_Sensors.htm

Preliminary Studies on Capacitive Proximity Sensing for Touchless Interaction with a Human Finger

* Leonhard HASLINGER and Bernhard G. ZAGAR

Johannes Kepler University Linz, Institute for Measurement Technology, Altenberger Straße 69,
4040 Linz, Austria

Tel.: +43 732 2468 5923, fax: +43 732 2468 5933

* E-mail: leonhard.haslinger@jku.at

Received: 5 November 2016 / Accepted: 5 December 2016 / Published: 30 December 2016

Abstract: This contribution deals with preliminary studies for touchless interaction based on capacitive sensor technologies. An existing approach in combination with additional capacitance measurements is used for position estimation. For that, a measurement system is utilized which is able to measure capacitances in a range of a few fF to several pF. The main focus is the 3D position estimation of a human finger through measuring the spatial capacitance distributions caused by its movements. A grounded metallic test object is used as an abstract model of a finger. The capacitance modeling is based on a 2D simplification by considering properties of symmetry. This new model, combined with complex data processing algorithms, ensures precise finger gesture recognition in future research.

Keywords: Modeling, 3D position estimation, Capacitive proximity sensors, Touchless interaction, Electric field.

1. Introduction

Numerous scientific publications in the context of touchless interaction, which are based on capacitive sensor technologies, deal with machine learning methods [1-2]. For an implementation of these algorithms empirical approximations, and a set of training data are often sufficient [3].

In contrast, this contribution uses a novel approach [4] that leads to a deeper physical understanding and model-based accurate algorithms for touchless interaction. Based on the proposed capacitance model 3D position estimation [5] can be implemented. Subsequently, tracking a sequence of positions should enable gesture recognition in future work. Here, a moderate spatial resolution of the measurement system is acceptable if the time resolution is sufficient to recognize smooth motions. The typically encountered small capacitance values and the rapid

capacitance changes caused by finger movements render the system sensitive to interferences. Concerning this matter the measurement and online evaluation of the data is challenging and already partly discussed in [6]. Furthermore, a variety of finger forms as well as numerous possible environmental conditions and disturbances are not considered. The main target regarding touchless interaction is to recognize the user's intention. In the case of incorrect interpretation an active feedback can inform the user how his behavior must be changed for a subsequent clear recognition.

Fig. 1 shows a schematic of the measurement set-up consisting of a sensing electrode with an area $a_s \times a_s$, a shielding electrode and a human finger. The surrounding volume is assumed as free space modeled with the permittivity ϵ_0 . For measurements, a grounded brass cuboid with an area $a_t \times a_t$ and a height h_t above the sensor plane is used as an abstract model

for an interacting finger, where the coordinates x_t , y_t and z_t describe the center position of its tip (denoted by an x in Fig. 1). In general, the human body capacitance to ground is about 150 pF [7]. This value is significantly larger than the maximal expected capacitance value¹ in the gesture sensing application. Therefore, a ground connected brass cuboid is a favorable simplification for a human finger.

The excitation signal is applied to the sensing electrode, which is used to measure the capacitance C_{3D} to ground. With a guard amplifier the shielding electrode is served to the same potential as the sensing electrode. Thereby, the effect or influence of parasitic capacitances is kept in check.

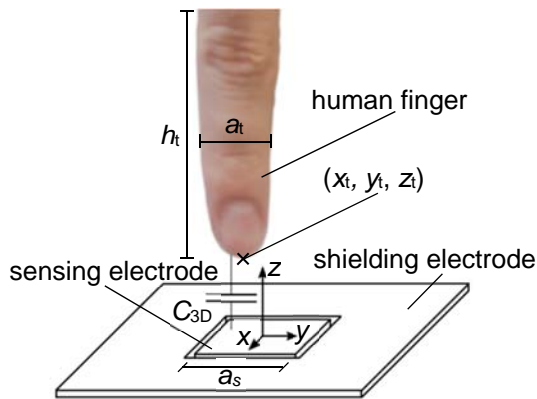


Fig. 1. Schematic of the measurement set-up.

Table 1 shows the values of the dimensions in Fig. 1 which are used for all the presented measurement data.

Table 1. Parameters for the measurement.

| Description | Parameter | Value |
|--------------------|-----------|-------|
| Width of electrode | a_s | 15 mm |
| Width of cuboid | a_t | 15 mm |
| Height of cuboid | h_t | 55 mm |

Due to symmetry properties, the 3D problem in Fig. 1 is presented as planar 2D problem in section 'Capacitance Modeling'. This configuration is divided in further parts for a mathematical description of the spatial capacitance distribution. These partial solutions of the 2D problem are combined for a 3D capacitance model. Section 'Capacitance Measurement' contains details concerning the measurement system, and the measured values are compared with the 3D capacitance model. Further, section 'Results' presents 3D position estimation as a basis for touchless interaction of a human finger. Finally, section 'Conclusion' discusses advantages and disadvantages as well as possible improvements for

¹ The parallel plate capacitor model at 1 mm plate distance yields 2 pF.

the 3D position estimation. Moreover, an outlook presents open problems for further studies.

2. Capacitance Modeling

Since an analytical calculation of C_{3D} in Fig. 1 is sophisticated, simplifications are useful. These simplifications are based on [8] and were partially discussed in [4].

2.1. 2D Modeling

Fig. 2 illustrates the abstraction of the measurement set-up in Fig. 1 as a planar problem in the xz -plane for $y = 0$. It is necessary to scale quantities in Fig. 2 with the spatial dimension a_y in y -direction to be consistent with Fig. 1. In Fig. 2 the corresponding human finger from Fig. 1 is assumed by a grounded metallic cuboid as test object. Furthermore, Fig. 2 splits the total capacitance into the capacitance C_b between the base of the cuboid and ground as well as the capacitances C_{sl} and C_{sr} between the left and right side of the cuboid and ground. The capacitance between the top side of the cuboid and ground is negligible. Therefore, the total capacitance C_{2D} between the sensing electrode and the cuboid follows as

$$C_{2D} = C_b + C_{sl} + C_{sr}, \quad (1)$$

where the x_t and z_t dependency of the capacitances is not denoted explicitly.

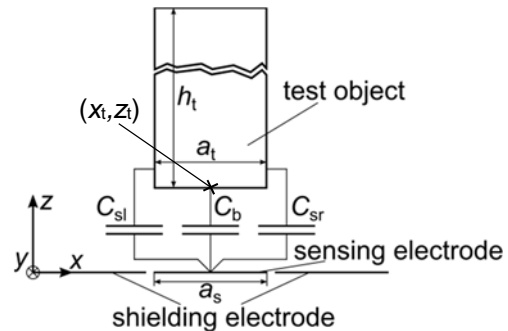


Fig. 2. Schematic of the planar problem.

For modeling C_b , C_{sl} and C_{sr} further simplifications are assumed:

- The spatial extension of the sensing and shielding electrode in z -direction are neglected.
- The gap between the sensing and the shielding electrode in the xy -plane is modeled as infinitesimally small.
- The shielding electrode extends infinitely in the xy -plane.

Modeling of C_b

The modeling of C_b is based on the geometry in Fig. 3. The superposition of two in x -direction differently shifted geometries in Fig. 3 follows in an approximation for C_b . The bottom Electrode 2 (red) and the bottom Shield 2 (blue) are part of the sensing and shielding electrode in Fig. 2. The top Electrode 1 (red) is part of the base area of the test object in Fig. 2. There is no equivalent for the top Shield 1 (blue), because it is used for virtual shielding of the partial capacitances C_{s1} and in the shifted case for the virtual shielding of the partial capacitance C_{sr} . Furthermore, the additional Shield 1 mainly results in a simplification for the mathematical calculation (superposition). At the point $x = x_1$ and $z = z_d$ Shield 1 ends and Electrode 1 begins and at point $x = x_2$ and $z = 0$ Electrode 2 ends and Shield 2 begins. Between the Electrodes 1 and 2 voltage U_{12} is applied. Moreover, the geometry is divided in part I ($x \leq x_1$) and part II ($x > x_1$) for a convenient calculation of the potential distribution.

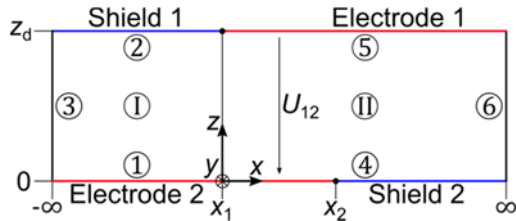


Fig. 3. Geometry definition for the modeling of C_b .

The potential φ within the electrode geometry in Fig. 3 follows as

$$\varphi(x, z) = \begin{cases} \varphi_I(x, z) & \text{for } x \leq x_1 \\ \varphi_{II}(x, z) & \text{for } x > x_1 \end{cases} \quad (2)$$

with the potential φ_I in part I and the potential φ_{II} in part II. The boundaries are divided into parts ① to ⑥ with the potentials given in Table 2.

Tab. 2. Parameters for the measurement.

| Boundary | x | z | φ |
|----------|-------------------------|---------------|------------------------|
| ① | $x \leq x_1$ | $z = 0$ | 0 |
| ② | $x \leq x_1$ | $z = z_d$ | 0 |
| ③ | $x \rightarrow -\infty$ | $0 < z < z_d$ | 0 |
| ④ | $x > x_1$ | $z = 0$ | 0 |
| ⑤ | $x > x_1$ | $z = z_d$ | U_{12} |
| ⑥ | $x \rightarrow \infty$ | $0 < z < z_d$ | $U_{12} \frac{z}{z_d}$ |

For the unique solution of the Laplace's equation [9]

$$\Delta\varphi(x, z) = 0 \quad (3)$$

additional constraints at the transition between part I and II are necessary. These are the Dirichlet condition

$$\varphi_I(x_1, z) = \varphi_{II}(x_1, z) \text{ for } 0 < z < z_d \quad (4)$$

and the Neumann condition

$$\frac{d\varphi_I(x_1, z)}{dx} = \frac{d\varphi_{II}(x_1, z)}{dx} \text{ for } 0 < z < z_d \quad (5)$$

To obtain a solution of (3) for the boundary conditions listed in Table 2 and the transition conditions (4) and (5) a separation of variables is suggested in [8]. This leads to the partial potentials φ_I and φ_{II} represented as

$$\varphi_I(x, z) = \frac{U_{12}}{\pi} \sum_{n=1}^{\infty} \frac{(-1)^{n+1}}{n} e^{-\frac{n\pi|x-x_1|}{z_d}} \sin\left(\frac{n\pi z}{z_d}\right) \quad (6.a)$$

$$\varphi_{II}(x, z) = U_{12} \frac{z}{z_d} - \varphi_I(x, z) \quad (6.b)$$

Besides, with (6) the surface charge density σ_2 on Electrode 2 in Fig. 3 follows through

$$\sigma_2(x) = -\epsilon_0 \frac{\partial\varphi(x, 0)}{\partial z} = -\epsilon_0 \frac{U_{12}}{z_d} \frac{e^{-\frac{\pi(x-x_1)}{z_d}}}{1 + e^{-\frac{\pi(x-x_1)}{z_d}}} \quad (7)$$

The superposition of the electric fields for the configuration in Fig. 3 with

$$x_1 = x_t - \frac{a_t}{2}, x_2 = \frac{a_s}{2} \quad (8)$$

and another configuration with an inverted potential distribution at the boundaries

$$x_1 = x_t + \frac{a_t}{2}, x_2 = -\frac{a_s}{2} \quad (9)$$

results in the field distribution, which is necessary for modeling C_b in Fig. 2. Consequently, the charge density σ_s on the sensing electrode is described by

$$\sigma_s(x) = -\sigma_2(x)|_{x_1=x_t-\frac{a_t}{2}} + \sigma_2(x)|_{x_1=x_t+\frac{a_t}{2}} \quad (10)$$

through superposition. By means of (10) the electric charge Q_s on the sensing electrode follows as

$$Q_s = a_y \int_{-\frac{a_s}{2}}^{\frac{a_s}{2}} \sigma_s(x) dx \quad (11)$$

Thereby, C_b can be calculated over the capacitance definition

$$C_b = \frac{Q_s}{U_{12}} \quad (12)$$

to

$$C_b = a_y \frac{\epsilon_0}{\pi} \ln\left(\frac{\cosh(k_{b1})\cosh(k_{b2})}{\cosh(k_{b3})\cosh(k_{b4})}\right) \quad (13)$$

with x_t and z_t dependence parameter k_{b1} , k_{b2} , k_{b3} and k_{b4} . Through the expressions

$$k_{b1} = \frac{\pi}{4z_t} (2x_t - a_s - a_t), \quad (14.a)$$

$$k_{b2} = \frac{\pi}{4z_t} (2x_t + a_s + a_t), \quad (14.b)$$

$$k_{b3} = \frac{\pi}{4z_t} (2x_t + a_s - a_t), \quad (14.c)$$

$$k_{b4} = \frac{\pi}{4z_t} (2x_t - a_s + a_t) \quad (14.d)$$

these parameters are determined. Assuming the same width $a_t = a_s$ (cf. Tab. 1) for the test object and the sensing electrode, C_b can be simplified to

$$C_b = a_y \frac{\epsilon_0}{\pi} \ln \left(\frac{1}{2} \cosh \left(\frac{\pi a_s}{z_t} \right) + \frac{1}{2} \right) \quad (15)$$

at $x_t = 0$. For $a_s/z_d \gg 1$ the capacitance C_b results in the well known parallel plate capacitor model

$$C_b \approx \epsilon_0 \frac{a_y a_s}{z_t} \quad (16)$$

Modeling of C_{sl} and C_{sr}

The conformal map f from [9-10] expressed as

$$t = f(s) = \ln(s) \quad (17)$$

in Fig. 4 is the basis for the approximation of C_{sl} and C_{sr} . This conformal map is a transformation from the s -plane

$$s = x + jz \quad (18)$$

into the t -plane

$$t = \xi + j\zeta \quad (19)$$

Fig. 4 shows the relation between the radial geometry with the radii r_{o1} , r_{o2} , r_{u1} and r_{u2} as well as the angle α in the s -plane and the problem in the t -plane. The problem in the t -plane is equivalent to the planar problem for the calculation of C_b before (cf. Fig. 2).

For calculating C_{sr} with (17) three geometrical sections of the form

$$\text{section 1: } -\frac{a_s + a_t}{2} > x_t, \quad (20.a)$$

$$\text{section 2: } -\frac{a_s + a_t}{2} \leq x_t < \frac{a_s - a_t}{2}, \quad (20.b)$$

$$\text{section 3: } \frac{a_s - a_t}{2} \leq x_t \quad (20.c)$$

are distinguished. The sections are referenced via the x -position x_t of the test object.

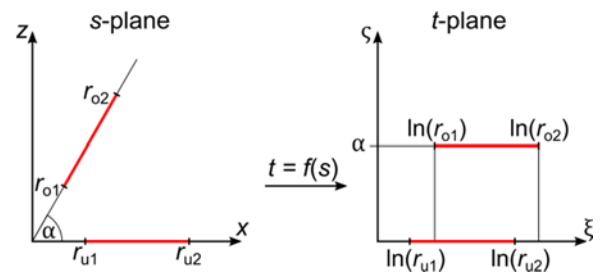


Fig. 4. Conformal map from s -plane into t -plane.

Fig. 5 depicts a schematic of Sections 1 and 2. There is a relative coordinate system with axes x' and z' , that moves in x -direction with the test object.

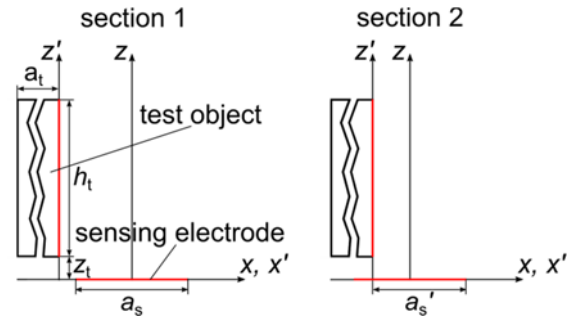


Fig. 5. Schematic of Sections 1 and 2.

Hence, the parameters in Fig. 4 for Section 1 follow as

$$r_{o1} = z_t, \quad r_{o2} = r_{o1} + h_t \quad (21.a)$$

$$r_{u1} = -\frac{a_s + a_t}{2} - x_t, \quad r_{u2} = r_{u1} + a_s \quad (21.b)$$

$$\alpha = \frac{\pi}{2} \quad (21.c)$$

In Section 2 the effective width of the sensing electrode is reduced from a_s to a'_s . The parameters in Fig. 5 are given by

$$r_{u1} = 0, \quad r_{u2} = a'_s \quad (22)$$

whereby (21.a) and (21.c) do not change. Section 3 is not part of Fig. 5 because there is $a'_s = 0$ and the parameters are determined by

$$r_{u1} = 0, \quad r_{u2} = 0, \quad (23)$$

thus not contributing any capacitance. Further, with (21), (22) and (23) in the t -plane (cf. Fig. 4) the equivalent problem must be solved for the capacitance calculation for C_b . Analogously to (13) and (14) the capacitance C_{sr} results in

$$C_{sr} = a_y \frac{\epsilon_0}{\pi} \ln \left(\frac{\cosh(k_{sr1}) \cosh(k_{sr2})}{\cosh(k_{sr3}) \cosh(k_{sr4})} \right) \quad (24)$$

and with (21), (22) and (23)² for the parameters k_{sr1} , k_{sr2} , k_{sr3} and k_{sr4} the expressions

$$k_{sr1} = \frac{\pi}{2\alpha} (\ln(r_{u2}) - \ln(r_{o1})) \quad (25.a)$$

$$k_{sr2} = \frac{\pi}{2\alpha} (\ln(r_{u1}) - \ln(r_{o2})) \quad (25.b)$$

$$k_{sr3} = \frac{\pi}{2\alpha} (\ln(r_{u1}) - \ln(r_{o1})) \quad (25.c)$$

$$k_{sr4} = \frac{\pi}{2\alpha} (\ln(r_{u2}) - \ln(r_{o2})) \quad (25.d)$$

follow. The reduction of the effective width of the sensing electrode from a_s to a_s' causes negligible partial capacitances. Moreover, in Section 3 capacitance contributions are completely omitted and therefore $C_{sr} = 0$. The capacitance calculation for C_{sl} can be done in the same way as for C_{sr} in (24) and (25).

2.2. 3D Modeling

To evaluate the validity of the derived 2D model approximating the 3D reality some further investigations are necessary.

Fig. 6 shows the capacitance contour lines³ of C_{3D} for $z_t = 2$ mm and $z_t = 5$ mm in the xy -plane.

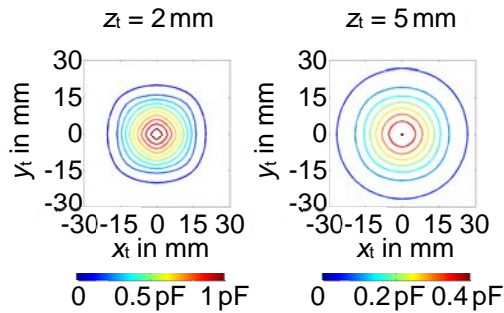


Fig. 6. Contours of C_{3D} for $z_t = 2$ mm and $z_t = 5$ mm.

As a consequence of the rectangular forms of sensing electrode and test object the contours differ from the circular form in the short range (see Fig. 6 for $z_t = 2$ mm). For larger distances the capacitance contours are nearly circular (see Fig. 6 for $z_t = 5$ mm).

Therefore, an approximation for the 3D capacitance model C_{3D} follows as

$$C_{3D}(x_t, y_t, z_t) = C_{2D}(\sqrt{x_t^2 + y_t^2}, z_t) \quad (26)$$

In the following this approach is used for small as well as for large distances and the validity is verified by measurements.

3. Capacitance Measurement

Fig. 7 shows the measurement system consisting of a 3-axis translation stage, the test object, the sensing electrode array and the extended OpenCapSense hardware with eight channels [6, 11]. The 3-axis system has an accuracy in the submillimeter range. The requirements for the capacitance measurement system were a small uncertainty (around ± 15 fF) and a wide measurement range (a few fF to several pF) combined with a moderate temporal resolution (≤ 5 ms processing time per sensor).

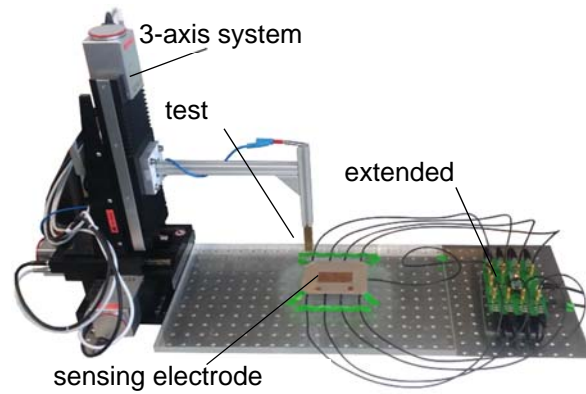


Fig. 7. Measurement system.

Fig. 8 illustrates the single and multi electrode structures (a) and (b) used as well as the grounded brass cuboid which represents a human finger. The sensing electrodes are made of a double sided PCB (printed circuit board) with an additional nanosilver imprinted PET foil at the top [12]. The sensor array (b) is based on a multilayer structure in order to circumvent interference artifacts and guarantee high symmetry.

To achieve a precise 3D localization of the test object several capacitance sensors must be combined to increase the spatial resolution (e.g., eight sensing electrodes in Fig. 8 (b)). In the set-up each electrode is connected to a separate measuring channel. The output signal of an astable multivibrator excites the sensing electrode and C_{3D} is proportional to the period of this signal. The combination of multiple sensing electrodes would decrease the accuracy for a simultaneous measurement of all channels, because the electrodes influence each other. Therefore, the sensing electrodes

² This is the trivial case $C_{sr} = 0$.

³ A contour line of a function of two variables is a curve along which the function has a constant value. It is a cross-

section of the three-dimensional graph of the function $f(x,y)$ parallel to the xy -plane.

are evaluated sequentially. While the capacitance C_{3D} of each sensing electrode is measured all other sensing electrodes are served to the same electrical potential as the active one to eliminate the influence of parasitic capacitances between the active and inactive sensing electrodes.

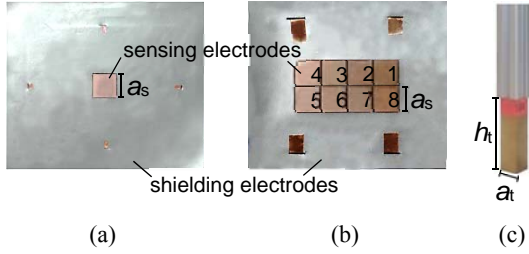


Fig. 8. Single electrode structure (a); multi electrode structure (b), and brass cuboid (c).

The left part of Fig. 9 shows a comparison of the measurement and the 3D capacitance model (26) for C_{3D} in the xz -plane. The right part illustrates the absolute deviation between measurement and model. The essential physical phenomena which are responsible for C_{3D} (cf. Fig. 1) are accurately described with (26) in the xz -plane. The absolute deviation in the short range is less than 50 fF and for larger distances much smaller (in the range of the

noise). Although, in the short range the absolute deviation is highest the relative deviation is low because of the large capacitance values through the $1/z$ distance characteristics. Conversely, for larger distances the relative deviation increases.

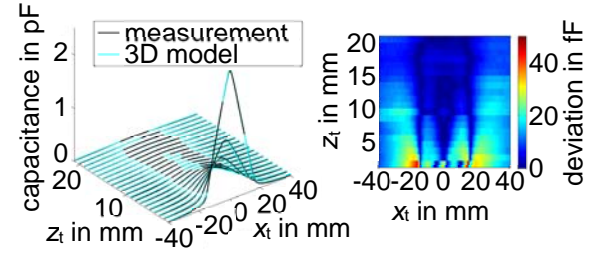


Fig. 9. Comparison of measurement and model for C_{3D} in the xz -plane.

Fig. 10 shows a comparison between the measurement and the 3D capacitance model (26) for C_{3D} at $z_t = 5$ mm in the xy -plane. The idealizations concerning the contour lines in Fig 6 cause additional deviations in comparison to the result depicted in Fig. 9. Nevertheless, Fig 10 shows that the 3D capacitance model is a good approximation for the measurement.

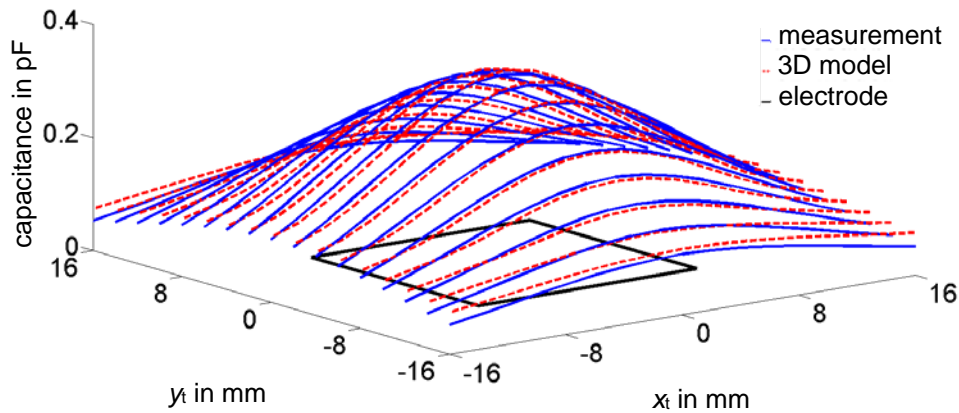


Fig. 10. Comparison of measurement and model for C_{3D} at $z_t = 5$ mm in the xy -plane.

4. Results

With the measured capacitance values and (26) the center position of the cuboid's base can be estimated via the formulation of an optimization problem for the measuring position as shown in preliminary studies [5]. At every sample interval the problem is viewed as quasi-stationary, and the minimization problem follows as

$$\min_{x_t, y_t, z_t} \sum_i \left(C_{m,i} - C_{3D,i}(x_t, y_t, z_t) \right)^2 \quad (27)$$

with the measured capacitance values $C_{m,i}$ and the modeled capacitance values $C_{3D,i}$ in (26) for each measuring channel $i \in \{1..8\}$. Only the four largest capacitance values of the eight channels are used in (27) to guarantee an overdetermined well-posed problem. If further capacitance values are larger than 80 % of the least value of the initial four those are also considered to further improve the estimation.

The left part of Fig. 11 illustrates the deviation between the x -coordinates of the estimation and the true value of the cuboid's base while the right part of Fig. 11 shows the deviation between the y -coordinates. The increasing deflection in the far field

of the electrodes in Fig. 11 is caused by simplifications in the 3D capacitance model (26). Furthermore, there are also limitations of accuracy concerning the extended OpenCapSense hardware [6, 11]. The

processing of the measured data by the new approach [4] results in very slight deviations from the true values (< 5 mm) close to the sensor electrodes.

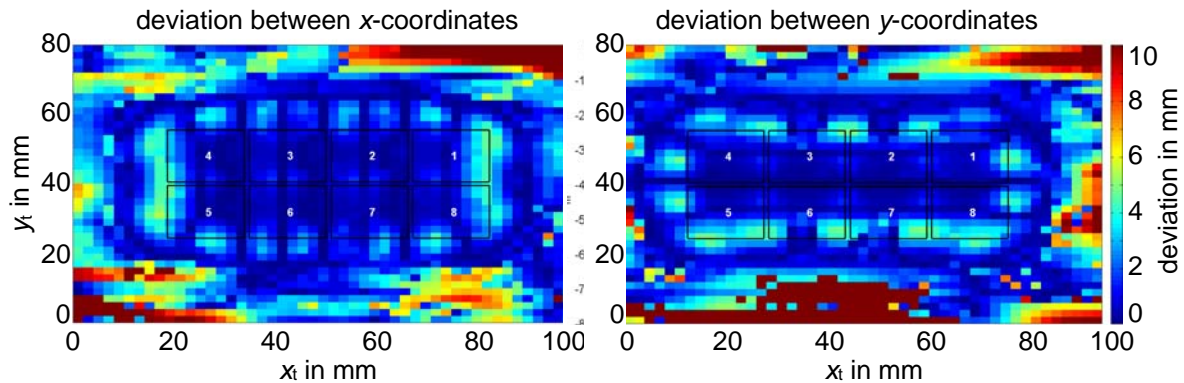


Fig. 11. Deviation of the estimated position of the coboid's base at $z_t = 1$ mm for x_t and y_t .

5. Conclusion

The approach used in this article can be a good basis for touchless gesture estimation of a human finger. As shown in Fig. 11 the absolute position error attainable for estimation employing the functional (27) is < 5 mm which is sufficient for a wide variety of pointing tasks. The moderate spatial resolution is sufficient still if the resolution in time is good enough to be able to follow smooth motions denoting typical swipe gestures or hand-wave gestures. Here, wipe gestures (e. g., up and down, left and right, circular forms, etc.) as known from smartphone interaction are of interest to be recognized as a user's intention. If necessary for further studies adopting parameters might be able to help to decrease absolute position errors. However, the main focus concerning capacitive proximity sensing for touchless interaction of a human finger is the application in a human machine interface.

Also an interesting point to be addressed in a future work is to investigate the validity of the assumption of a grounded metallic object as finger model and the conditions so that these this simplifications hold.

Currently the optimization problem in (27) is solved offline. Here, methods must be developed to ensure online finger gesture recognition in future research.

Acknowledgements

The authors gratefully acknowledge the partial financial support for the work presented in this paper by the Austrian Research Promotion Agency (FFG) under contract grant 846057 and WimTec Sanitärprodukte GmbH. Furthermore, we thank Simon Hehenberger for recording the measurement data.

References

- [1]. A. Braun, *et al.*, Capacitive sensor-based hand gesture recognition in ambient intelligence scenarios, in *Proceedings of the 6th International Conference on 'Pervasive Technologies Related to Assistive Environments'*, Rhodes, Greece, 29-31 May 2013, Article No. 5.
- [2]. T. Große-Puppenthal, *et al.*, Classification of User Postures with Capacitive Proximity Sensors in AAL-Environments, in *Proceedings of the International Joint Conference on Ambient Intelligence (Aml)*, Springer, Vol. 7040, 2011, pp. 314-323.
- [3]. T. Große-Puppenthal, *et al.*, Honeyfish - A High Resolution Gesture Recognition System based on Capacitive Proximity Sensing, in *Proceedings of the Embedded World Conference*, Weka Fachmedien, 2012, pp. 1-10.
- [4]. L. Haslinger, B. G. Zagar, Voruntersuchungen zur berührungslosen Gestenerkennung mittels kapazitiver Sensorik, in *Proceedings of the 18th GMA/ITG Conference on 'Sensors and Measurement Systems'*, Nürnberg, Germany, 10-11 May 2016, pp. 210-217.
- [5]. L. Haslinger, B. G. Zagar, 3D Position Estimation with Capacitive Sensors for Touchless Interaction, in *Proceedings of the 2nd International Conference on 'Sensors and Electronic Instrumentation Advances (SEIA' 2017)*, Barcelona, Castelldefels, Spain, 22-23 September 2016, pp. 123-127.
- [6]. L. Haslinger, *et al.*, Capacitance Measurement System for Touchless Interaction, in *Proceedings Eurosensor 2016*, Budapest, Hungary, 4-7 September 2016, pp. 1071-1074.
- [7]. G. Durcansky, EMV-gerechtes Gerätedesign, Franzis Verlag GmbH, 1999. ISBN-10: 3772353886.
- [8]. G. Willem de Jong, Smart Capacitive Sensors, Dissertation, *Delft University of Technology*, 1994.
- [9]. P. Henrici, Applied and Computational Complex Analysis, *John Wiley & Son*, 1974.
- [10]. N. Eidenberger, Konforme Abbildungen zur Lösung ebener inverser Probleme in der Messtechnik, Dissertation, *Johannes Kepler University Linz*, 2014.

[11]. T. Grosse-Puppenthal, *et al.*, OpenCapSense: A Rapid Prototyping Toolkit for Pervasive Interaction using Capacitive Sensing, in *Proceedings of the IEEE International Conference on Pervasive Computing and Communications*, San Diego, 2013, pp. 151-158.


[12]. C. Beisteiner, B. G. Zagar, Electrical and mechanical characterization of inkjet-printed functional structures, *tm - Technisches Messen*, Vol. 83, Issue 11, 2016.



Published by International Frequency Sensor Association (IFSA) Publishing, S. L., 2016 (<http://www.sensorsportal.com>).

Universal Sensors and Transducers Interface (USTI)

for any sensors and transducers with frequency, period, duty-cycle, time interval, PWM, phase-shift, pulse number output

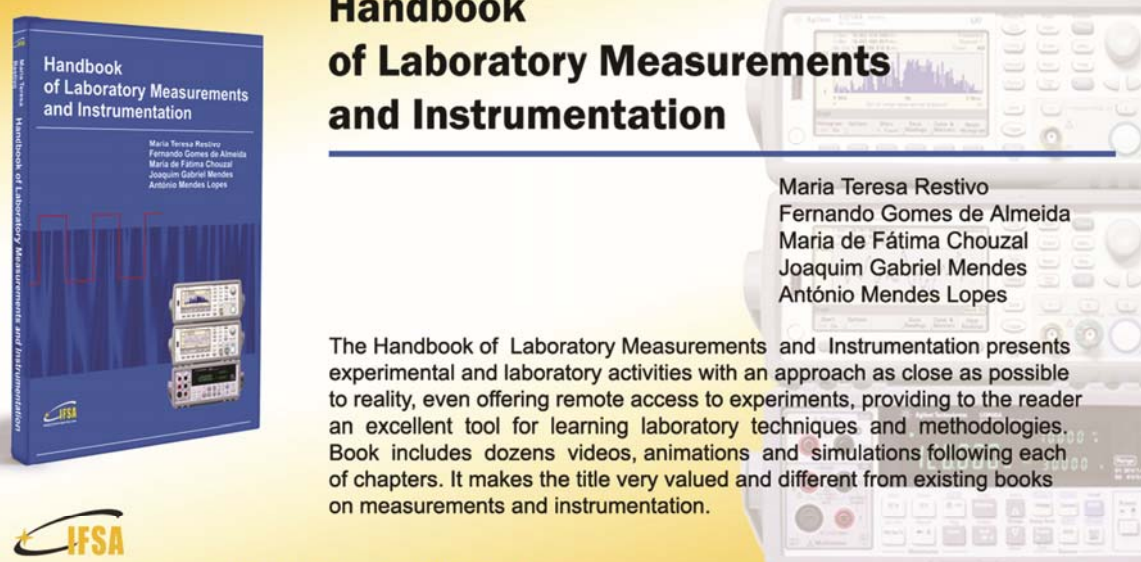


- * Input frequency range: 0.05 Hz ... 9 MHz (144 MHz)
- * Selectable and constant relative error: 1 ... 0.0005 % for all frequency range
- * Scalable resolution
- * Non-redundant conversion time
- * RS232, SPI, I2C interfaces
- * Rotational speed, *rpm*
- * Cx, 50 pF to 100 μ F
- * Rx, 10 Ω to 10 M Ω
- * Pt100, Pt1000, Pt5000, Cu, Ni
- * Resistive Bridges
- * PDIP, TQFP, MLF packages

Just make it easy !

<http://excelera.io/> info@excelera.io

Handbook of Laboratory Measurements and Instrumentation



Maria Teresa Restivo
Fernando Gomes de Almeida
Maria de Fátima Chouzal
Joaquim Gabriel Mendes
António Mendes Lopes

The Handbook of Laboratory Measurements and Instrumentation presents experimental and laboratory activities with an approach as close as possible to reality, even offering remote access to experiments, providing to the reader an excellent tool for learning laboratory techniques and methodologies. Book includes dozens videos, animations and simulations following each of chapters. It makes the title very valued and different from existing books on measurements and instrumentation.

IFSA
International Frequency Sensor Association Publishing

Order online:
http://www.sensorsportal.com/HTML/BOOKSTORE/Handbook_of_Measurements.htm

Vector Magnetometer Application with Moving Carriers

**Andrii PRYSTAI, Valery KOREPANOV, Fedir DUDKIN
and Borys LADANIVSKYY**

LLC Laboratory for Electromagnetic Innovations (LEMI), 5-A Naukova Str., Lviv, 79060, Ukraine
Tel.: + 380322639163, fax: + 380322639163
E-mail: vakor@isr.lviv.ua

Received: 5 November 2016 /Accepted: 5 December 2016 /Published: 30 December 2016

Abstract: In magnetic prospecting the aeromagnetic survey is a widespread method used for research in large territories or in the areas with difficult access (forests, swamps, shallow waters). At present, a new type of mobile carriers – remotely piloted vehicles or drones – is becoming very common. The drones supplied by magnetometer can be also used for underground utility location (for example, steel and concrete constructions, buried power cables, to name a few). For aeromagnetic survey, obtaining of 3-component magnetic field data gives higher processing precision, so the fluxgate magnetometers (FGM) seem to be the most preferable by reason of low weight, noise, power consumption and costs. During movement of FGM fixed to a drone practically permanent attitude changes in the Earth's magnetic field arises with corresponding changes of its projection at FGM axes. Also the electromagnetic interference from the drone motor and uncontrolled oscillations of drone and suspension are the factors which limit the magnetometer sensitivity level. Aroused because of this, signals significantly exceed the expected signals from a studied object and so should be removed by proper interference filtration and use of stabilized towed construction, as well as at data processing. To find the necessary resolution threshold of a drone-portable FGM, the modeling was made to estimate magnetic field value from a small sphere about 1 cm radius at the minimal altitude of drone flight and it was shown that such a small object can be reliably detected if the FGM noise level is less than 0.15 nT. Next requirement is the necessity to decrease as much as possible the FGM power consumption with retention of low noise level. Finally, because of drone movement, the broadening of a frequency range should be done. The LEMI-026 magnetometer was developed satisfying all requirements to the drone-mounted device. The field tests were successfully performed using two of LEMI-026 magnetometers and it was concluded that the parameters of these magnetometers allow their using for the magnetic survey with moving platforms.

Keywords: Drone, Flux-gate magnetometer, Aeromagnetic survey, Modeling, Test results.

1. Introduction

Geological/geophysical prospecting magnetometry is widely used method which is based on the difference in the magnetic properties of soils and rocks (see, for example, [1]). Magnetic prospecting studies the magnetic anomalies produced by geological bodies that have been magnetized by present-day (induced magnetization) and ancient (residual magnetization)

geomagnetic fields. Their magnetization is determined by the presence of ferromagnetic minerals (for example, magnetite, pyrrhotite). In magnetic prospecting the aeromagnetic survey is a widespread method for large territories or in the areas with difficult access (forests, swamps, shallow waters).

Till recently, it was realized mostly with specialized planes and helicopters. At present, a new type of such carriers – remotely piloted vehicles or

drones – is becoming more common. Additionally to the mining exploration and regional geophysical studies, they allow solving much wider spectrum of tasks. For example, it is a location of the archeological sites, where the alteration and concentration of weakly magnetic minerals to fine grained iron oxides, such as magnetite or maghaemite, during human activity lead to the increase of soil magnetic susceptibility [2-4]. The soil magnetic properties mapping is necessary for: application of soil compensation techniques for the detection of buried metallic objects (UXO, EOD, landmines etc.) using electromagnetic sensors; study the effect of small scale spatial variation of soil magnetic susceptibility [5-6]. Digital soil mapping can contribute significantly to prediction of the soil spatial and parameter distribution in the landscape using models. Initially soils were mapped as class maps (i. e. soil types) but increasingly property maps can be developed, [7-8]. The wetlands aeromagnetic inspection with drones is applicable for archaeology, agriculture and civil works [2, 9-12]. Metal debris and contamination detection are required at landfill mining and reclamation when wastes (metal debris and scrap) and contaminated by heavy metals soil are excavated and processed at soil remediation [13-15]. Also drones supplied by magnetometer can be used for underground utility location (for example, steel and concrete constructions, buried DC and AC power cables, to name a few). For these purposes the magnetometer with frequency range DC-AC up to 60 Hz is necessary [16-18].

The magnetic field of buried detected/located objects or soil inhomogeneities is too weak, even in close proximity of the earth's surface, and needs for reliable detection very sensitive magnetometers. Also at surveying of large areas a mobile lightweight device for productive and low cost measurements is necessary. Now, at magnetic prospecting the most used are the scalar magnetometers which have a very high sensitivity and some of them have a moderate mass for application with drones. For example, Cesium-vapor magnetometer G-822A has noise less than 0.001 nT/ $\sqrt{\text{Hz}}$ rms at a 0.1 second sample rate, sensor and electronic module weight 339 and 623 g respectively [19]. However, the scalar magnetometers have essential drawback because of absolute value magnetic field measurement, which limits the possibilities of data interpretation by application of methods for inverse problem solution.

For obtaining of 3-component magnetic field data, the fluxgate magnetometers (FGM) seem to be the most preferable by reason of low weight, noise, power consumption and costs. For example, FGM designed for drone application has noise less than 0.02 nT/ $\sqrt{\text{Hz}}$ rms at 1 Hz, sample rate 200 Hz, power consumption 6 W, sensor and electronic weight 200 and 500 g respectively [20]. There is no information about data collection system for this FGM, and its power consumption is too high for small portable batteries. So, the adaptation of FGMs for the measurement onboard such a small size and low-powered carriers implies further more stringent requirements to their

technical parameters. Other hindrance, resulted from instability of FGM axes orientation and distance to boundary air-ground during magnetic prospecting, strongly impedes the measuring procedure and data interpretation [21]. This problem still waits for new theoretical investigations and experimental ideology, which will allow obtaining the final results with high accuracy.

2. Problems of FGM Application for Moving Carriers

During movement of suspended or fixed FGM on a drone practically permanent attitude changes in the Earth's magnetic field \mathbf{B}_0 arises. The corresponding changes of \mathbf{B}_0 projection on FGM axes significantly exceed the expected signal from a studied object and so should be removed at data processing. For example, the sensor deviation at as tiny angle as 0.01° may lead to the appearance of parasitic signal up to 5-12 pT. At the same time the minimal anomalous magnetic field at geomagnetic prospecting can be of value about

$$B_{\min} \sim \kappa B_0 \approx 10^{-5} B_0 = 0.3 - 0.7, \text{ pT}, \quad (1)$$

where κ is the soil magnetic susceptibility [22], $B_0 = |\mathbf{B}_0|$.

The appropriate FGM orientation in flight is hardly ever can be controlled for such small carriers. Nevertheless, at geomagnetic prospecting, where the large areas with slow change of the soil magnetic susceptibility are studied, the measurement of anomalous magnetic field components is not so important because of absence of the pronounced structural configurations. Such a study can be provided by FGM in magnetic field absolute value measurement mode. The anomalous magnetic field value ΔB_i is calculated by simple equation

$$\Delta B_i = B_i - B_{i0}, \quad (2)$$

where B_1, B_i are the first and i-th magnetic field absolute value readings on the studied profile,

$$B_i = (B_{x,i}^2 + B_{y,i}^2 + B_{z,i}^2)^{0,5}.$$

For such a case, the FGM orientation does not affect on ΔB_i estimation. And to distinguish temporal and spatial variations of the magnetic field, a stationary reference magnetometer with known orientation has to be installed in the area where the survey is executed.

At fast magnetic field changes, for example at buried compact object or UXO detection and classification the 3-component anomalous magnetic field measurements are obligatory. Very often for decreasing of air-ground boundary influence the gradiometric measurements are applied. In this case two FGMs are mounted on a rigid platform at fixed distance (see, for example, Magdrone II [20]).

To find the necessary resolution threshold of FGM for this purpose, let us estimate the magnetic field value at differential (gradiometric) detection method of a small steel sphere with radius $R=1$ cm and magnetic permeability $\mu_s=300\mu_0$, where μ_0 is magnetic permeability of free space ($\mu_0=4\pi\times 10^{-7}$ H/m). Because the sphere is small in comparison with distance r to the sensor we can use the dipole approximation for its induced field \mathbf{B} in the Earth external magnetic field \mathbf{B}_0 :

$$\mathbf{B} = \mu_0 (3r(\mathbf{M} \cdot \mathbf{r}) / r^5 - \mathbf{M} / r^3) / 4\pi \quad (3)$$

The vector of magnetic moment \mathbf{M} for steel sphere equals to [23]:

$$\mathbf{M} = 4\pi R^3 (\mu_s - \mu_0) \mathbf{B}_0 / (\mu_0 (\mu_s + 2\mu_0)) \quad (4)$$

The results of arising anomalous magnetic fields calculation for movement of two FGMs placed on a boom with separation distance $\Delta x=1$ m over the steel sphere $R=1$ cm with centre coordinates $x_s=y_s=z_s=0$ at height $z=0.5$ m along x-direction ($y=0$) are shown in Figs. 1 - 2.

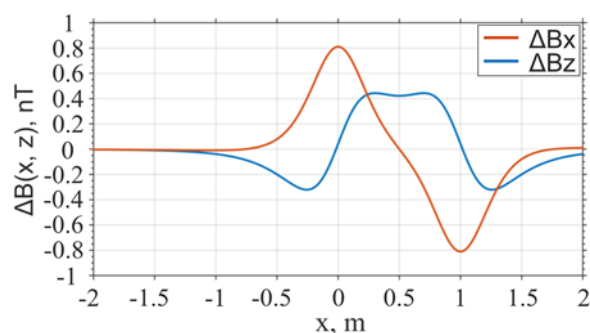


Fig. 1. Modeling results for a steel sphere with $R=1$ cm and $M_x=M_y=0$, $M_z \neq 0$ with centre coordinates $x_s=y_s=z_s=0$, flight at height $z=0.5$ m along x-direction and B_0 , $m=50,000$ nT.

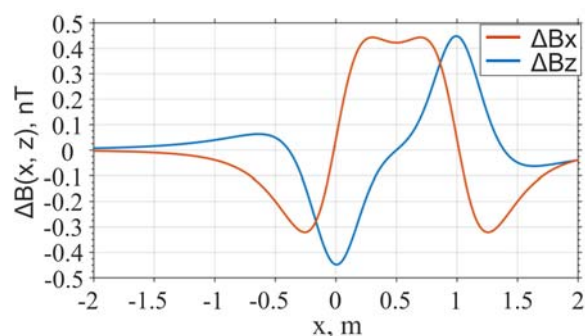


Fig. 2. Modeling results for a steel sphere with $R=1$ cm and $M_y=M_z=0$, $M_x \neq 0$ with centre coordinates $x_s=y_s=z_s=0$, flight at height $z=0.5$ m along x-direction and B_0 , $m=50,000$ nT.

Here for simplification of numerical estimations we assume that \mathbf{B}_0 has direction along only one Cartesian coordinate axis $m=x, y, z$ and its absolute value equals to $B_0=50,000$ nT. Thus anomalous magnetic field is calculated for two different magnetic moment orientations: $M_x=M_y=0$, $M_z \neq 0$; $M_y=M_z=0$, $M_x \neq 0$.

From these figures it is clearly seen that such a small object can be reliably detected if the FGM noise level is less than 0.15 nT. It should be noted that calculated anomalous fields is proportional to R^3 , thus for steel sphere of $R=2$ cm the field maximums are in the range 3-6.4 nT. The same field intensity can be achieved at $R=1$ cm and $z=0.25$ m because of field proportionality to $1/r^3$.

3. Description of FGM for Drones

As it was stated above, FGM is the most suitable for vectorial magnetic field measurements with drones. That is why FGM was taken as basic magnetometer to be adapted to moving carrier applications. The most important parameter characterizing magnetometer quality is magnetic noise, which arises due to fluctuations determined by periodic magnetization of the FGM sensor core. For decrease the noise level, the attention has to be paid primarily to the selection of the best material for the sensor core, its annealing and excitation modes. Also, the proper selection of sensor housing material has to be made. It is assumed that the quality of electronic components used during FGM manufacturing allows neglecting their influence at the final FGM parameters. Taking into account very limited energetic capability of the drone, it is necessary to decrease as much as possible the FGM power consumption with retention of low noise level, which regularly increases with lowering of consumed power. Finally, because of drone movement, the broadening of a frequency range should be done because FGM usually are designed for measurement of very slow fluctuations (\sim DC-1 Hz).

The detailed analysis of the ways to fulfil necessary requirements to low power FGMs was presented in [24]. The use of recommendations given there allowed development of the customized FGM LEMI-026 which has several advantages relatively to best found in the publications drone-oriented FGM MagDrone One [20]. The comparison of technical parameters of these two FGMs is given in Table 1.

From this table it is evident that the developed magnetometer has strong advantages as to most important parameters – sensitivity threshold and especially power consumption. Also from the published parameters one may conclude that MagDrone One is an FGM only, whereas LEMI-026 is a complete instrument which may be used fully autonomously suspended to drone.

Table 1. Comparison of LEMI-026 and MagDrone One Main Technical Parameters.

| Parameter | LEMI-026 | MagDrone One |
|--|--|--|
| Measured range of the magnetic field | ± 70000 nT | ± 75000 nT |
| Frequency range | DC...100 Hz | No data |
| Sample rate | 250 Hz | 200 Hz |
| Noise level at 1 Hz | 10 pT/ $\sqrt{\text{Hz}}$ | 20 pT/ $\sqrt{\text{Hz}}$ |
| ADC (6 channels) | 32 bits | 24 bits |
| Tilt measurement range | $\pm 30^\circ$ | No data |
| Tiltmeter resolution | 0.01 $^\circ$ | No data |
| Operating temperature range | -20... +60 $^\circ\text{C}$ | -20 to +50 $^\circ\text{C}$ |
| Power supply voltage | 5 \pm 0.25 V | 12 V |
| Maximal power consumption | < 1.2 W | 6 W |
| Recording time with 1900 mAh internal battery | 5 h | No data |
| GPS Receiver time stamps error maximal data rate | <100 ns 10 Hz | No data |
| Digital interface | USB | Serial to USB |
| Volume of SD memory card | 8 GB | No data |
| Internal memory | - | 512 M |
| Weight | <1.25 kg | 0.7 kg |
| Dimensions: | Electronic unit with sensor and battery \varnothing 96 \times 270 mm | Electronic unit 205 \times 105 \times 45 mm Sensor \varnothing 35 \times 365 mm |

The external view of LEMI-026 FGM for drones use is given in Fig. 3 – both with weather-proof housing and without.



Fig. 3. External view of LEMI-026 magnetometer both with weather-proof housing (left) and without it (right).

4. Experimental Tests Results

The field tests were performed using two of the LEMI-026 magnetometers. The first problem which had to be investigated was magnetometer noise level (NL) in flight. The Fig. 4 shows that LEMI-026 magnetometer assembled with digital part has NL in stationary position below 30 picotesla, what is fairly good according to the modeling results (Figs. 1 - 2).

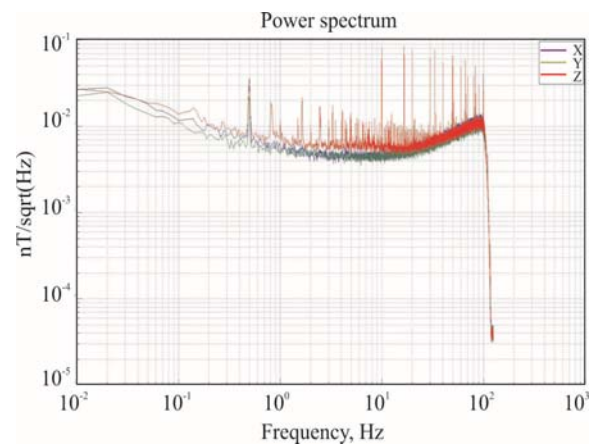


Fig. 4. Noise level of LEMI-026 magnetometer assembled with digital part in stationary position.

To estimate the FGM NL when mounted onboard the copter the data obtained at drone flight were submitted to spectral analysis (see Fig. 5). Here color plots are B_x , B_y , B_z components of the FGM and in black are given two components T_x , T_y of tiltmeter data. Necessary to mention that FGM spectra at Fig. 5 are not correct in the Earth frame system because axes azimuths are changing during the flight. More precisely, they have to be considered as FGM components in the frame system of the sensor. But we may accept them for further analysis because our goal here is to estimate what we may get from FGM on copter in movement.

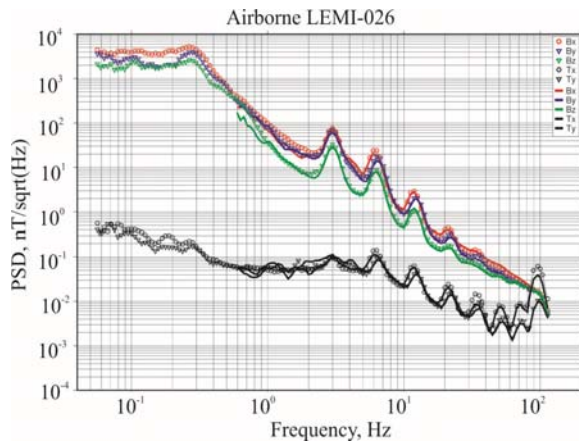


Fig. 5. Spectral analysis of LEMI-026 magnetometer noise level when mounted onboard drone at flight.

These data allow us to make following conclusions. First, strange set of oscillations with 3 Hz frequency and its harmonics are observed both in magnetometer and tiltmeter plots. We shall not comment them and only make an assumption that they are resulted by the mechanical oscillations of copter and FGM suspension system.

Next, the magnetic measurements in movement are used as it was mentioned above for aeromagnetic survey or buried objects detection. For the aeromagnetic survey variations in the period range more than 10 second are used. Analyzing data at the figure, we see that at the frequency 0.1 Hz signal fluctuations are around 2000 – 4000 nT, what is considerably more than any useful signal.

Nevertheless, let us try to analyze the obtained data in order to estimate whether it is possible to apply this method to aeromagnetic survey using the obtained during the flight data of components of vector of Earth's magnetic field and their spatial and temporal variations [25]. As it is seen from the Table 1, the sampling rate of FGM is 250 Hz, and GPS timing – 10 Hz. Because of this the first step was FGM data decimation to 10 Hz and then for every time moment the magnetic field module was calculated as:

$$F_f(t, x) = \sqrt{B_x(t, x)^2 + B_y(t, x)^2 + B_z(t, x)^2}, \quad (5)$$

where $F_f(t, x)$ is the vector of EMP induction for FGM in flight as function of time and space, $B_i(t, x)$ are the components of magnetic field induction vector.

For FGM in flight time and space variables are connected uniquely – to each moment of time responds its own position in space. At aeromagnetic survey, the spatial distribution of the EMP module under the studied area is searched; because of this the temporal variations have to be eliminated from the data. For this the data of a second – stationary FGM – were used, its decimation also was made and the file $F_b(t)$ was obtained. Then for every time moment the difference $F(x) = F_f(t, x) - F_b(t)$ was calculated as the

data depending exclusively on spatial position of the flying FGM.

This value is plotted in Fig. 6 and corresponding area map with flight traces is given in Fig. 7.

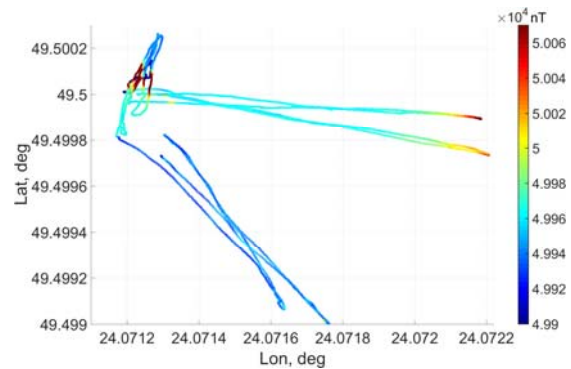


Fig. 6. Results of the magnetic field calculation as difference of the data of moving and stationary magnetometers.



Fig. 7. Test area map with flight traces corresponding to magnetic field data in Fig. 6.

From the comparison of both figures we may conclude that the tests were successful because namely at the places where enhanced intensity of the magnetic field was obtained the inspection revealed metallic bar (upper left part) and buried tube along the road (right part).

5. Conclusion

From the analysis above we may conclude that the parameters of the existing flux-gate magnetometers allow their using for magnetic survey with moving platforms. The electromagnetic interference from the drone motor and uncontrolled oscillations of drone and suspension are the main factors which limit the magnetometer sensitivity level. This problem can be solved by proper interference filtration and use of stabilized towed FGM construction. First results showed that FGM application for the search of metallic objects using scalar calculations seem to be satisfactory, but vector calculation results need further development. For this it is expected that matrix

method for FGM axes attitude reduction to geomagnetic frame can be successfully implemented for the electromagnetic sounding system, where the knowledge of sensor axes direction is important for data interpretation.

References

- [1]. A. B. Broughton Edge, T. H. Laby, *The Principles and Practice of Geophysical Prospecting*, Cambridge University Press, 2012.
- [2]. L. Dyson, C. Johnson, E. Heppell, M. Pieters, Archaeological evaluation of wetlands in the Planarch area of North West Europe, 2007. (<http://agris.fao.org/agris-search/search.do?recordID=AV20120155498>).
- [3]. N. Linford, Archaeogeophysics: Applications and challenges for magnetic methods, in *Proceedings of the Workshop on Soil Magnetism: Multidisciplinary Perspectives, Emerging Applications and New Frontiers: Report. ERDC Report*, 2009, pp. 35-36.
- [4]. S. D. Stull, From west to east: current approaches to medieval archaeology, *Cambridge Scholars Publishing*, 2015.
- [5]. Y. Das, Soil magnetism and landmine (metal) detectors, in *Proceedings of the Workshop on Soil Magnetism: Multidisciplinary Perspectives, Emerging Applications and New Frontiers: Report. ERDC Report*, 2009, pp. 15-20.
- [6]. L. R. Pasion, S. D. Billings, D. W. Oldenburg, Y. Li, N. Lhomme, Soil compensation techniques for the detection of buried metallic objects using electromagnetic sensors, in *Proceedings of the Workshop on Soil Magnetism: Multidisciplinary Perspectives, Emerging Applications and New Frontiers: Report. ERDC Report*, 2009, p. 64.
- [7]. E. Dobos, F. Carré, T. Hengl, H. I. Reuter, G. Tóth, Digital Soil Mapping as a support to production of functional maps, EUR 22123 EN, *Office for Official Publications of the European Communities*, Luxembourg, 2006.
- [8]. T. Mayr, Digital Soil Mapping – spatial variability and prediction of soil properties, in *Proceedings of the Workshop on Soil Magnetism: Multidisciplinary Perspectives, Emerging Applications and New Frontiers: Report. ERDC Report*, 2009, pp. 41-45.
- [9]. L. D. McGinnis, M. D. Thompson, S. F. Miller, Environmental Geophysics: Buildings E5485, E5487, and E5489 Decommissioning - The 'Ghost Town' Complex, Aberdeen Proving Ground, Maryland, *Reclamation Engineering and Geosciences Section, Energy Systems Division, Argonne National Laboratory, Argonne*, The report, 1994.
- [10]. J. W. E. Fassbinder, Geophysical Prospection: a Powerful Non-destructive Research Method for the Detection, Mapping and Preservation of Monuments and Sites, in *Proceedings of the 1st CEUR Workshop on The New Technologies for Aquileia*, Aquileia, Italy, May 2, 2011, pp. 1-9.
- [11]. R. A. Viscarra Rossel, V. Adamchuk, Proximal soil sensing, in *Precision Agriculture for Sustainability and Environmental Protection*, M. Oliver, T. Bishop, B. Marchant (Eds.), *Routledge*, NY, 2013, pp. 15-28.
- [12]. J. Hill, Civil engineering gives solar projects a firm foundation, *Solar Industry Magazine*, September 2015, pp. 1-11.
- [13]. S. R. Evanko, D. A. Dzombak, Remediation of Metals-Contaminated Soils and Groundwater, Report TE-97-01, *Ground-Water Remediation Technologies Analysis Center, Carnegie Mellon University*, Pittsburgh, PA, 1997.
- [14]. L. B. Ball, W. H. Kress, E. D. Anderson, A. P. Teeple, J. W. Ferguson, R. Charles, C. R. Colbert, Surface geophysical investigation of the areal and vertical extent of metallic waste at the former Tyson Valley Powder Farm near Eureka, *Scientific Investigations Report 2004-5208*, Missouri, Spring, 2004.
- [15]. J. L. Gerberding, H. Frumkin, Ellenville scrap iron and metal, Public health assessment prepared, *Agency for Toxic Substances and Disease Registry*, Report, Ellenville, Ulster county, New York, EPA facility ID: NYSFN0204190, 2006.
- [16]. K. F. Goddard, P. Wang, P. L. Lewin, S. G. Swingler, Detection and location of underground cables using magnetic field measurements, *Measurement Science and Technology*, Vol. 23, Issue 5, 2012.
- [17]. X. Sun, Y. Hou, P. W. T. Pong, Underground Power Cable Detection and Inspection Technology Based on Magnetic Field Sensing at Ground Surface Level, *IEEE Transactions on Magnetics*, Vol. 50, Issue 7, July 2014.
- [18]. Geotrace Pty Ltd (<http://www.geotrace.com.au>).
- [19]. Geometrics, OYO Corporation (<http://www.geometrics.com/geometrics-products/geometrics-magnetometers/>).
- [20]. SENSYS GmbH (<http://www.sensysmagnetometer.com/en/magdrone-one.html>).
- [21]. V. Korepanov, Yu. Tsvetkov, Gradient magnetometer system for balloons, in *Proceedings of the 17th ESA Symposium on European Rocket and Balloon Programmes and Related Research*, Sandefjord, Norway, Vol. 590, 30 May – 2 June 2005, (ESA SP-590, August 2005), p. 443-450.
- [22]. J. H. Scott, Electrical and magnetic properties of rock and soil, *Report 83-915*, Prepared in cooperation with the U.S. Air Force, 1983.
- [23]. R. Fitzpatrick, Classical Electromagnetism, *Create Space Independent Publishing Platform*, 2016.
- [24]. V. Korepanov, A. Marusenkov, Flux-Gate Magnetometers Design Peculiarities, *Surveys of Geophysics*, Vol. 33, Issue 5, 2012, pp. 1059-1079.
- [25]. V. Korepanov, F. Dudkin, Magnetometer design for copters, in *Proceedings of the 2nd International Conference on Sensors Engineering and Electronics Instrumental Advances (SEIA' 2016)*, 22-23 September 2016, Barcelona, Spain, pp. 138-139.



UWB Radar Signal Processing for Localization of Persons with the Changing Nature of Their Movement

¹ Dušan KOCUR, ² Daniel NOVÁK and ³ Mária ŠVECOVÁ

Technical University of Košice, Department of Electronics and Multimedia Communications
Letná 9, 042 00 Košice, Slovakia

¹ Tel.: +421 55 602 4233,

^{2,3} Tel.: +421 55 602 4234

E-mail: Dusan.Kocur@tuke.sk, Daniel.Novak@tuke.sk, Maria.Svecova@tuke.sk

Received: 5 November 2016 / Accepted: 5 December 2016 / Published: 30 December 2016

Abstract: In the last decade, it has been shown that short-range ultra-wide band radars (sensors) can provide the efficient solution for human being localization for line-of-sight and non-line-of-sight scenarios. To localize people correctly using this technology, the corresponding detection and localization methods have to be selected according to the nature of person motion state. In this respect, two basic kinds of persons can be identified. They are so-called moving and static persons. In this paper, we will introduce a radar signal processing procedure allowing a joint detection and localization of moving and static persons. Good performance properties of this procedure will be confirmed by its application for an experimental scenario represented by a through-the-wall detection and localization of a single person with changing nature of his/her movement.

Keywords: Detection, Localization, Moving and static person, Radar, Sensors, Signal processing, Target, Tracking, UWB.

1. Introduction

At the beginning of the 21st century, the human society is facing quite a number of specific social trends. The increasing density of population in towns and town agglomerations, criminality growing and political tensions producing terrorism can be ranked among them.

Taking into account these facts, the detection and positioning of human beings is very interesting especially for military and security operations. Here, reservoirs, power plants, and other critical infrastructures are extremely vulnerable to terrorist attack. Therefore, the request for monitoring of these critical environments and for the detection of unauthorized intrusion is still needful. At these events, the knowledge about the number of persons and their

position in the operational area can be very useful for military or security teams to take the right decisions [1]. In the outlined operations of law enforcement troops, the persons to be detected and localized are often situated behind an obstacle (e.g. behind a wall). That is the reason why conventional optical and infrared sensors cannot be applied for human beings localization for such scenarios.

As through-the-obstacles seeing sensors, the short-range high-resolution radars emitting electromagnetic waves with ultra-wide frequency band (UWB radars) using relatively low frequencies can be used with advantage [2]. Here, the ultra-wide frequency band provides the fine resolution of the radar systems. On the other hand, the electromagnetic waves emitted in the frequency band DC-5 GHz can penetrate through standard non-metallic materials with an acceptable

attenuation. Therefore, UWB radars exploiting this frequency band are capable to detect not only the targets located in a line-of-sight, but also the target situated behind a non-metallic obstacle.

There are two fundamental approaches for human beings localization. The former is intent on the localization of so-called moving persons, i.e. the persons moving within the monitored area in such a way that their co-ordinates are changing. In this case, the persons are detected based on an observation of the time changes of adjacent impulse responses within the radargram. These changes are identified along the propagation time (fast-time) axis [3]. The latter approach is devoted to the localization of so-called static persons, i.e. the persons situated but not moving (e.g. unconscious persons) within the monitored area (i.e. their co-ordinates are not changing). Respiration or heart beating could be given as examples of the motion activities of that kind. In this case, the persons can be localized based on the detection of their vital signs such as respiration or heart beating [4].

However, for real-life scenarios, persons to be located are usually moving through monitored area with some stops. Therefore, the same person may be once regarded as static and once again as a moving person. Moreover, the form of their movement is usually not known for monitoring system. Taking into account these facts, we will introduce in this paper a new UWB sensor signal processing procedure capable to localize a person for scenarios where persons change the nature of their motion. The presented approach based on a combination of radar signal

processing procedures developed for moving and static person localization in [3] and [4], respectively, has already been outlined in our previous work [16]. In contrast to [16], this contribution provides deeper analysis of the problem of locating persons moving by various forms of movement and a detailed description of the procedure for localization of persons moving with the changing nature of their movement as well.

This paper is organized as follows. In Section 2, a basic concept of localization of a person changing the nature of her/his motion will be firstly introduced. As we have outlined above, the core of the new localization approach consists in the application of the signal processing procedures for moving and static person localization. Therefore, these two signal processing procedures will be summarized in Section 3 and 4. In Section 5, some experimental results will be shown to illustrate the performance of the localization method introduced in Section 2. In the last section, some concluding remarks will be summarized.

2. Basic Concept of Person Localization

The analyses of the detection and localization of human beings by means of UWB sensors have shown that the fundamental solution of that problem depends on the character of the motion of persons to be detected and localized (e.g. [3-4], [16]). The results of the analyses are summarized in Table 1.

Table 1. Classification of person types according to the character of their motion.

| Person type | Description of person motion character | Example | Basic principle of person detection |
|---|---|--|---|
| Moving person I (MP-I) | Person moving within the monitored area in such a way that his/her co-ordinates are changing. | Walking, running, crawling persons | Detection of time changes of adjacent impulse responses of radargram. The changes should be identified along the propagation time (fast-time) axis. |
| Moving person II (MP-II) | Not motionless persons but their co-ordinates are not changing. | Person is still on the same place, but his/her limbs (legs, hands, head), trunk are in motion. | Detection of time changes of adjacent impulse responses of radargram. The changes should be identified along the propagation time (fast-time) axis. |
| Static person (SP) | “Motionless” persons situated in the monitored area. Their co-ordinates are not changing. | Sleeping person, unconscious person, etc. | Detection of person vital signs such as respiration or heart beating. |
| Person changing nature of his/her movement (MP+SP) | The same person may be once regarded as static and once again as a moving person. | Person walking with some stops. | Joint detection of time changes of impulse responses and person vital signs. |

This table suggests a classification of the person types according to the character of their motion and provides a description of the particular kinds of motions. Moreover, motion examples and basic person detection principles for the particular movement kinds are outlined in this table, too.

Taking into account these facts, MP-I and MP-II can be localized based on the detection of time changes of the adjacent impulse responses of radargram. These changes should be identified along the propagation time (fast-time) axis. For that purpose, radar signal processing procedure for moving person localization

(MPL) introduced in [3] can be applied. On the other hand, the detection of the person vital signs such as respiration or heart beating can be used for SP localization. Employing this idea, SP can be localized by radar signal processing procedure for static person localization (SPL) suggested in [4]. Then, a radar signal procedure for joint localization of the moving and static person can be proposed for MP+SP localization (M+SPL). This procedure consists of two steps. Firstly, raw radar data is processed in parallel by MPL and SPL. Then, a data fusion obtained as the results of the MPL a SPL is made to accomplish the procedure. For the data fusion, different approaches can be used. The simplest method (considered in this paper) consists only in a visualization of the results of MPL and SPL in the same figures.

As follows from the outlined concept of M+SPL, MPL and SPL are the key algorithms of this approach. Therefore, a short but comprehensive summary of these radar signal procedures is given in the next sections. It is assumed that the raw radar data for the both procedures are represented by a set of the impulse responses of the environment through which the electromagnetic waves emitted by the radar are propagated from transmitting to receiving radar antenna. This set of impulse responses is usually referred to as radargram. Moreover, we assume that UWB sensor considered here employs one transmitting and two receiving antennas.

3. Signal Processing Procedure for Moving Person Localization

MPL consists of the set of the five basic signal processing phases such as background subtraction, target detection, time of arrival (TOA) estimation (including TOA association), target localization, and target tracking. In the next, the importance of the particular phases and signal processing methods suitable for their implementation will be shortly outlined.

3.1. Background Subtraction

The analysis of the raw radar data shows that it is impossible to identify directly any persons within these signals. This comes from the fact that the components of the impulse responses represented by the target echo are much smaller in comparison with the signals reflected by the front wall or large/metal static objects or signals representing the cross-talk between transmitting and receiving antennas. In order to detect a moving target, the ratio of signals scattered by a target (i.e. nonstationary or periodic components of received signals) to noise and clutter (i.e., stationary components of received signals) has to be increased. For that purpose, background subtraction methods can be used (e.g. [5-6]). They help to reject, especially, stationary and correlated clutter, such as antenna

coupling, impedance mismatch response and ambient static clutter. In such a way we are able to detect a moving and static person echo within a radargram. It has been shown (e.g. in [5]) that the signal processing methods, such as basic averaging (mean, median), exponential averaging, adaptive exponential averaging, adaptive estimation of Gaussian background, Gaussian mixture method, moving target detection by FIR and IIR filtering, prediction, principal component analysis, etc., can be used for background subtraction. The mentioned methods differ in relation to assumptions concerning the clutter properties, as well as by their computational complexity and convenience for online signal processing. Because of a good performance, high robustness and low computational complexity, the method of exponential averaging [6] is one of the most popular and often used methods of background subtraction.

3.2. Target Detection

The detection is the next phase of the radar signal processing procedure, which comes after the background subtraction. In the case of MP-I and MP-II, the target echo can be considered as a nonstationary component of the impulse response. On the other hand, the clutter and noise are considered as stationary signal components. Hence, using a background subtraction method, target echo to clutter and noise ratio is increased. Then the target can be detected based by comparing the actual sample of the impulse response with a properly setting reference threshold. With regard to the fact, that the level of the background can vary, a very popular constant-false alarm (CFAR) detector is being used with advantage for the person detection [7-8]. The basic idea of CFAR detector operation consist in adaptive setting of its threshold in such a way as to maximize the probability of the target detection assuming the constant probability of false alarms. The output signal of the detector is represented by a binary signal, where "1" indicates that target has been detected, whereby "0" indicates that no target is detected in the monitored area.

In the field of target detection, a lot of different kinds and modifications of CFAR detectors can be found (e.g. [8]). Our experiences gained from testing of different CFAR detectors have shown, that a CFAR detector modification introduced in [7] can provide good and robust performance for MP-I and MP-II detection.

3.3. TOA Estimation

If a target is represented by only one non-zero sample at the detector output, then the target is referred to as a simple target. However, in the case of the scenario analyzed in this paper, the radar range

resolution is finer than the physical dimensions of the target (person). Then such a target is usually not expressed by only one non-zero sample of the detector output, but by a set of the non-zero samples. In this case, the target is referred to as the distributed target. Since several different TOA correspond to the same distributed target, the detector output for a distributed target is very complex, and the task for the distributed target localization is more complicated than that for a simple target. The basic idea of the distributed target localization employed in this paper consists of a substitution of the set of TOA corresponding to the same target with only one non-zero properly estimated TOA referred to as the TOA of the distributed target. Then, the TOA corresponding to a distributed target will be expressed by only one instant of the fast-time t_0 .

The very efficient algorithm for TOA estimation can be found e.g. in [9]. This algorithm referred to as the trace connection method provides not only TOA estimation, but also the association of the data received from two receiving channels and deghosting operation essential for multiple target detection. The trace connection method is quite complex, and hence, it is beyond this paper. The details concerning this method can be found e.g. in [9]. The output of this phase consists in the pairs of TOA associated with the same target obtained for the first (R_{x1}) and second (R_{x2}) receiving channel of the radar.

3.4. Target Localization

The aim of the target localization phase is to determine the target coordinates in a defined coordinate system. Because the considered UWB sensor is equipped with one transmitting and two receiving antennas, the target coordinates can be obtained using a direct computation method (e.g. [3], [5]) applied to the particular pairs of TOA associated with the same target. The estimates of the target coordinates represent the output of this phase.

3.5. Target Tracking

Target tracking provides a new estimate of the target location based on its foregoing positions. Target tracking usually results in the target trajectory estimation error decreasing, including trajectory smoothing. Most of tracking systems use a number of basic or advanced modifications of Kalman filters (e.g. [10]) or particle filters (e.g. [11]). In the case of multiple target tracking, multiple target tracking (MTT) systems can be used with advantage [12]. MTT efficiency is that it provides not only a simple target tracking, but also gate checking, point-to-point and point-to-track association and track maintenance.

4. Signal Processing Procedure for Static Person Localization

SPL consists of the set of the four basic signal processing phases such as background subtraction, target detection, TOA estimation (including TOA association), and target localization. Here, we would like to stress that the importance of background subtraction, target detection, TOA estimation, and target localization is the same as for MPL. Moreover, for the implementation of background subtraction, TOA estimation and target localization, the same methods as for MPL can be employed. Therefore, we will focus in this section on the detection phase only.

Detection methods analyze the radargram with the subtracted background to reach the decision whether a signal scattered by a static person is present or absent in the analyzed radargram. It is well known, that the respiratory motion of human beings can be considered as a periodical motion. Depending on the age, health and a mental condition of the person, the frequency of his/her respiration motion takes on value from the interval $B = \langle 0.2 \text{ Hz}, 0.7 \text{ Hz} \rangle$, whereby the pick-to-pick value of the chest motion due to respiration in adults is about 0.4-1.2 cm [17-18]. On the other hand, if we ignore the small changes between the person chest and antenna array of the radar system due to breathing, then the bistatic range of the person and radar system (i.e. the distance transmitting antenna-person-receiving antenna) can be considered as the constant one. Then, SP can be detected based on the identification (detection) of periodical components of the radargram with subtracted background located in the interval $B = \langle 0.2 \text{ Hz}, 0.7 \text{ Hz} \rangle$ for a constant instant of the propagation time $t = t_0$. Then, the target bistatic range is $d_0 = ct_0$, where $c = 3 \times 10^8 \text{ m s}^{-1}$ is the velocity of the electromagnetic wave propagation in the air.

It has been shown in [4] that for the SP detection using the idea outlined in the previous paragraph, a two-stage detector can be used. This detector consists of power spectrum estimator, CFAR detector (the first detection stage) and a simple threshold detector (the second detection stage). As a power spectrum estimator, Welch periodogram (e.g. [13]) can be used. In the next step, the estimated power spectrum is integrated over the frequency band $B = \langle 0.2 \text{ Hz}, 0.7 \text{ Hz} \rangle$ to estimate the total power located in this frequency band. The result of this integration represents the input of the first detection stage. As the first stage detector, an order-statistic CFAR detector (OS-CFAR detector, [8]) employing guarding intervals has been suggested in [4]. Taking into account the fact that a person is a distributed target [3], the output of OS-CFAR detector is integrated over the distance corresponding approximately to a human body size. The quantity created in such a way represents the input of the second detection stage. And finally, as the second detector, a simple detector using a constant threshold is employed.

The results obtained as the output of the detection phase are then processed by the methods of TOA estimation and target localization as it was outlined in the previous section.

5. Experimental Results

The performance of the outlined approach for localization of a person changing the nature of their movement will be illustrated by through-the-wall localization (a brick wall with the thickness of 35 cm) of a person moving with a stop. The scenario is outlined in Fig. 1. The person was walking from the position P3, through the position P2 to the position P1. Then, the person was sitting motionless for 50 s in the position P3. Finally, the person returned back to the position P1 through the position P2.

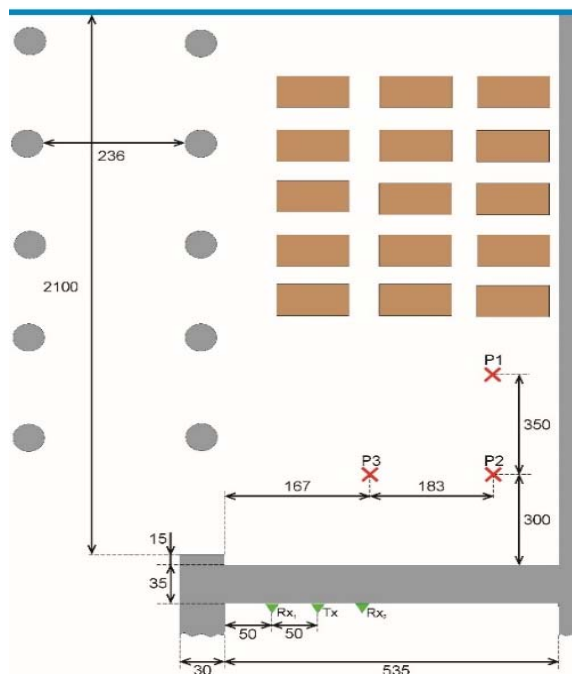


Fig. 1. Scheme of measurement.

The raw radar data analyzed in this contribution were acquired by means of M-sequence UWB radar system, equipped with one transmitting (Tx) and two receiving antennas (Rx_1 , Rx_2) [2]. The radar antenna positions are outlined in Fig. 1. The system clock frequency of the radar device is about 4.5 GHz, which results in the operational bandwidth of about DC-2.25 GHz. The order of the M-sequence emitted by the radar is nine, i.e., the impulse response covers 511 samples regularly spread over 114 ns. This corresponds to an observation window of 114 ns, leading to an unambiguous range of about 17 m. In our measurement, the radar systems were set in such a way as to provide approximately 13.5 impulse responses per second. The total power transmitted by the particular radars was about 1 mW.

For the target localization and its track estimation, M+SPL was used. The obtained results representing the outputs of its selected phases and the final estimation of the target track are given in Fig. 2-Fig. 10. Now, we can discuss the M+SPL performance.

In Fig. 2, the radargram with subtracted background for Rx_1 is given. The highest-level components of this figure usually (i.e. not always) represent the reflections due to person. This figure illustrates the different motion style of the person very clearly.

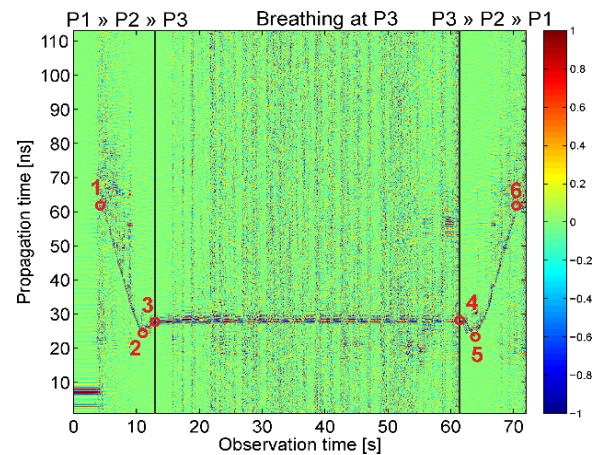


Fig. 2. Radargram with subtracted background. MPL, SPL, Rx_1 .

The part of the radargram between the points 1-2 corresponds to walking of MP-I from P1 to P2. Then, the part of the radargram between the points 2-3 with total length of a few second only expresses the person sitting down in a chair. Here, the person has still approximately the same co-ordinates, but their limbs are moving. Therefore, the person can be considered as MP-II for that part of the scenario. Then the person was sitting for the total time 50 s (section between the points 4-5). This is represented in the radargram by approximately constant value of t_0 propagation time corresponding to the highest level of the radargram components. It can be shown in a similar way that the section 6-7 corresponds person's getting up, and finally the section 7-8 describes the person walking from the position P3 towards the position P1 through P2.

The detector output for MPL and Rx_1 is sketched in Fig. 3. We can observe from this figure, that the detector is able to detect the target moving as MP-I and MP-II, but not as SP. The target track estimation for the person motion from the position P1 to P3 and for his motion from the position P3 to P1 are drawn in Fig. 4 and Fig. 5, respectively. The shape of the estimated tracks indicates a good performance of MPL for this parts of the analyzed scenario.

The performance of SPL is illustrated by Fig. 2 and Fig. 6 - Fig. 9. Firstly, the estimate of the radargram power spectrum is given in Fig. 6. Here, the relatively

high components of the power spectrum in the frequency band 0.5-0.6 Hz can be visible within the interval 25 ns-30 ns along the propagation time-axis. These components indicate that SP can be located in the monitored area. This hypothesis has been confirmed by the detection phase of SPL.

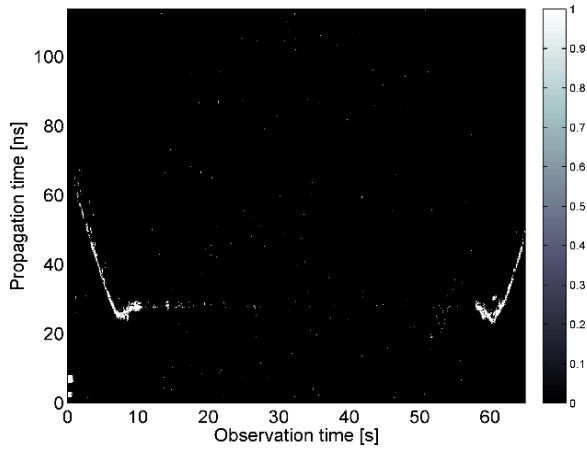


Fig. 3. Detector output. MPL. RX1.

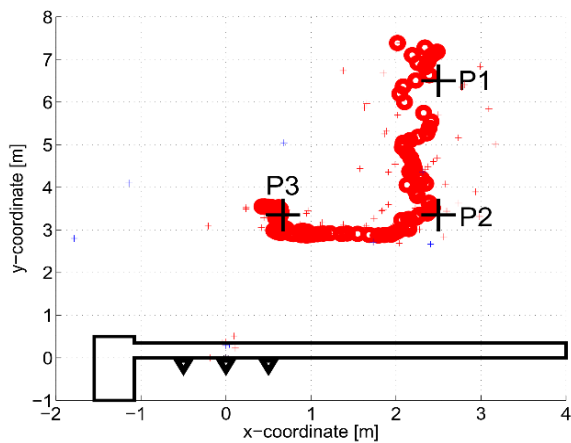


Fig. 4. Target track estimation for the person moving along the position P3-P2-P1. MPL.

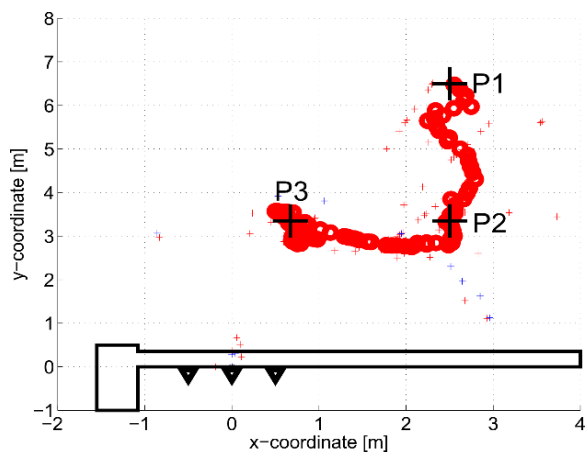


Fig. 5. Target track estimation for the person moving along the position P3-P2-P1. MPL.

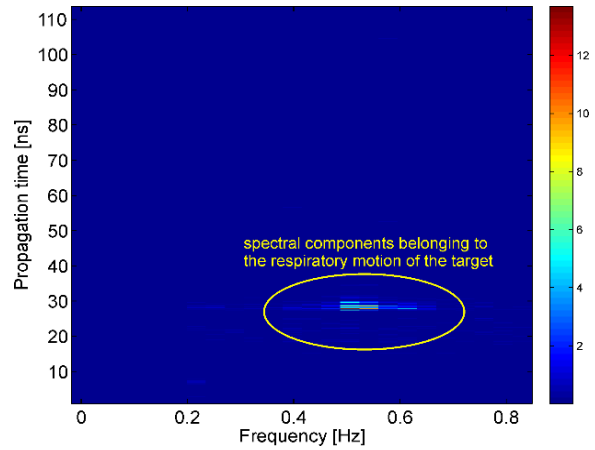


Fig. 6. Estimate of power spectrum of radargram with the subtracted background. SPL. RX1.

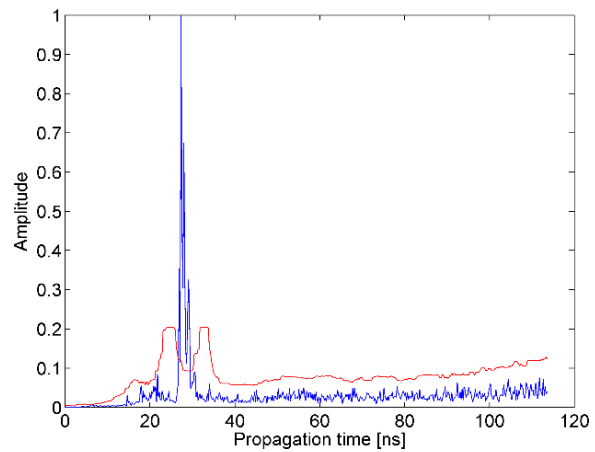


Fig. 7. OS-CFAR detector input (blue curve), OS-CFAR detector threshold (red curve). SPL. RX1.

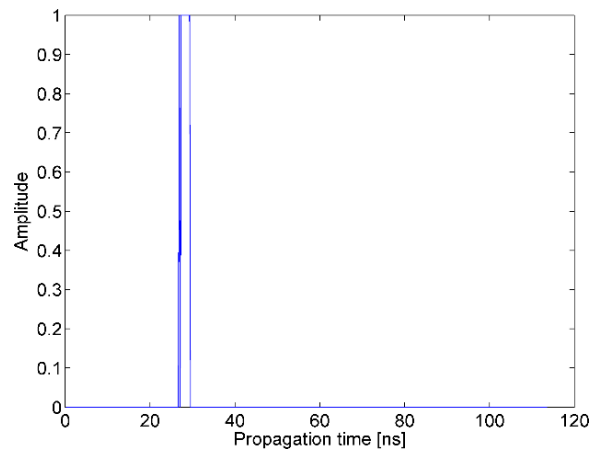


Fig. 8. The threshold detector output (the second detection stage). SPL. RX1.

Here, the person has been firstly detected by the OS-CFAR detector (Fig. 7). The decision of the OS-CFAR detector has been confirmed by the second detection stage (Fig. 8). Using the detector output,

target TOA has been estimated and the target coordinates has been computed (Fig. 9). The obtained results of SPL given in Fig. 9 indicate that SPL can provide a good performance for the analyzed scenario. Finally, the output of the MPL and SPL are fused in Fig. 10.

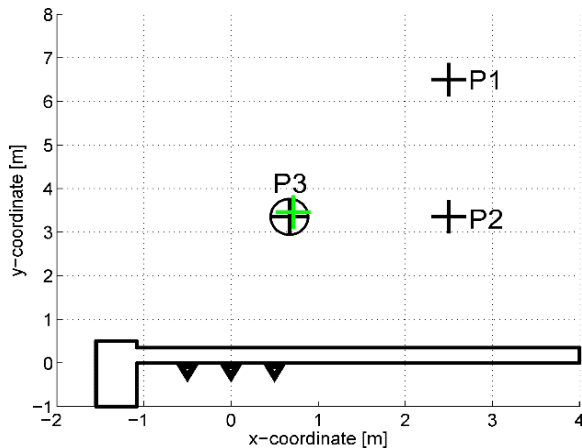


Fig. 9. Target localization by SPL. The true target position: P3, black mark. The estimated target position: green mark. Tolerance area: black circle.

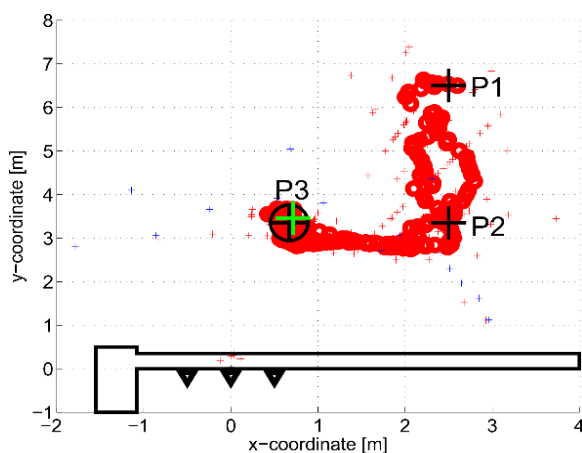


Fig. 10. Target localization as the fusion of the MPL and SPL outputs.

7. Conclusions

In this paper, we have dealt with the signal processing procedure for the short-range detection and localization of a person moving by a different style. The obtained results summarized in Fig. 10 indicate, that M+SPL could be a good candidate for the detection and localization of persons moving with the changing nature of their motion.

Unfortunately, in general, M+SPL is not able to provide a robust performance. In order to improve the performance of the proposed concept of M+SPL, this procedure should be extended at least by such signal processing phases as e.g. low-level echo of the target enhancement [14], wall effect compensation [15], etc.

The present version of M+SPL combines radar signal processing of two kinds: method based on the sequential processing of impulse responses (MPL) and the method of block signal processing (SPL) due to Welch periodogram computation. In our opinion, from the practical point of view, a new solution of SPL allowing radar signals to be processed by the method of sequential processing of the impulse responses instead of the block signal processing approach should be used. Finally, M+SPL should be extended also for multi-target scenarios. We assume that this approach could provide a new efficient approach for the person localization with changing nature of their motion.

Acknowledgements

This work was supported by the Slovak Research and Development Agency under the contract No. APVV-0404-12.

References

- [1]. Withington P., *et al.*, Enhancing Homeland Security with Advanced UWB sensors., *Microwave Magazine, IEEE*, Vol. 4, No. 3, 2003, pp. 51–58.
- [2]. Sachs J., *Handbook of Ultra-Wideband Short-Range Sensing, Wiley-VCH*, January 2013.
- [3]. Kocur D., Rovňáková J., Švecová M., Through Wall Tracking of Moving Targets by M-Sequence UWB Radar, in Rudas I. J., Fodor J., Kacprzyk J., (Eds.) *Towards Intelligent Engineering and Information Technology*, Rudas I. J., Fodor J., Kacprzyk J., (Eds.), *Springer*, 2009, pp. 349–363.
- [4]. Novák D., Kocur D., Multiple Static Person Localization based on Respiratory Motion Detection by UWB Radar, in *Proceedings of the IEEE 26th International Conference (RADIOELEKTRONIKA)*, 2016, pp. 252-257.
- [5]. Rovňáková J., Complete Signal Processing for Through Wall Tracking of Moving Targets, *LAP LAMBERT Academic Publishing*, Saarbrücken, Germany, 2010.
- [6]. Zetik R., *et al.*, Detection and Localization of Persons Behind Obstacles Using M-Sequence Through-The-Wall Radar, *Proc. SPIE, Sensors, and Command, Control, Communications, and Intelligence (C3I) Technologies for Homeland Security and Homeland Defense V*, Vol. 6201, 2006, pp. 62010I-1 - 62010I-12.
- [7]. Dutta P., Arora A., Bibyk S., Towards Radar-Enabled Sensor Networks, in *Proceedings of the 5th International Conference on Information Processing in Sensor Networks (IPSN)*, 2006, pp. 467–474.
- [8]. Rohling H., Some radar topics: waveform design, range CFAR and target recognition, in *Advances in Sensing with Security Applications*, Byrnes J., Ostheimer G., (Eds.), 2nd edition, *Springer Netherlands*, Vol. 2, 2006, p. 293-322.
- [9]. Rovňáková J., Kocur D., TOA estimation and data association for through-wall tracking of moving targets, *EURASIP Journal on Wireless Communications and Networking*, 2010, Vol. 2010, pp. 1-11.
- [10]. Grewal M. S., Andrews A. P., Kalman Filtering. Theory and Practice Using MATLAB, *John Wiley and Sons, Inc.*, Hoboken, New Jersey, 2008.

- [11]. Arulampalam M.S., Maskell S., Gordon N., Clapp T., A tutorial on particle filters for online nonlinear/non-Gaussian Bayesian tracking, *IEEE Transactions on Signal Processing*, Vol. 50, Issue 2, 2002, pp. 174–188.
- [12]. Rovňáková J., Kocur D., Short range tracking of moving persons by UWB sensor network, in *Proceedings of the 8th European Radar Conference (EuRAD)*, Manchester, UK, 2011, pp. 321–324.
- [13]. Proakis J. G., Manolakis D. G., *Digital Signal Processing*, Pearson Prentice Hall, 2007.
- [14]. Rovňáková J., Kocur D., Weak signal enhancement in radar signal processing, in *Proceedings of the 20th International Conference RADIOELEKTRONIKA*, Brno, Czech Republic, 19-21 April 2010, pp. 1-4.
- [15]. Rovňáková J., Kocur D., Compensation of wall effect for through wall tracking of moving targets, *Radioengineering, Part 2, Special Issue on Workshop of the COST Action IC0803: RF/Microwave Communication Subsystems for Emerging Wireless Technologies (RFCSET)*, Vol. 18, No. 2, 2009, p. 189-195.
- [16]. Kocur D., Novák D., UWB Sensor Based Localization of Person with the Changing Nature of His/Her Movement, in *Proceedings of the 2nd International Conference on Sensors Engineering and Electronics Instrumental Advances (SEIA'2016)*, 22-23 September 2016, Barcelona, Castelldefels, Spain, 2016.
- [17]. Sachs J., *et al.*, Remote vital sign detection for rescue, security, and medical care by ultra-wideband pseudo-noise radar, *Ad Hoc Networks*, Vol. 13, 2014, pp. 42–53.
- [18]. Lazaro A., Girbau D., Villarino R., Techniques for clutter suppression in the presence of body movements during the detection of respiratory activity through UWB radars, *Sensors*, Vol. 14, No. 2, 2014, pp. 2595–2618.



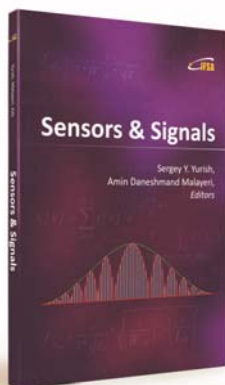
Published by International Frequency Sensor Association (IFSA) Publishing, S. L., 2016 (<http://www.sensorsportal.com>).



International Frequency Sensor Association (IFSA) Publishing

Sensors & Signals

Sergey Y. Yurish, Amin Daneshmand Malayeri, *Editors*



Formats: printable pdf (Acrobat) and print (hardcover), 208 pages

ISBN: 978-84-608-2320-9,
e-ISBN: 978-84-608-2319-3

Sensors & Signals is the first book from the Book Series of the same name published by IFSA Publishing. The book contains eight chapters written by authors from universities and research centers from 12 countries: Cuba, Czech Republic, Egypt, Malaysia, Morocco, Portugal, Serbia, South Korea, Spain and Turkey. The coverage includes most recent developments in:

- Virtual instrumentation for analysis of ultrasonic signals;
- Humidity sensors (materials and sensor preparation and characteristics);
- Fault tolerance and fault management issues in Wireless Sensor Networks;
- Localization of target nodes in a 3-D Wireless Sensor Network;
- Opto-elastography imaging technique for tumor localization and characterization;
- Nuclear and geophysical sensors for landmines detection;
- Optimal color space for human skin detection at image recognition;
- Design of narrowband substrate integrated waveguide bandpass filters.

Each chapter of the book includes a state-of-the-art review in appropriate topic and well selected appropriate references at the end.

With its distinguished editors and international team of contributors *Sensors & Signals* is suitable for academic and industrial research scientists, engineers as well as PhD students working in the area of sensors and its application.

http://www.sensorsportal.com/HTML/BOOKSTORE/Sensors_and_Signals.htm

An Optical Processor for Data Error Detection and Correction Using a (9,5) Binary Code Generator and the Syndrome Decoding Process

^{1,2} M. A. Vieira, ^{1,2,3} M. Vieira, ^{1,2} P. Louro, ^{1,2} V. Silva and ^{1,2} J. Costa

¹ Electronics Telecommunication and Computer Dept. ISEL, R. Conselheiro Emídio Navarro, 1959-007 Lisboa, Portugal

² CTS-UNINOVA, Quinta da Torre, Monte da Caparica, 2829-516, Caparica, Portugal

³ DEE-FCT-UNL, Quinta da Torre, Monte da Caparica, 2829-516, Caparica, Portugal

¹ Tel.: +351218317000, fax: +351218317144

E-mail: mv@isel.ipl.pt

Received: 5 November 2016 /Accepted: 5 December 2016 /Published: 30 December 2016

Abstract: Based on a-SiC:H technology, we present an optical processor for data error detection and correction using a suitable (9,5) Hamming binary code generator and the syndrome decoding process. The optical processor consists of an a-SiC:H double p-i-n photodetector with two ultraviolet light biased gates. The relationship between the optical inputs (transmitted data) and the corresponding output levels (the received data) is established and decoded. Results show that under irradiation the device acts as an active filter. Under front irradiation the magnitude of the short wavelength is quenched and in the long wavelength range is enlarged, while the opposite happens under back lighting. Parity bits are generated and stored simultaneously with the data word. Parity logic operations are performed and checked for errors together. An all-optical processor for error detection and correction is presented to provide an experimental demonstration of this fault tolerant reversible system. Two original coloured string messages, having 4- and 5- bits, respectively, are analyzed and the transmitted 7- or 9- bit string, the parity matrix, the encoding and decoding processes, are explained. The design of SiC syndrome generators for error correction is tested.

Keywords: a-SiC:H technology, Error detection and correction, Syndrome decoding process, Hamming binary code.

1. Introduction

In digital transmission systems, an error occurs when a bit gets altered between transmission and reception; that is, a binary 1 is transmitted and a binary 0 is received, or a binary 0 is transmitted and a binary 1 is received. Noise and physical defects in the communication system can cause random bit errors during data transmission. Errors detection codes are generated as a function of the bits being transmitted.

Such codes are appended to the data bits and transmitted together. The receiver evaluates the code based on the incoming bits and compares it with the incoming code to check for errors [1]. Optical/optoelectronic computing is an important topic and several architectures, logical and arithmetic operations were proposed in the literature [2-3]. Remote control applications demand error correction also to be implemented, so that the receiver itself is able to manage error correction [4]. Error coding is a

method of detecting and correcting these errors which ensures information to be transferred intact from its source to its destination. Error coding uses mathematical formulas to encode data bits at the source into longer bit words for transmission. The code word can then be decoded at the destination to retrieve the information. The extra bits, in the code word, provide *redundancy* that, according to the coding scheme used, will allow the destination to use the decoding process to determine if the communication system has introduced errors and, in some cases, correct them avoiding the need of data retransmission.

By using different optoelectronic devices [5-6], strength has been set into the development of all-optical logical functions [7]. Tandem monolithic Si/C structures based on amorphous silicon technology can be reconfigurable to perform optoelectronic logic functions [8-9] due to their nonlinear magnitude-dependent response to each incident light wave, in the visible range. Based on such properties, in this paper we built an optical processor for error detection and correction based on SiC amorphous technology. The design of SiC syndrome generator is presented. The syndrome decoding is analyzed and uses the syndrome bits introduced. A syndrome decoding for a linear code is explained and tested showing the ability to decode a seven and nine linear code efficiently.

2. Experimental Details

2.1. Receiver Design and Operation

In Fig. 1, it is shown the configuration and operation of the optical receiver. The active device is a double pi^3n/pin a-SiC:H photodetector produced by Plasma Enhanced Chemical Vapor Deposition (PECVD). It consists of a $p-i'(a-SiC:H)-n/p-i(a-Si:H)-n$ heterostructure with high resistivity 20 nm thick doped layers ($>10^{17}\Omega \times cm$) packed between two transparent oxide layers (TCO) made of ITO. The deposition conditions and optoelectronic characterization of the single layers and device as well as their optimization were described elsewhere [10-11]. The device acts as an active filter, confining the short wavelength optical carriers in the front photodiode while the long ones are absorbed into the back photodiode (see arrow magnitudes). The medium wavelength ranges are absorbed differently across both [12].

In Fig. 1, a four channel transmission is exemplified. Here, the data is transmitted using four monochromatic (red, green, blue and violet; $\lambda_{R,G,B,V}$) pulsed communication channels (input channels; data code) that are mixed together, each one with a specific bit sequence and are absorbed in different regions depending on their wavelengths. The combined optical signal (multiplexed signal) is received and analysed by reading out the generated photocurrent under negative applied voltage (-8 V), and 390 nm

background lighting, applied either from the front or the back sides of the device. In a four channel data transmission, the square wave of four modulated low power lights of red (R: 626 nm), green (G: 524 nm), blue (B: 470 nm) and violet (V: 400 nm) LEDs were used. In the five channel transmission an extra near infrared (I: 700 nm) LED was added.

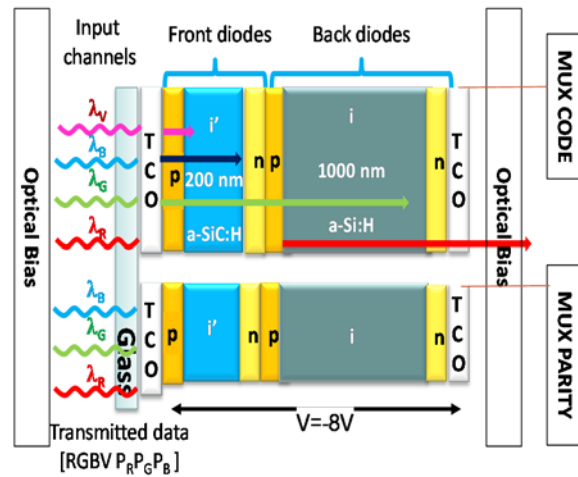


Fig. 1. Receiver configuration and operation.

Hamming codes are code words formed by adding redundant check bits, or parity bits, to a data word [1]. Those code words are verified at the receiver end to check and correct. So, when the transmission uses n input channels ($n=4$ or $n=5$), $n-1$ parity channels are needed to define the parity bits. Here, for parity check, three or four red, green, blue and violet synchronous channels, respectively, were read in simultaneous with the data code. As an application, data was sent through one detector while error detection and correction bits were sent through the other.

2.2. Nonlinear Optical Gain

Five monochromatic input channels in the VIS/NIR range (400 nm-850 nm) illuminated the device separately (transmitted data) or combined (MUX signal) at 12000 bps. The generated photocurrent was measured under negative applied voltage (-8 V) and under front and back steady state irradiation. For each channel, the gain ($\alpha_{R,G,B,V}^V$), defined as the ratio between the photocurrent with and without applied background, was determined.

In Table 1 the optical gains of the input channels used in the transmission are displayed under $2800 \mu Wcm^{-2}$ front (α_F) and back (α_B) irradiation.

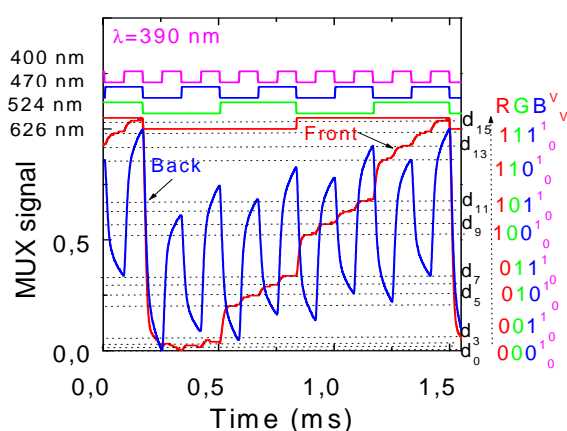
Data measured confirm that the optical gain, under irradiation, depends on the irradiated side and on the incoming wavelength acting as an active filter for the input channels.

Table 1. Front (α_F) and back (α_B) optical gains.

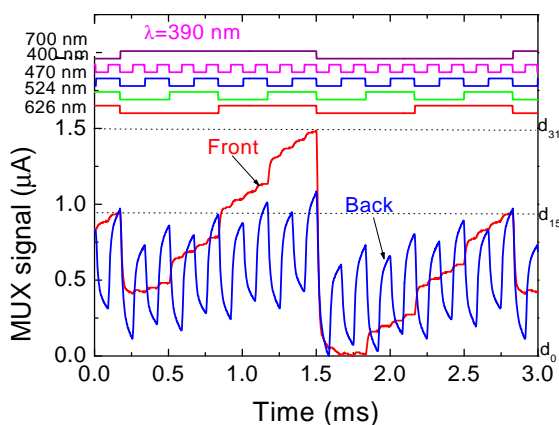
| λ (nm) | α_F | α_B |
|----------------|------------|------------|
| 400 | 0.90 | 11.60 |
| 470 | 1.07 | 1.96 |
| 524 | 3.55 | 0.57 |
| 626 | 4.70 | 0.45 |
| 700 | 5.55 | 0.40 |

3. MUX/DEMUX Receiver

In Fig. 2, the received data, i.e. the MUX code signal, due to the combination of four (Fig. 2(a); 400 nm, 470 nm, 524 nm, 626 nm) or five (Fig. 2(b); 400 nm, 470 nm, 524 nm, 626 nm, 700 nm) input channels are displayed under both front and back irradiations.



(a)



(b)

Fig. 2. MUX signals under 390 nm front and back irradiation. On the top the transmitted channels are displayed: a) Four channels transmission; b) Five channels transmission.

At the top, the input channels (transmitted data) are shown to guide the eyes. In Fig. 2(a), the selection index for the 16-element look-up (d_0 - d_{15} , dotted levels) is a 4-bit binary code (RGBV), while in Fig.

2(b), the selection index for the 32-element look-up (d_0 - d_{31} , dotted levels) is a 5-bit (RGBVI) binary code.

The algorithms to encode and decode are relatively simple and the knowledge of the background acting as selector that chooses one or more of the 2^n sublevels, with n the number of transmitted channels, and their n -bit binary code makes the communication reliable [13]. Results show that to each of the 2^n possible *on/off* states corresponds a well-defined level. In Fig. 2, all the *on/off* states are possible so, 2^n ordered levels are detected and correspond to all the possible combinations of the *on/off* states [14]. Here, under either front or back irradiation, each of those n channels, by turn, are enhanced or quenched differently (see Table 1) resulting in an increase magnitude of infrared/red/green under front irradiation or of the blue/violet, under back lighting. So, by assigning each output level to an n digit binary code weighted by the optical gain of the each channel, the signal can be decoded. A maximum transmission rate capability of 60 kbps was achieved in a five channel transmission.

4. Error Control Based on a-SiC:H Technology

The proximity of the magnitude of consecutive levels (Fig. 2) and noise during the read out process causes occasional errors in the decoded information that should be corrected. To minimise the errors, a parity bit [1] was generated and stored along with the data word. The parity of the word is checked after reading the word. The word is accepted if the parity of the bits read out is correct. If the parity of the bits is incorrect, an error is detected, but it cannot be corrected. An error-correcting code uses multiple parity check bits that are stored with the data word. Each check bit is a parity bit for a group of bits in the data word. When the word is read, the parity of each group, including the check bit, is evaluated. If the parity is correct for all groups, it indicates that no detectable error has occurred. If one or more of the newly generated parity values is incorrect, a unique pattern called a syndrome results that may be able to identify which bit is in error. If the specific bit in error is identified, then the error can be corrected by complementing the erroneous bit.

The standard Hamming code [1] is designed to have a minimum Hamming distance of 3 between any two code words. i.e., the Hamming (7,4) is a standard type of Hamming code that encodes 4 bits (four input channels) of data into 7 bits by adding 3 parity bits (three parity input channels). Taking into account Fig. 2(a), the encoder takes four input data bits [R G B V] to which corresponds one of the possible 16 sublevels and generates three additional parity bits to which corresponds one of the eight (2^3) possible well defined levels:

$$P_R-(VRB) = V \oplus R \oplus B \quad (1)$$

$$P_G-(VRG) = V \oplus R \oplus G \quad (2)$$

$$P_B-(VGB) = V \oplus G \oplus B \quad (3)$$

In a similar way, from Fig. 2(b), the encoder for code takes five input data bits [R G B V I] to which corresponds one of the possible 32 sublevels, and also provides violet redundancy creating the same three additional parity bits, given by the Equations (1), (2) and (3) and an extra fourth parity bit given by Equation (4).

$$P_V-(I) = I \quad (4)$$

The extra bit for the extended code is added as one more parity check bit. This fourth parity equation was chosen to take advantage of the background illumination. Since under front irradiation the 626 nm and 700 nm have similar optical gains in order to decode the near-infrared channel the parity bit matches with the violet bit where the back optical gain is high (Table 1). So, in a four channel transmission (Equations (1), (2), (3)) the parity bits are SUM bits of the three-bit additions of violet pulsed signal with two additional bits of RGB [15]. In a five channel transmission (Equations (1), (2), (3) and (4)), one-bit extra, named I, was added leading to a 16-level $P_R P_G P_B P_V$ MUX for the parities.

To build a code with 5-bit data words [R G B V I] that will correct single-bit errors, we must add the 4 check bits [P_R, P_G, P_B, P_V] generated by Equations (1), (2), (3) and (4) creating extended code words of length 9. In Table 2, all the 32 code word combinations are displayed. For a 4-bit transmission the process was similar and made using the standard Hamming code [14].

Fig. 3, show the MUX signal (solid lines) that arises from to the transmission of the four (Fig. 3(a)) or five (Fig. 3(b)) wavelength channels. The dotted line marks the generation of the synchronized parity MUX transmitted in simultaneous with the data code. Due to the different front and back optical gains (Table 1) the colors red, green, blue and violet were assigned respectively to P_R, P_G, P_B and P_V . The eight, or the sixteen, ordered levels of the parity bits are marked as horizontal dash lines in Fig. 3(a) and Fig. 3(b), respectively. In the right side of figures the eight or the sixteen sublevels and their 3- or 4-bit binary codes are inserted, respectively. On the top the seven or the nine bit word [R, G, B, V (I), $P_R, P_G, P_B (P_V)$] of the transmitted inputs guides the eyes.

Taking into account Fig. 3(a) and Fig. 3(b) the 7- or the 9-bit word at the output of the encoder will be in a bitwise format, with the data and the parity bits separated. It is interesting to notice that different code words can present the same parity bits. For instance, in Fig. 3(a) the levels d_2 and d_{12} present the same parity level p_5 while in Fig. 3(b) the same occur between d_{18} and d_{28} that both present parity level p_{11} .

Table 2. Strings of all possible code words for a (9,5) block code. The message and parity digits [R G B V I : $P_R P_G P_B P_V$] and the received message levels, d_{0-31} , and their correspondent parity levels, p_{0-15} .

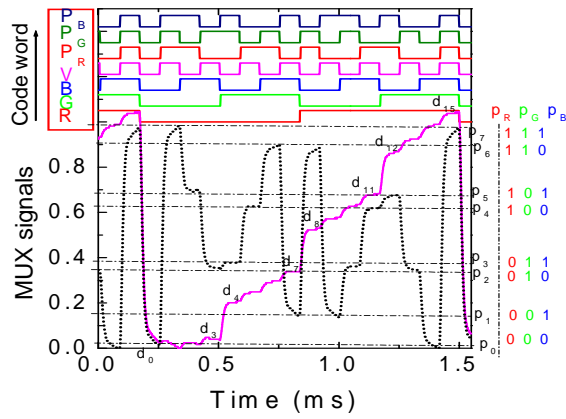
| d_{0-31} | R | G | B | V | I | P_R | P_G | P_B | P_V | p_{0-15} |
|------------|---|---|---|---|---|-------|-------|-------|-------|------------|
| d_0 | 0 | 0 | 0 | 0 | 0 | 0 | 0 | 0 | 0 | p_0 |
| d_1 | 0 | 0 | 0 | 1 | 0 | 1 | 1 | 1 | 0 | p_{14} |
| d_2 | 0 | 0 | 1 | 0 | 0 | 1 | 0 | 1 | 0 | p_{10} |
| d_3 | 0 | 0 | 1 | 1 | 0 | 0 | 1 | 0 | 0 | p_4 |
| d_4 | 0 | 1 | 0 | 0 | 0 | 0 | 1 | 1 | 0 | p_6 |
| d_5 | 0 | 1 | 0 | 1 | 0 | 1 | 0 | 0 | 0 | p_8 |
| d_6 | 0 | 1 | 1 | 0 | 0 | 1 | 1 | 0 | 0 | p_{12} |
| d_7 | 0 | 1 | 1 | 1 | 0 | 0 | 0 | 1 | 0 | p_2 |
| d_8 | 1 | 0 | 0 | 0 | 0 | 1 | 1 | 0 | 0 | p_{12} |
| d_9 | 1 | 0 | 0 | 1 | 0 | 0 | 0 | 1 | 0 | p_2 |
| d_{10} | 1 | 0 | 1 | 0 | 0 | 0 | 1 | 1 | 0 | p_6 |
| d_{11} | 1 | 0 | 1 | 1 | 0 | 1 | 0 | 0 | 0 | p_8 |
| d_{12} | 1 | 1 | 0 | 0 | 0 | 1 | 0 | 1 | 0 | p_{10} |
| d_{13} | 1 | 1 | 0 | 1 | 0 | 0 | 1 | 0 | 0 | p_4 |
| d_{14} | 1 | 1 | 1 | 0 | 0 | 0 | 0 | 0 | 0 | p_0 |
| d_{15} | 1 | 1 | 1 | 1 | 0 | 1 | 1 | 1 | 0 | p_{14} |
| d_{16} | 0 | 0 | 0 | 0 | 1 | 0 | 0 | 0 | 1 | p_1 |
| d_{17} | 0 | 0 | 0 | 1 | 1 | 1 | 1 | 1 | 1 | p_{15} |
| d_{18} | 0 | 0 | 1 | 0 | 1 | 1 | 0 | 1 | 1 | p_{11} |
| d_{19} | 0 | 0 | 1 | 1 | 1 | 0 | 1 | 0 | 1 | p_5 |
| d_{20} | 0 | 1 | 0 | 0 | 1 | 0 | 1 | 1 | 1 | p_7 |
| d_{21} | 0 | 1 | 0 | 1 | 1 | 1 | 0 | 0 | 1 | p_9 |
| d_{22} | 0 | 1 | 1 | 0 | 1 | 1 | 1 | 0 | 1 | p_{13} |
| d_{23} | 0 | 1 | 1 | 1 | 1 | 0 | 0 | 1 | 1 | p_3 |
| d_{24} | 1 | 0 | 0 | 0 | 1 | 1 | 1 | 0 | 1 | p_{13} |
| d_{25} | 1 | 0 | 0 | 1 | 1 | 0 | 0 | 1 | 1 | p_3 |
| d_{26} | 1 | 0 | 1 | 0 | 1 | 0 | 1 | 1 | 1 | p_7 |
| d_{27} | 1 | 0 | 1 | 1 | 1 | 1 | 0 | 0 | 1 | p_9 |
| d_{28} | 1 | 1 | 0 | 0 | 1 | 1 | 0 | 1 | 1 | p_{11} |
| d_{29} | 1 | 1 | 0 | 1 | 1 | 0 | 1 | 0 | 1 | p_5 |
| d_{30} | 1 | 1 | 1 | 0 | 1 | 0 | 0 | 0 | 1 | p_1 |
| d_{31} | 1 | 1 | 1 | 1 | 0 | 1 | 1 | 1 | 1 | p_{15} |

As an example, in Fig. 3(a) the codeword that corresponds to receive the $d_3 = "0011"$ and $p_2 = "010"$ levels are in the same time slot. Since d_3 is too near d_2 the message ($d_2:p_2$) could be measured instead, which is impossible since the d_2 correspondent parity level, $p_5 = "101"$, is too far way. A similar example could be easily obtained from Fig. 3(b). Here, the codeword [10111001] was sent and received as ($d_{26}; p_9$) which corresponds to [101011001], which is impossible since the last four bit should be $p_9 = "1001"$ ($d_{27}; p_9$). So, an error was detected in the transmission and has to be corrected.

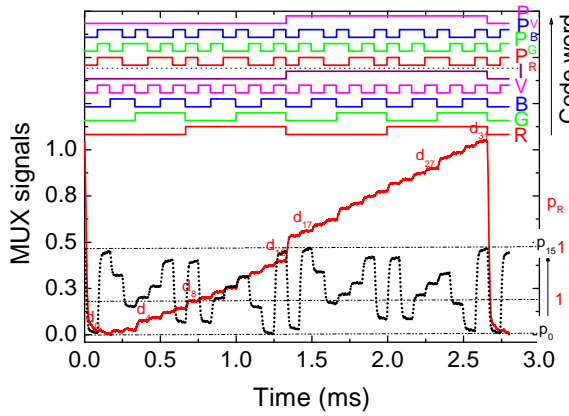
5. Design of SiC Syndrome Generators and Syndrome Decoding

5.1. Syndrome Calculation for a Hamming (9,5) Block Code

The transformation from message bits to code words is linear, so, one can represent each message-to-codeword transformation succinctly using matrix notation.



(a)



(b)

Fig. 3. Code and parity MUX signals under 390 nm front irradiation. On the top the transmitted channels [R G B V P_R P_G P_B] are shown. a) Four channel transmission; b) five channel transmission.

The parity check bits of a (7, 4) block code are generated by Equations (1), (2), (3) and for a (9,5) block code by Equations (1), (2), (3), (4) (see Table 2). To obtain the generator matrix and the parity check matrix, the check bits are related in a five channel transmission as [3]:

$$\begin{bmatrix} P_R-(VRB) & P_G-(VRG) & P_B-(VGB) & P_V-(I) \end{bmatrix}_{\times 4} = \begin{bmatrix} RGBVI \end{bmatrix}_{\times 5} \begin{bmatrix} P \end{bmatrix}_{5 \times 4}, \quad (5)$$

where P is the parity matrix.

Comparing the above equations with the check bit equations (Equations (1), (2), (3), (4)) we find that P matrix, for a five channel transmission, is given as:

$$P = \begin{bmatrix} 1 & 1 & 0 & 0 \\ 0 & 1 & 1 & 0 \\ 1 & 0 & 1 & 0 \\ 1 & 1 & 1 & 0 \\ 0 & 0 & 0 & 1 \end{bmatrix} \quad (6)$$

The Generator matrix, G , is taken so that $G_{k \times n} = [I_k : P_{k \times (n-k)}]$, where I_k is the identity matrix which determine the code words and P , the parity matrix, that provides redundancy, and G is given by:

$$G_{5 \times 9} = [I_5 : P_{5 \times 4}] = \begin{bmatrix} 1 & 0 & 0 & 0 & 0 & : & 1 & 1 & 0 & 0 \\ 0 & 1 & 0 & 0 & 0 & : & 0 & 1 & 1 & 0 \\ 0 & 0 & 1 & 0 & 0 & : & 1 & 0 & 1 & 0 \\ 0 & 0 & 0 & 1 & 0 & : & 1 & 1 & 1 & 0 \\ 0 & 0 & 0 & 0 & 1 & : & 0 & 0 & 0 & 1 \end{bmatrix}_{9 \times 5} \quad (7)$$

The parity check matrix, H is given by:

$$H = [P^T : I_{(n-k)}] = \begin{bmatrix} 1 & 0 & 1 & 1 & 0 & : & 1 & 0 & 0 & 0 \\ 1 & 1 & 0 & 1 & 0 & : & 0 & 1 & 0 & 0 \\ 0 & 1 & 1 & 1 & 0 & : & 0 & 0 & 1 & 0 \\ 0 & 0 & 0 & 0 & 1 & : & 0 & 0 & 0 & 1 \end{bmatrix} \quad (8)$$

And the syndrome is given by:

$$S_i = \begin{bmatrix} r & g & b & v & i & p_R & p_G & p_B & p_V \end{bmatrix} H^T \quad (9)$$

So, the output of the syndrome for general received word is a four-bit $S_i = [S_1 S_2 S_3 S_4]$, modulus 2, with:

$$\begin{aligned} S_1 &= (r + b + v + p_R), \\ S_2 &= (r + g + v + p_G), \\ S_3 &= (g + b + v + p_B), \\ S_4 &= (i + p_V), \end{aligned} \quad (10)$$

where each $[S_1 S_1 S_3 S_4]$ is the syndrome bit, and it helps the receiver to diagnose the errors in the received data. In a similar way, in a four channel transmission, the syndrome calculation for a (7,4) block code will give S_4 always zero once the parity check matrix will be given by:

$$H = \begin{bmatrix} 1 & 0 & 1 & 1 & : & 1 & 0 & 0 \\ 1 & 1 & 0 & 1 & : & 0 & 1 & 0 \\ 0 & 1 & 1 & 1 & : & 0 & 0 & 1 \end{bmatrix} \quad (11)$$

5.2. Syndrome Decoding

For a received word, syndrome decoding pre-computes the syndrome corresponding to each error. If it is 0, then there are no single-bit errors, and the receiver returns the first bits of the received word as the decoded message. If not, then it compares that bit value with each of the stored syndromes. If the syndrome matches, then it means that a data bit in the received word was in error, and the decoder flips that bit and returns the first bit of the received word as the most likely message that was encoded and transmitted. Taking into account H^T matrix, a table (Table 3) is created with the corrective action for each combination of the syndrome bits. These bits are

possible candidates for having an error since any of them could have caused the observed parity errors. A similar table could be generated for four channels transmission with $S_4=0$ [14].

Table 3. Corrective actions for each combination of syndrome bits in a five channel transmission.

| S ₁ | S ₂ | S ₃ | S ₄ | Corrective actions |
|----------------|----------------|----------------|----------------|----------------------------------|
| 0 | 0 | 0 | 0 | no errors |
| 1 | 1 | 0 | 0 | r have an error, flip to correct |
| 0 | 1 | 1 | 0 | g have an error, flip to correct |
| 1 | 0 | 1 | 0 | b has an error, flip to correct |
| 1 | 1 | 1 | 0 | v has an error, flip to correct |
| 0 | 0 | 0 | 1 | i has an error, flip to correct |
| 1 | 0 | 0 | 0 | pr has an error, flip to correct |
| 0 | 1 | 0 | 0 | pg has an error, flip to correct |
| 0 | 0 | 1 | 0 | pb has an error, flip to correct |
| 0 | 0 | 0 | 1 | pv has an error, flip to correct |

Taking as an example Fig. 3(b), the d_{15} and d_{14} levels are too close. The message (d_{14} ; p_7) could be received when transmitting [111101110]. The syndrome S will be given by:

$$S = Y_1 H^T = [1 \ 1 \ 1 \ 0 \ 0 \ 1 \ 1 \ 1 \ 0] H^T = [1110] \quad (12)$$

Applying the corrective action (Table 3) the fourth bit, the violet, has an error and has to flip to recover the original message. The syndrome could be the same even if the two code words are different. When $S_1=1$, $S_2=1$, $S_3=1$ and $S_4=0$, we notice that bit v (violet) appears in the computations for S_1 , S_2 and S_3 (10), so, v is the sole candidate as the bit with the error.

Combining the information given by the generated parity bits and signal levels either the absence or the presence of one error will be easily checked, even for similar values of the different MUX levels. This correction is obvious from the MUX signal under back irradiation (Fig. 2) where data have shown that the MUX signal is strongly enhanced if the violet bit is in the *on* state, allowing confirmation of the presence of the violet bit if generated.

Results show that by using a pin/pin optical processor under steady state irradiation and simultaneously storing the MUX signal due to the received data code and generated parity, consecutive levels in the data code (RGBVI) do not correspond to two near levels in the parity levels [P_R , P_G , P_B , P_V]. For instance, in the message [001001010] (d_2 ; p_{10}) the level d_2 is too near from d_1 level and an error could occur when decoding and the received message could result in [d_1 ; p_{10}]. The syndrome obtained was [0100] that corresponds to an error in the p_G that has to flip from 0 to 1 which corresponds to the level p_{14} what is obviously wrong. Nevertheless, the parity is correct (p_{10}) so, the error comes from the level that should be d_2 [00100].

5.3. Decoding Algorithm

In order to automate the process of recovering the original transmitted data an algorithm was developed and implemented. The transmitted information is decoded by comparing the MUX signal from the code with the simultaneous parity MUX signal under front irradiation, as shown in Fig. 4 and Fig. 5.

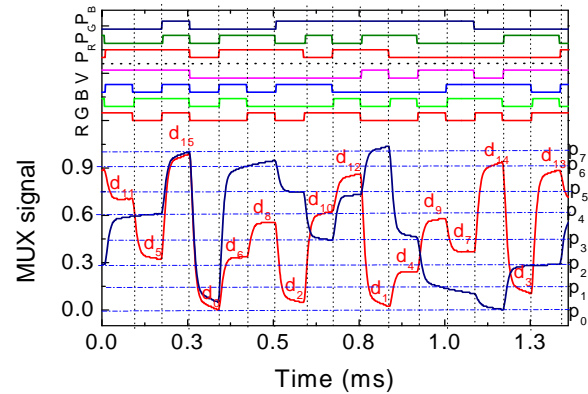


Fig. 4. Code and parity MUX/DEMUX signals under 390 nm front irradiation. On the top the decoded 7-bit word code [R G B V Pr Pg Pb] are shown.

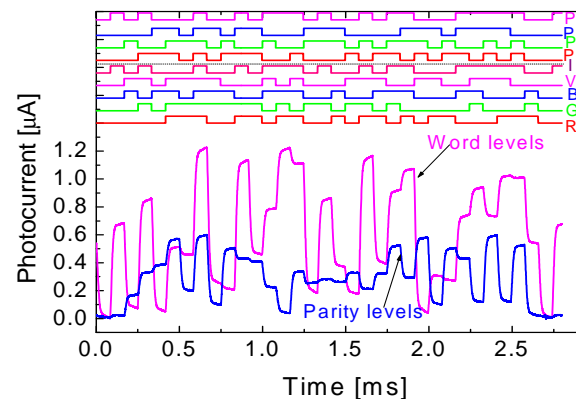


Fig. 5. Code and parity MUX/DEMUX signals under 390 nm front irradiation. On the top the decoded 9-bit word code [R G B V I Pr Pg Pb Pv] are displayed.

The decoding algorithm is based on a proximity search [16] after each time slot is translated to a vector in multidimensional space. The vector components are determined by the signal currents I_1 and I_2 , where I_1 (d levels) and I_2 (p levels) are the currents measured simultaneously under front optical bias for the 4-bit codeword (RGBV) in a four channel transmission or 5-bit codeword (RGBVI) if five channels are used for the word transmission. The correspondent parity levels, [P_R , P_G , P_B] or [P_R , P_G , P_B , P_V] in the respective time slot are also obtained and are assumed to be correct. The result is then compared with all vectors obtained from a calibration sequence (Fig. 3) where to each code level, $d_{(0-31)}$, is assigned the correspondent parity level, $p_{(0-15)}$. The colour bits of the nearest calibration point are assigned to the time slot. An Euclidian metric is applied to measure the distances.

We have tested the algorithm with different random sequences of the channels and we have recovered the original colour bits, as shown in the top of Fig. 4 and Fig. 5.

For simplicity and to guide the eyes, in Fig. 4, for the simultaneous transmission of the data word and parity code (RGBV: P_R, P_G, P_B), for each time slot, the received data (d_{0-15} levels) is marked in the correspondent MUX slots as well as the received parity levels (p_{0-8}) marked as horizontal lines. On the top of both figures the decoded 7-bit coded word (Fig. 4) or the decoded 9-bit coded word (Fig. 5) is exhibited [17].

6. Conclusions

Based on a-SiC:H technology, we presented an optical processor for data error detection and correction using a suitable (9,5) Hamming binary code generator and the syndrome decoding process.

Results show that by comparing the MUX signal due to the received data code word with the generated parity MUX signal, two consecutive levels in the data code (RGBVI) do not correspond to two near levels in the parity levels [P_R, P_G, P_B, P_V] allowing information retrieval.

The generator matrix, the parity check matrix and corrective action for each combination of the syndrome bits depends on the optical gain of both transmitted message and parity bits under lighting irradiation. An algorithm to decode the received data is presented and tested.

Acknowledgements

This work was sponsored by FCT – Fundação para a Ciência e a Tecnologia, within the Research Unit CTS – Center of Technology and systems, reference UID/EEA/00066/2013.

References

- [1]. R. W. Hamming, Error detecting and error correcting codes, *Bell System Technical Journal*, Vol. 29, 1960, pp. 147–160.
- [2]. S. Lin, Y. Ishikawa, K. Wada, Demonstration of optical computing logics based on binary decision diagram, *Optics Express*, Vol. 20, No. 2, 2012, pp. 1378-1384.
- [3]. A. J. Poustie, K. J. Blow, A. E. Kelly, R. J. Manning, All-optical binary half-adder, *Optics Communications*, Vol. 156, 1998, pp. 22–26.
- [4]. Bhattacharya D. K., S. Nandi, Theory and design of SEC-DED-AUED codes, *IEE Proceedings on Computers and Digital Techniques*, Vol. 145, Issue 2, 1998, pp. 121-126.
- [5]. V. Van, T. A. Ibrahim, K. Ritter, P. P. Absil, F. G. Johnson, R. Grover, J. Goldhar, P. T. Ho, All-optical nonlinear switching in GaAs-AlGaAs microring resonators, *IEEE Photonics Technology Letters*, Vol. 14, No. 1, 2002, pp. 74-76.
- [6]. J. N. Roy, D. K. Gayen, Integrated all-optical logic and arithmetic operations with the help of TOAD based interferometer device – alternative approach, *Applied Optics*, Vol. 46, No. 22, 2007, pp. 5304–5310.
- [7]. K. E. Zoiros, G. Papadopoulos, T. Houbavlis, G. T. Kanellos, Theoretical analysis and performance investigation of ultrafast all-optical Boolean XOR gate with semiconductor optical amplifier-assisted Sagnac interferometer, *Optics Communications*, Vol. 258, No. 2, 2006, pp. 114–134.
- [8]. M. Vieira, P. Louro, M. Fernandes, M. A. Vieira, A. Fantoni, J. Costa, Three Transducers Embedded into One Single SiC Photodetector: LSP Direct Image Sensor, Optical Amplifier and Demux Device, *Advances in Photodiodes, InTech*, Chap. 19, 2011, pp. 403-425.
- [9]. M. A. Vieira, M. Vieira, J. Costa, P. Louro, M. Fernandes, A. Fantoni, Double pin Photodiodes with two Optical Gate Connections for Light Triggering: A capacitive two-phototransistor model, *Sensors & Transducers*, Vol. 9, Special Issue, 2010, pp. 96-120.
- [10]. M. Vieira, P. Louro, M. Fernandes, M. A. Vieira, A. Fantoni, J. Costa, Advances in Photodiodes, *InTech*, Chapt. 19, 2011, pp. 403-425.
- [11]. M. A. Vieira, P. Louro, M. Vieira, A. Fantoni, A. Steiger-Garção, Light-activated amplification in Si-C tandem devices: A capacitive active filter model, *IEEE Sensor Journal*, Vol. 12, No. 6, 2012, pp. 1755-1762.
- [12]. M. Vieira, M.A. Vieira, P. Louro, J. Costa, M. Fernandes, A. Fantoni, M. Barata, Multilayer architectures based on a-SiC:H material: Tunable wavelength filters in optical processing devices, *Journal of Nanoscience and Nanotechnology*, Vol. 11, No. 6, 2011, pp. 5299-5304.
- [13]. M. A. Vieira, M. Vieira, V. Silva, P. Louro, M. Barata, Optoelectronic logic functions using optical bias controlled SiC multilayer devices, *MRS Proceedings*, Vol. 1536, 2013, pp. 91-96.
- [14]. M. A. Vieira, M. Vieira, V. Silva, P. Louro, J. Costa, Optical signal processing for data error detection and correction using a-SiCH technology, accepted for publication in *Physica Status Solidi (c)*, 2015.
- [15]. M. A. Vieira, M. Vieira, V. Silva, P. Louro, M. Barata, Error control on spectral data of four-wave mixing based on a-SiC technology, *Phys. Status Solidi, C* 12, No. 1-2, 2015, pp. 181-186.
- [16]. M. A. Vieira, M. Vieira, P. Louro, V. Silva, J. Costa, A. Fantoni, SiC Multilayer Structures as Light Controlled Photonic Active Filters, *Plasmonics*, Vol. 8, No. 1, 2013, pp. 63-70.
- [17]. M. A. Vieira, M. Vieira, P. Louro, Optical processor design for data error detection and correction using a (9,5) binary code generator and the syndrome decoding process, in *Proceedings of the 2nd International Conference on Sensors and Electronic Instrumentation Advances (SEIA'16)*, Barcelona, Castelldefels, Spain, 22-23 September 2016, pp. 147-149.



Characterization and Compensation of the Fixed Pattern Noise in the Output of a CCD Camera

* **Andreas W. WINKLER and Bernhard G. ZAGAR**

Institute for Measurement Technology,
Johannes Kepler University Linz, Altenbergerstraße 69, 4040 Linz, Austria
Tel.: +43 732 2468 5929, fax: + 43 732 2468 5933
E-mail: andreas.winkler@jku.at

Received: 5 November 2016 /Accepted: 5 December 2016 /Published: 30 December 2016

Abstract: A monochrome CCD camera is used in a reflectometer in order to measure the luminance of light reflected by a specimen. This application requires a compensation of the non-uniformities introduced by the optical system, also known as fixed pattern noise. We provide an image formation model and characterize the bias and the dark signal of the CCD sensor and we use a self-built integrating sphere with an inner diameter of 500 mm as a uniform light source in order to characterize the photo sensitivity of the whole optical system. Finally, a new effective approach to compensate the fixed pattern noise pixel by pixel and in dependence of the exposure time is proposed.

Keywords: Camera calibration, Flat-field correction, Fixed pattern noise, Dark signal, Photo response, Integrating Sphere.

1. Introduction

We use a CCD camera from Allied Vision Technologies (model GC1600H) to measure the luminance L of reflected light in a gonio-reflectometer. The reflectometer is used to evaluate the bidirectional reflectance distribution function (BRDF) of metallic specimens [1]. The camera features a monochrome Sony ICX274AL progressive scan 2 megapixel CCD sensor, a 12 bit ADC, and is equipped with a Pentax TV zoom lens (8 – 48 mm).

The camera supplies the digital image f , measured in ADU (analog-to-digital units). Obviously, the image value $f(u, v)$ depends on $L(u, v)$, the mean luminance of the pencil of light which is imaged onto pixel (u, v) . In an ideal camera, f would be proportional to the imaged light field L with the same factor of proportionality for all pixels. A real camera sensor, however, has several imperfections which may be

categorized in two main groups [2]: (a) fixed pattern noise (FPN), and (b) temporal noise [3-4]. Our application of the camera in the reflectometer requires it to supply a real measure of the luminance [5]. Thus, our goal is to compensate the FPN in acquired images.

The word *noise* in the term FPN may be, although widely adopted in the literature, somewhat misleading, because FPN means spatially varying but temporally constant (and thus deterministic) non-uniformities in acquired images [6]. In the remainder of this paper, the single word *noise* in another context than FPN refers to temporal noise only. In related literature [2], the FPN is often further subdivided into the so-called dark signal non-uniformity (DSNU) and the photo-response non-uniformity (PRNU). The DSNU can be observed under dark conditions and the PRNU takes effect as soon as light strikes the image sensor. After presenting the physical image formation model in Sec. 3, we show measurements of the bias and the dark

signal of the CCD sensor as well as of the photo sensitivity of the whole optical system in Sec. 4. The photo sensitivity is evaluated by means of a custom integrating sphere which is introduced in Sec. 2. Based on the measurements, we finally propose a method for compensation of the FPN in Sec. 5 which is applied pixel by pixel. The presented method is more accurate than the conventional so-called flat-field correction which is often used in astronomical imaging.

As the characteristics of the camera depend on the temperature of the CCD sensor and the electronics to a high degree [7], we have implemented temperature stabilization of the camera. The stabilization uses a thermoelectric cooler in a closed loop control to actively cool the aluminum housing of the camera (Fig. 1). For all measurements in this paper, we have stabilized the housing temperature at $(20 \pm 0.1)^\circ\text{C}$ ¹. This operating temperature has the advantage that it is close to the ambient temperature and hence a possible temperature gradient along the housing is minimized. It is also well above the dew point in order to avoid harmful water condensation.

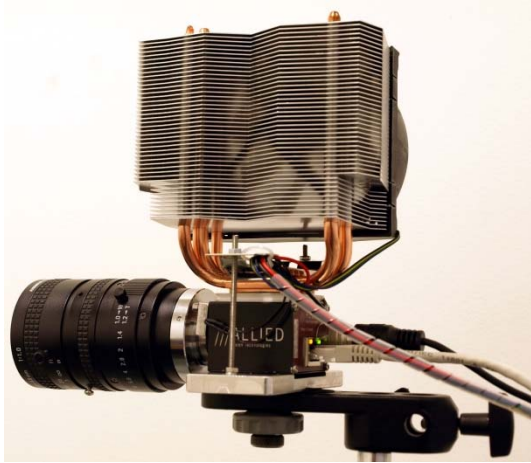


Fig. 1. The thermoelectric cooler is clamped between the housing of the camera and a fan.

1.1. Mathematical Notation

We will denote matrices with bold italic letters, e.g. the image \mathbf{f} , and we will use $f(u, v)$ to refer to a single entry of \mathbf{f} . Unless otherwise stated, mathematical operations between two matrices are carried out on a per-element basis.

Throughout this paper, we will make use of two different sample means. We call

$$\langle \mathbf{f} \rangle = \frac{1}{MN} \sum_{u,v} f(u, v) \quad (1)$$

the spatial mean and

¹ Without the stabilization, the housing heats up to about 45°C during operation.

$$\bar{\mathbf{f}} = \frac{1}{N_f} \sum_{n=1}^{N_f} f(u, v; n) \quad (2)$$

the temporal mean [8], where M and N are the dimensions of an image or matrix and N_f is the number of temporally averaged images or matrices. Note that the former is a scalar value, whereas the latter is still an image or matrix.

We will also introduce a few random variables and we will make no difference in notation between a random variable and its realization² whereby the difference should be clear from the context.

2. The Integrating Sphere

The custom integrating sphere (Fig. 2) with a diameter of 500 mm provides, in the ideal case, a uniform and fully diffuse light field at the 140 mm wide exit port and is used to evaluate the photo sensitivity of the optical system (Sec. 4.3).

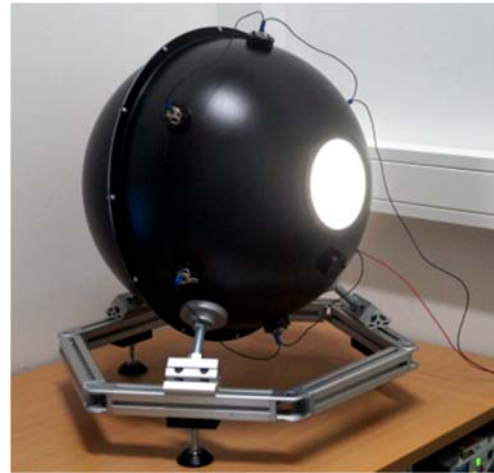


Fig. 2. The integrating sphere is used to evaluate the photo sensitivity of the optical system.

The sphere is made of two metal-spun and powder-coated aluminum hemispheres. Inside it is additionally coated with white and diffusely reflecting barium sulfate with a reflectance in the visible wavelength range of more than 97 %. It is illuminated by six high power LEDs with three of them having a correlated color temperature (CCT) of 3000 K and a luminous flux of 300 lm@1050mA and the other three having 5700 K and 360 lm@1050mA. It is possible to set a desired CCT by means of driving the two LED types with appropriate currents. With all six LEDs at nominal current of 1050 mA, the luminance at the exit port is about $1.46 \times 10^4 \text{ cd/m}^2$. The LEDs can temporarily be operated at up to 3A to increase light

² Some authors use capital letters for a random variable and lowercase letters for a corresponding realization.

output even further. For our experiments, all six LEDs have been operated at a constant current of 500 mA.

Important quality characteristics of the sphere are the spatial and the angular homogeneity of the output light field. We have used the CCD camera at hand to measure both of them. In order to determine the spatial homogeneity, we have applied a linear and a rotation stage to move the camera around the whole area of the exit port automatically and for the angular measurement we have used just the rotation stage to rotate the camera around its own axis, one time horizontally and the other time vertically. In the acquired images, we build the average of a 150px × 150px center section in order to get a value which is proportional to the luminance. The center section instead of the whole image is used to improve the directionality of the measurements. The results are shown in Fig. 3 and Fig. 4.

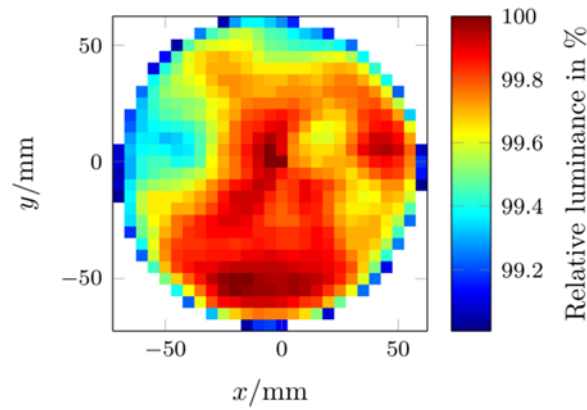


Fig. 3. Spatial homogeneity of the output light field.

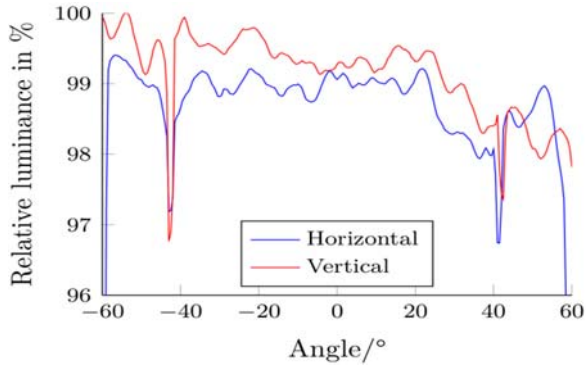


Fig. 4. Angular homogeneity of the output light field measured in the horizontal and the vertical direction.

In the plot of the spatial luminance distribution (Fig. 3) it can be seen that the relative luminance stays well above 99 % of the maximum luminance and in the plot of the angular luminance distribution (Fig. 4), the relative luminance stays above 98 % in the range from -40° to $+40^\circ$. The negative peaks at $\pm 45^\circ$ can be explained by the influence of the interface where the two aluminum hemispheres are stitched together.

Regarding the homogeneity and the optical output power, the performance of the sphere compares well

to those commercially available, while the manufacturing costs were just about one-tenth.

3. An Image Formation Model

The CCD camera sensor principle is based on photoelectrons generated in sensor cells, also known as pixels. The photoelectrons per unit time for all pixels can be summarized in the matrix of photo currents \mathbf{i}_p . Our model assumes that \mathbf{i}_p is proportional to the matrix \mathbf{E} of illuminances at the image pixels:

$$\mathbf{i}_p \propto \mathbf{E} \quad (3)$$

Furthermore, it can be shown [1] that \mathbf{E} is described by

$$\mathbf{E} = \mathbf{a} \frac{\pi}{4} \left(\frac{D}{b} \right)^2 \cos^4 \alpha \mathbf{L}, \quad (4)$$

when the optics is approximated by a single thin lens. Here, \mathbf{a} is the matrix of attenuation factors which are determined by the transmittance of the lens and distortions in the optical path, D , is the diameter of the entrance pupil, b , is the image distance, α , is the matrix of angles between the principal ray of each pixel and the optical axis of the sensor, and \mathbf{L} , is the imaged light field.

Equations (3) and (4) can be combined by using a single matrix \mathbf{g}_p of factors of proportionality, measured in $A/(cd/m^2)$:

$$\mathbf{i}_p = \mathbf{g}_p \mathbf{L}. \quad (5)$$

This matrix depends, besides the parameters of the optics noted in Eq. (4), on characteristics of the CCD sensor like the effective pixel area, the fill factor, the quantum efficiency, or the charge collection efficiency [2].

There are also thermally induced charges in the sensor cells, even if no light strikes the sensor. These charges are the source of the so-called dark current \mathbf{i}_d . The dark current is well understood and described in [6], for example. It depends exponentially on the sensor temperature.

During the exposure time t_s of an acquisition, \mathbf{i}_d and \mathbf{i}_p are integrated and the matrices of mean numbers of generated dark and photo charges are

$$\begin{aligned} \frac{(\mathbf{i}_d + \mathbf{i}_p)t_s}{q} &= \frac{\mathbf{i}_d t_s}{q} + \frac{\mathbf{i}_p t_s}{q} \\ &= \frac{\mathbf{i}_d t_s}{q} + \frac{\mathbf{g}_p \mathbf{L} t_s}{q} \\ &= \overline{\mathbf{n}}_d + \overline{\mathbf{n}}_p \end{aligned} \quad (6)$$

with q being the elementary charge. The actual values in \mathbf{n}_d and \mathbf{n}_p are subject to shot noise and can thus be modeled as Poisson distributed random variables with $\overline{\mathbf{n}}_d$ and $\overline{\mathbf{n}}_p$ being the matrices of the corresponding Poisson parameters: $\mathbf{n}_d \sim \mathcal{P}(\overline{\mathbf{n}}_d)$ and $\mathbf{n}_p \sim \mathcal{P}(\overline{\mathbf{n}}_p)$. Note

that the Poisson parameter denotes the mean as well as the variance³. For large values of the parameter, the Poisson distribution can be approximated by the normal distribution. The shot noise implies an inherent limit for the attainable signal-to-noise ratio (SNR) of the sensor.

Directly after the exposure, the collected charges are transferred off the sensor⁴ and are serially applied to a capacity. The capacity converts the charges to a voltage which is amplified and finally AD-converted [2]. This process can be modeled by a bias image \mathbf{f}_b and a matrix of factors \mathbf{g}_c which denotes the conversion between the amount of charge and the output signal in ADU. The bias image is modeled to contain additive white Gaussian noise. This noise is often referred to as read out noise [3].

The final image is composed of the bias image and the dark-, and the photo signal and can be written as

$$\begin{aligned} \mathbf{f} &= \mathbf{f}_b + (\mathbf{n}_d + \mathbf{n}_p) \mathbf{g}_c \\ &= \mathbf{f}_b + \mathbf{f}_d + \mathbf{f}_p. \end{aligned} \quad (7)$$

4. Analysis of the FPN

The pixels of the CCD sensor differ in the bias signal, the dark current and the photo sensitivity. These temporally constant inter-pixel variations are the cause of the so-called fixed pattern noise.

The FPN is analyzed in the following subsections by looking at (a) bias images, (b) dark images, and (c) flat-field images. Flat-field images for different exposure times t_s are acquired with the lens directed at the exit port of the integrating sphere, which provides a uniform and flat light field. Dark images for different t_s are produced by suppressing the photo signal \mathbf{f}_p in the acquisitions. In practice, this is achieved with an opaque lens cap. Finally, bias images are acquired by suppressing the dark signal \mathbf{f}_d in addition to \mathbf{f}_p . This is done by choosing t_s as low as possible. For the camera at hand, the minimal t_s is 10 μ s.

4.1. The Bias Image

The mean bias image $\overline{\mathbf{f}_b}$ shown in Fig. 5 is the result of averaging 256 \times 2048 single bias frames. It shows a vertically striped pattern and has a darker region on the very left. These effects may be caused by the readout electronics and a non-uniform temperature distribution over the sensor. The spatial

mean $\langle \overline{\mathbf{f}_b} \rangle$ is ~ 36.8 ADU. This is a bit less than 1 % of the total dynamic range of 4095ADU.

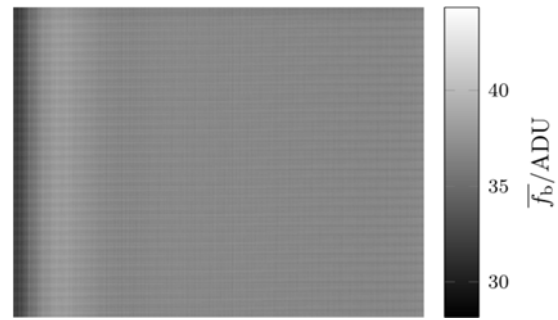


Fig. 5. The averaged bias image $\overline{\mathbf{f}_b}$.

The bias image can be further subdivided in

$$\mathbf{f}_b = \mathbf{f}_{dc} + \boldsymbol{\eta}_w \quad (8)$$

with the steady component \mathbf{f}_{dc} and additive white Gaussian noise $\boldsymbol{\eta}_w$. An interesting observation during our experiments was that \mathbf{f}_{dc} is not entirely constant, but with each new acquisition sequence⁵ it randomly appears as one out of a finite number N_{dc} of different steady components $\mathbf{f}_{dc,i}$, whereby the number N_{dc} and the steady components $\mathbf{f}_{dc,i}$ themselves depend on the temperature and possibly on other parameters. This effect is presumably caused by a camera-internal and temperature-dependent offset compensation.

When the camera housing temperature is stabilized at 20°C, we have $N_{dc} = 8$ and the mean variance between single pixels of the different steady components $\mathbf{f}_{dc,i}$ ($\sim 4\text{ADU}^2$) is very small as compared to the mean variance of $\boldsymbol{\eta}_w$ ($\sim 200\text{ADU}^2$). Thus, this effect can be safely neglected in most cases.

4.2. The Dark Signal

While the bias images were acquired at the minimal possible exposure time, the effect of the dark current is analyzed by means of dark images acquired with 128 different t_s between 10 μ s and 2 s. At each of these exposure times, 256 dark images are acquired. Moreover, this measurement is repeated three times. Thus, 256 \times 3 images are averaged at each exposure time in total in order to reduce temporal noise.

Fig. 6 shows the trends of three typical pixels in the averaged dark images. As the physical model predicts, the dark signal is linear in t_s in good

³ As the Poisson parameter is without unit, there is no contradiction regarding units in this statement.

⁴ There are different kinds of sensor structures available, the most common being (a) frame transfer, (b) interline

transfer and (c) frame-interline transfer CCDs [2]. The sensor at hand is an interline transfer CCD.

⁵ In order to modify camera settings like the acquisition time, the current acquisition sequence has to be stopped and a new one has to be started. In MATLAB, this corresponds to a stop/start of the video object associated with the camera.

approximation. Thus, it can be modeled by means of linear regression lines for each pixel. The slope $k_d(u, v)$ of such a line is proportional to the magnitude of dark current generated in pixel (u, v) and we call it the dark signal rate of this pixel, measured in ADU/s.

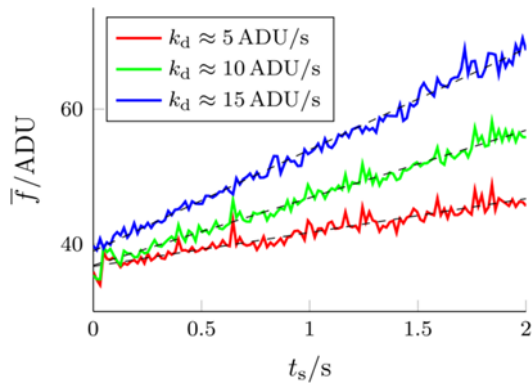


Fig. 6. The trends of three typical pixels in the averaged dark images versus exposure time. The corresponding regression lines are shown dashed.

The histogram of the dark signal rates is shown in Fig. 7. The range from (0 to 35)ADU/s covers 99.14 % of all pixels of the sensor. The mean dark signal rate is about 8.84ADU/s. This indicates a quite low impact of the mean dark current of the temperature-stabilized camera: After an exposure time of $t_s = 1$ s, the mean dark signal would be just 0.22 % of the whole dynamic range of the sensor.

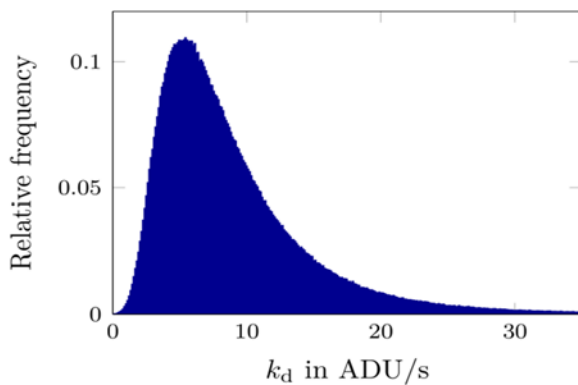


Fig. 7. Histogram of the dark signal rates. The Histogram is normalized such that the covered area equals 1.

However, there also a few pixels which exhibit untypical dark signal behavior. Such pixels can be roughly classified into two categories which are not mutually exclusive: (a) pixels with exceptional high dark signal rates, the so-called hot pixels, and (b) pixels with varying dark signal rates.

The trends of some of the pixels with the highest dark signal rates are shown in Fig. 8. The rates range from ~ 1100 ADU/s for the purple curve up to ~ 19200 ADU/s (measured in the linear range) for the

red curve. An interesting effect is that the dark signal obviously saturates before it reaches the upper limit of 4095ADU. The red curve saturates at ~ 3710 ADU, while the yellow curve saturates yet at ~ 750 ADU. Another observation is that some of the hot pixels exhibit a slightly nonlinear behavior [9] as it is the case with the green curve, for example.

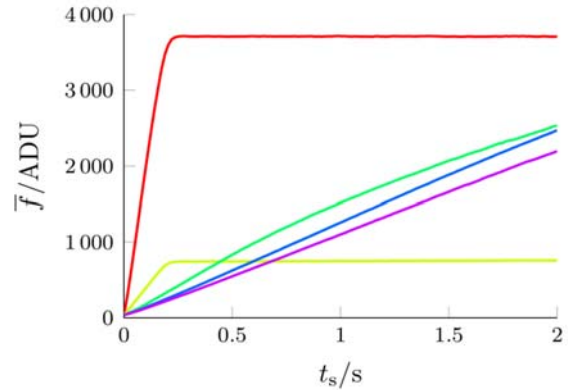


Fig. 8. The trends of five of the pixels with the highest dark current.

When we define the threshold for the dark signal rate of hot pixels to be 100ADU/s, we have 496 pixels above this value. This means that ~ 0.0251 % of all sensor pixels are hot pixels.

The second main category of untypical dark signal behavior comprises those pixels with a varying dark signal rate. The dark current generated in these pixels seems to alternate randomly between two or more discrete values. The signals of three examples of this group are shown in Fig. 9.

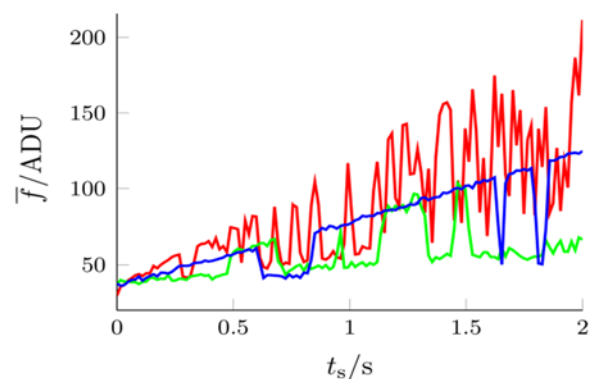


Fig. 9. Three examples of pixels with varying dark current.

We define pixels to be of this type when the maximum absolute value of the forward difference of the corresponding dark signal is above a certain threshold. In our experiments, 8ADU has proven to be a reasonable value and using this threshold we have identified ~ 1.96 % of all pixels to be of this category.

4.3. The Photo Signal

For evaluation of the photo signal, we use images of the exit port of the integrating sphere which provides the spatially constant light field L_{ref} . We have acquired flat-field images with 128 different exposure times t_s between 10 μs and 13.3 ms. The upper bound of 13.3 ms has been chosen such that all pixels reach at least an output signal of 4000ADU. At each of these exposure times, 128 flat-field images have been averaged in order to reduce temporal noise.

The corresponding trend for three typical pixels is shown in Fig. 10. It can be observed that the pixels have a different photo sensitivity and that the trends are slightly nonlinear in t_s [9] (even before reaching the saturation level at 4095ADU).

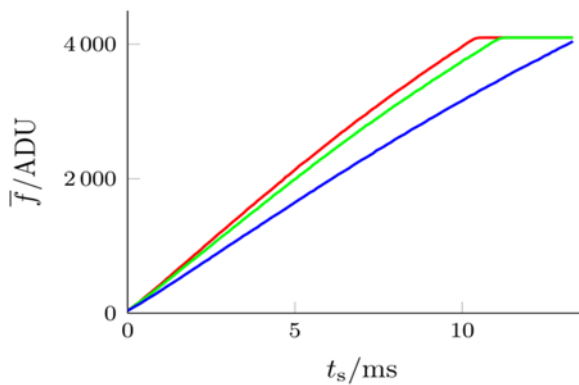


Fig. 10. The trends of three pixels versus exposure time in the averaged flat-field image. The used pixels are those with the highest (red), the mid-level (green) and the lowest (blue) photo sensitivity. The maximum output value is 4095ADU.

The varying photo sensitivity can be observed even more clearly in a flat-field image itself. The image f_{flat} shown in Fig. 11 is the result of averaging 512 flat-field images acquired at $t_s = 6$ ms. The gray values in the image are scaled from the minimum value of 1963ADU to the maximum value of 2532ADU. The plot in Fig. 12 shows the values of the pixel row which is marked with the blue line in Fig. 11.

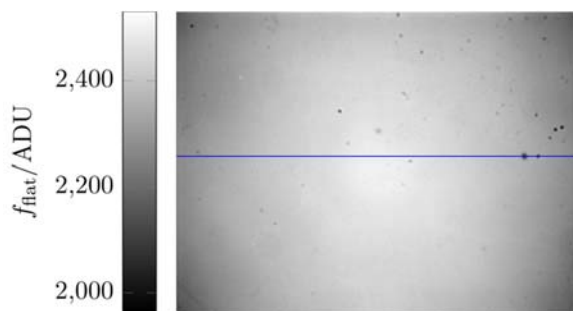


Fig. 11. The mean of 512 flat-field images acquired at $t_s = 6$ ms.

The high number of averaged images causes the temporal noise to be effectively removed and the FPN to be dominant. The FPN exhibits a low frequency part which is mainly caused by vignetting of the lens and a high frequency part which is presumably caused by the read-out electronics. The visible dark spots are caused by distortions in the optical path, like dust or smear on the optics.

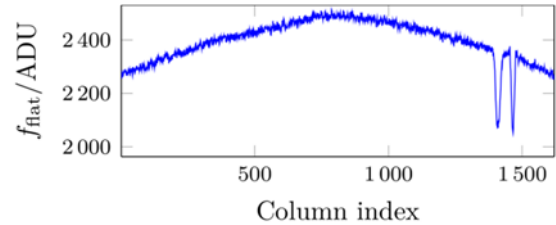


Fig. 12. Values of a single row of the flat-field image.

5. Compensation of the FPN

As the FPN is temporally constant, it can be considered a systematic error which can be corrected. In this section, we derive a way to calculate L (or at least an image proportional to L) based on an acquisition f and its given exposure time t_s .

We infer from Eqs. (6) and (7) that the photo signal f_p in an acquisition is a function of the product of the acquired light field L and the exposure time t_s . In other words: For a given f_p , the product $L t_s$ is constant. As a consequence, we can write

$$L t_s = L_{\text{ref}} t_{s,\text{ref}}(f_p) \quad (9)$$

Here, L_{ref} describes the spatially constant reference light field provided by the integrating sphere and $t_{s,\text{ref}}(f_p)$ is a function which maps the given photo signal f_p to the matrix of reference exposure times $t_{s,\text{ref}}$ which would be required to generate f_p under the assumption that L_{ref} is imaged by the optical system.

Rearranging Eq. (9) and substituting the quantities from Eq. (7) for f_p , we finally get the expression

$$L = \frac{L_{\text{ref}} t_{s,\text{ref}}(f - f_b - f_d)}{t_s} \quad (10)$$

The acquisition f and the exposure time t_s are given. For now, we assume the exact value of L_{ref} from the integrating sphere to be known, too. What we yet need in order to compute expression (10), is (a) an estimate \hat{f}_b of the bias image, (b) an estimate \hat{f}_d of the dark signal (which depends on the exposure time), and (c) an estimate $\hat{t}_{s,\text{ref}}(f_p)$ of the function which maps a given photo signal to the reference exposure time.

For the bias image estimate \hat{f}_b (a), the following method has proven to work well: We perform a polynomial regression of order 4 to approximate the

dark signal measurements of pixels with typical behavior presented in Sec. 4.2 and use the resulting matrix of constant coefficients \mathbf{a}_0 as the estimate of the bias. The higher order polynomial deals with nonlinearities which may occur in the dark signal. For pixels with untypical behavior, the polynomial regression does not yield satisfying results and we thus use the mean bias image $\overline{f_b}$ presented in Sec. 4.1. This approach can be summarized as follows:

$$\hat{f}_b(u, v) = \begin{cases} a_0(u, v), & \text{typical} \\ \overline{f_b}(u, v), & \text{untypical} \end{cases} \quad (11)$$

The dark signal has been shown to be linear in t_s in good approximation for the majority of the pixels. Thus, we use

$$\hat{f}_d(t_s) = \hat{\mathbf{k}}_d t_s \quad (12)$$

for the dark signal estimate (b). In order to determine the matrix of dark signal rates $\hat{\mathbf{k}}_d$, we apply a least squares approach to determine the slopes of the lines which approximate the measurements presented in Sec. 4.2, while having the intercepts of these lines fixed at \hat{f}_b from Eq. (11).

The estimate $\hat{t}_{s,\text{ref}}(f_p)$ of the function for the reference exposure time (c) is performed using the measurements of the photo sensitivity in Sec. 4.3. In a first step, we subtract \hat{f}_b and $\hat{f}_d(t_s)$ from the acquired image f to isolate the photo signal f_p . In a second step, we model the reference exposure time by a polynomial of order 4:

$$\hat{t}_{s,\text{ref}}(f_p) = \sum_{i=0}^4 \mathbf{b}_i f_p^i. \quad (13)$$

Finally, polynomial regression is used to determine the matrices of coefficients \mathbf{b}_i . The results of the regression for the three example pixels from Fig. 10 are shown in Fig. 13 as dashed lines.

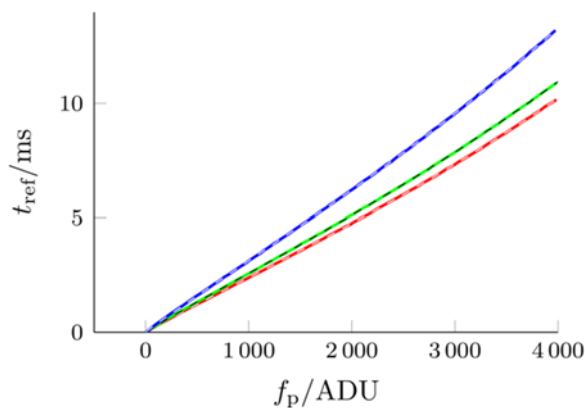


Fig. 13. The reference exposure time in terms of the photo signal. The results of the polynomial regression are shown dashed.

Only measurements with an output signal less than 4000ADU have been used for the regression. Note that the axes in Fig. 13 are interchanged as compared to the axes in Fig. 10: Now, $f_p(u, v)$ is the independent variable, whereby $t_{\text{ref}}(u, v)$ is the dependent variable.

It should be noted that the measurement of the photo sensitivity and the polynomial regression in order to determine the matrices of coefficients \mathbf{b}_i have to be repeated as soon as a parameter of the optical system (e.g. the zoom level of the lens) changes.

5.1. Evaluation of the FPN Compensation

The proposed method is verified by applying it to the flat-field image f_{flat} from Fig. 11. The results are shown in Figs. 14 and 15.

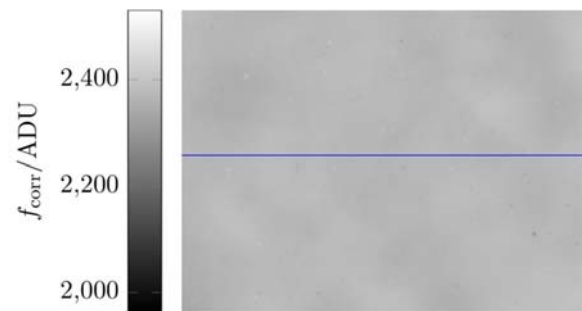


Fig. 14. The corrected flat-field image.

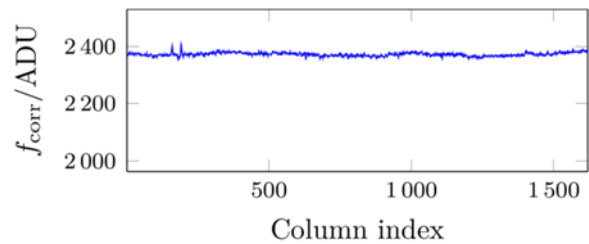


Fig. 15. A single row of the corrected flat-field image.

Usually the exact value of L_{ref} is not exactly known. However, from Eq. (10) it can be seen that L_{ref} can be used as arbitrary scaling factor, as long as it is the same for the whole image. Here, we have used

$$L_{\text{ref}} = \langle f_{\text{flat}} \rangle / \langle f_{\text{corr}} \rangle \quad (14)$$

in order to make the original and the corrected image easily comparable.

The corrected image is reasonably flat. The low frequency FPN is effectively eliminated and also the high frequency FPN is significantly reduced. Even the dark spots from the original image are compensated. There are a few distortions in the corrected image, as can be seen around column 200 in Fig. 15. These are either caused by local inhomogeneities in the output light field of the sphere or by distortions in the optical path which have changed between the measurements

of the photo sensitivity and the acquisition of the flat-field image.

6. Conclusion

An optical system, consisting of a CCD camera and a zoom lens has been characterized by means of the FPN. We have done measurements to evaluate the bias, the dark signal in dependence of the exposure time and the photo sensitivity by means of a custom integrating sphere. Using these measurements, a method has been proposed to correct the FPN pixel by pixel and in dependence of the exposure time. Finally, we have verified our method by applying it to a flat-field acquisition.

Acknowledgement

This work has been [partially] supported by the Austrian COMET-K2 programme of the Linz Center of Mechatronics (LCM), and was funded by the Austrian federal government and the federal state of Upper Austria.

References

- [1]. A. Winkler, B. Zagar, Building a gonireflectometer - a geometrical evaluation, in *Proceedings of the IEEE*

International Conference Instrumentation and Measurement Technology (I2MTC 2015), 2015, pp. 1900-1905.

- [2]. J. Nakamura, *Image Sensors and Signal Processing for Digital Still Cameras*, CRC Press, 2005.
- [3]. K. Irie, A. E. McKinnon, *et al.*, A Technique for Evaluation of CCD Video-Camera Noise, *IEEE Transactions on Circuits and Systems for Video Technology*, Vol. 18, No. 2, 2008, pp. 280-284.
- [4]. G. Healey, R. Kondepudy, Radiometric CCD camera calibration and noise estimation, in *IEEE Transactions on Pattern Analysis and Machine Intelligence*, Vol. 16, No. 3, 1994, pp. 267-276.
- [5]. A. Winkler, B. Zagar, CCD Camera Characterization by means of a Custom Integrating Sphere, in *Proceedings of the 2nd International Conference on Sensors and Electronic Instrumentation Advances*, International Frequency Sensor Association (IFSA) Publishing, 2016, pp. 47-51.
- [6]. J. Lukás, *et al.*, Digital Camera Identification from Sensor Pattern Noise, in *IEEE Transactions on Information Forensics and Security*, Vol. 1, No. 2, 2006, pp. 205-214.
- [7]. R. Widenhorn, *et al.*, Temperature dependence of dark current in a CCD, in *Proceedings of the Conference Series Society of Photo-Optical Instrumentation Engineers (SPIE)*, Vol. 4669, 2002, pp. 193-201.
- [8]. R. C. Gonzalez, R. E. Woods, *Digital Image Processing*, 3rd Ed., Pearson Prentice Hall, 2008.
- [9]. E. G. Stevens, Photoresponse Nonlinearity of Solid-State Image Sensors with Antiblooming Protection, in *IEEE Transactions on Electron Devices*, Vol. 38, No. 2, 1991, pp. 299-302.



Published by International Frequency Sensor Association (IFSA) Publishing, S. L., 2016 (<http://www.sensorsportal.com>).

**Universal Frequency-to-Digital Converter
(UFDC-1 and UFDC-1M-16)
in MLF (5 x 5 x 1 mm) package**

**SMALL WORLD -
BIG FEATURES**

SWP, Inc., Toronto, Ontario, Canada,
Tel. + 34 696067716, fax: +34 93 4011989, e-mail: sales@sensorsportal.com
http://www.sensorsportal.com/HTML/E-SHOP/PRODUCTS_4/UFDC_1.htm

Electrochemical Study of Delta-9-Tetrahydrocannabinol by Cyclic Voltammetry Using Screen Printed Electrode, Improvements in Forensic Analysis

^{1,2} Marco Antonio BALBINO, ^{1,2} Izabel Cristina ELEOTERIO,
¹ Marcelo Firmino de OLIVEIRA and ² Bruce Royston McCORD

¹ Departamento de Química, Grupo de Estudos em Eletroquímica e
Química Forense, Faculdade de Filosofia, Ciências e Letras de
Ribeirão Preto, USP, Ribeirão Preto, SP 14040-901, Brazil

² Department of Chemistry and Biochemistry, Florida International University, 11200 SW 8th Street,
Miami, FL 33199, United States

² Tel.: +1 305 348 7543, fax: +1 305 348 377

² E-mail: mccordb@fiu.edu

Received: 5 November 2016 /Accepted: 5 December 2016 /Published: 30 December 2016

Abstract: Rapid screening of seized drugs is a continuing problem for governmental laboratories and customs agents. Recently new and cheaper methods based on electrochemical sensing have been developed for the detection of illicit drugs. Screen printed electrodes are particularly useful in this regard and can provide excellent sensitivity. In this study, a carbon screen printed electrode for the voltammetric analysis of Δ^9 -THC was developed. The analysis was performed using cyclic voltammetry with $0.15 \text{ mol} \times \text{L}^{-1}$ potassium nitrate as a supporting electrolyte. In the analysis, a Δ^9 -THC standard solution was added to the surface electrode by a drop coating method. A study of scan rate, time of pre-concentration, and concentration influence parameters showed versatility during the investigation. The high sensitivity, quantitative capability and low limit of detection ($1.0 \mu\text{mol} \times \text{L}^{-1}$) demonstrate that this electrochemical method should be an attractive alternative in forensic investigations of seized samples.

Keywords: Detection, Cyclic voltammetry, Screen printed electrodes, Delta-9-tetrahydrocannabinol, Versatility.

1. Introduction

Cannabis, a widely used illicit drug [1-4], contains delta-9-tetrahydrocannabinol (Δ^9 -THC), a primary terpenophenolic substance which can induce psychosis, and reduction of cognition [2-4]. When a marijuana sample is seized, the sample is first extracted in organic media and then a presumptive test is performed. Typically, colorimetric reagents such as Fast Blue B salt or Duquenois–Levine are used. [5].

These tests produce a change of color when Δ^9 -THC and other cannabinoids (such as Cannabinol or Cannabidiol) are present. This test can also be combined with thin layer chromatography for additional specificity [6]. However, these tests can produce false positive and false negative results due to a variety of interfering substances [7]. For confirmatory results, many countries follow the recommendations of The Scientific Working Group for the Analysis of Seized Drugs – SWGDRUG

[8-9]. The SWGDRUG guidelines divide analytical methods into a set of three groups based on specificity. In general, colorimetric and other less specific tests are defined as group C, more specific tests such as chromatography are placed in group B, and highly specific spectroscopic and spectrometric tests are placed in group A. Conclusive identification usually involves a presumptive test such as C or B followed by a more confirmatory type A test. (See Table 1) Unfortunately, more specific analytical techniques (classified as A category) are not always available in smaller laboratories. Thus, one complementary type C procedure and two chemical analyses in category B may be carried out as an alternative [8-13].

Table 1. Recommendations purposed for forensic test illegal drugs [6-11, 21].

| Category A | Category B | Category C |
|-----------------------|----------------------------|---------------------------|
| Raman | GC, LC, TLC | Color tests |
| NMR | Capillary Electrophoresis | Fluorescence spectroscopy |
| Infrared Spectroscopy | Pharmaceutical identifiers | UV Spectroscopy |
| MS | Micro \ macro tests | Immunoassay |
| X-ray Diffractometry | For Cannabis only | Melting point |

1.1. The Advances of Electrochemical Methods in Forensic Analysis

Recently, newer and cheaper methods have been developed for analyzing illicit drugs. For example, the detection of illegal drugs at low concentrations can be carried out using voltammetric techniques. These procedures can be quite selective and quantitative [13]. The low cost of the electrochemical instrumentation, as well as its potential application in providing determining electrochemical reaction mechanisms, [14-16] has motivated several groups to develop methods for detecting illicit drugs. For example voltammetric analysis has been used in the determination of cocaine [10, 13, 17-21], as well as 3,4-methylenedioxy-methamphetamine (*ecstasy*) [22-24]. For the electrochemical detection of Δ^9 -THC, there are methods for both indirect [25-26] and direct analysis using voltammetry. Carbon paste electrodes (with or without chemical modification) have shown reliable results for cannabinoid detection [2, 27]. Voltammetric analysis of Δ^9 -THC (following extraction of seized marijuana samples) using glassy carbon electrode in organic media produced limits of detection between 1×10^{-9} to $1 \times 10^{-7} \text{ mol} \times \text{L}^{-1}$. The novel electrochemical procedure could easily differentiate between five different plant species which produced false positives during colorimetric testing [6].

1.2. Screen Printed Electrodes

Screen-printed electrodes (SPEs) present an easily accessible platform for voltammetric measurements. These devices have 3 electrodes printed on a flat ceramic or plastic surface and are designated for working with microvolumes of analytes. The low volume requirement and facile surface access permit rapid measurements [28]. There are a number of publications on the application of voltammetric analysis in forensic science [13]. Aribas, *et al.*, studied the determination of cocaine using homemade SPE's [29], and carbon screen printed electrodes (CSPE) modified with the enzyme cytochrome P450 [30-31]. Commercially manufactured SPE's have proven useful in the determination of cocaine following modification of the working electrode surface by electrodeposition of CoCl_2 and $\text{K}_3\text{Fe}[(\text{CN})_6]$ in an aqueous solution [13] or after chemical modification by drop coating using Schiff Base films [10].

3,4-Methylenedioxyamphetamine and 4-methoxyamphetamine, have been detected by electrochemistry using graphite screen printed electrode [23]. CSPE devices have also proved useful in the detection of Δ^9 -THC in marijuana in seized sized samples [13], and in an undiluted saliva, using N-(4-amino-3-methoxyphenyl)-methanesulfonamide as a mediator [32]. Cyclic voltammetry permits the study of electroactive substances given by the potentials at which oxidation or reduction occurs, and the intensity of anodic peak current, I_{pa} or cathodic peak current, I_{pc} [33-35]. In this paper, the goal was to examine the voltammetric behavior of Δ^9 -THC using a supporting electrolyte in aqueous solution [2, 27] by CSPE.

2. Experimental

2.1. Reactants and Solutions

A standard solution of Δ^9 -THC 1 mg/mL (Cerilliant) and potassium nitrate (Acros Organics) were employed to prepare the solutions in this study. Δ^9 -THC was diluted in methanol. $0.15 \text{ mol} \times \text{L}^{-1}$ potassium nitrate was prepared in deionized water and used as a supporting electrolyte. This solution was purged with nitrogen gas for 15 minutes prior to use.

2.2. Cyclic Voltammetry

CV experiments were performed on a potentiostat Autolab model 128 N coupled to a microcomputer controlled by Nova 2.0 software. Carbon screen printed electrodes from DropSens (model DRP-110) is constituted by working (4 mm in diameter) and counter electrode of carbon, and reference electrode of Ag. All voltammetric measurements were carried out in triplicate under optimized parameters. A drop

coating method was used to add a small quantity of Δ^9 -THC standard solution onto the surface of the working electrode. This was allowed to dry at room temperature for few minutes [27].

The influence of concentration was determined using an applied potential from -0.8 V to 0.9 V (vs. Ag - SPE) at a scan rate of $100 \text{ mV} \times \text{s}^{-1}$. A potential of -0.5 V for 60 seconds was used to pre-concentrate Δ^9 -THC species on the electrode surface.

3. Results and Discussion

3.1. Voltammetric Behavior of Supporting Electrolyte

The Voltammetric response to $10 \mu\text{L}$ of the supporting electrolyte solution on the surface electrode is illustrated in Fig. 1. A potential of -0.8 to 0.8 V vs. Ag-SPE, was applied at a scan rate of $100 \text{ mV} \times \text{s}^{-1}$. The cyclic voltammogram indicates the expected behavior with an absence of faradaic (cathodic and anodic) peaks.

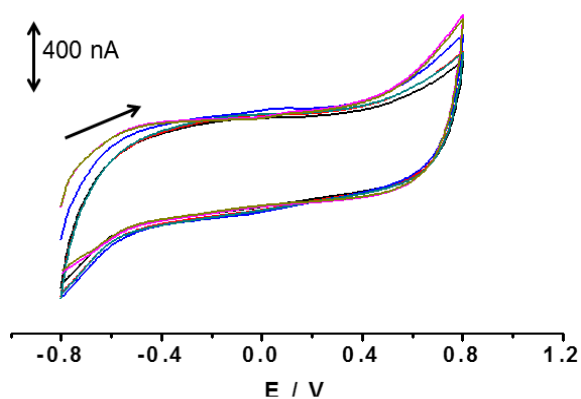


Fig. 1. Cyclic voltammogram of the $0.1 \text{ mol} \times \text{L}^{-1}$ KNO_3 supporting electrolyte solution.

3.2. Accumulation Time

An $18 \mu\text{mol} \times \text{L}^{-1}$ Δ^9 -THC standard was used to optimize the accumulation time. This step occurs prior to the voltammetric scan and is utilized to preconcentrate the sample on the surface of the working electrode due to an attraction between the molecule and surface charges. As shown in Fig. 2, a proportional increase in the anodic peak current (I_{pa} at 0.13 V vs. Ag-SPE) occurs during the time of accumulation, reaching a plateau after that 80 seconds (See Fig. 3). Fig. 4 illustrates the oxidation of the Δ^9 -THC phenol group which involves the loss of one electron and one proton generating a radical phenoxy group [2, 5-6, 9, 13] and subsequent polymeric products [2]. This process passivates the electrode due to saturation of the molecule on the electrode surface. [26-27, 35-36].

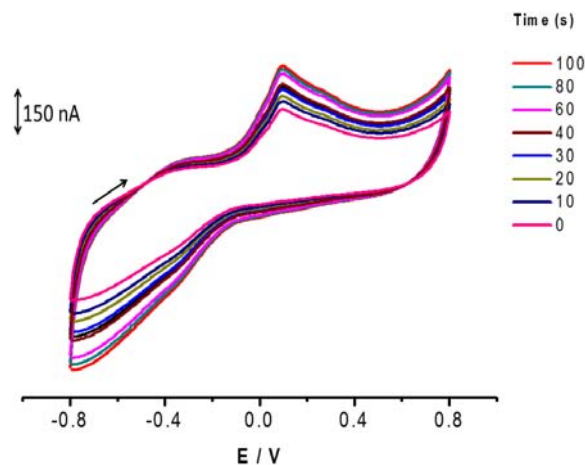


Fig. 2. Cyclic voltammogram of $18 \mu\text{mol} \times \text{L}^{-1}$ of Δ^9 -THC standard solution at different accumulation times. Supporting electrolyte: $0.15 \text{ mol} \times \text{L}^{-1}$ of KNO_3 , scan rate: $100 \text{ mV} \times \text{s}^{-1}$.

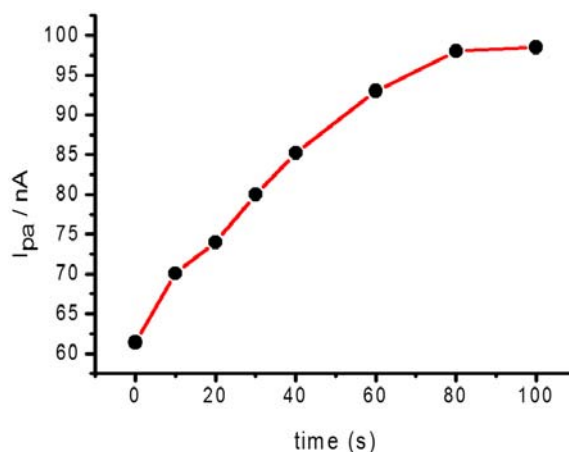


Fig. 3. Influence of pre-concentration time.

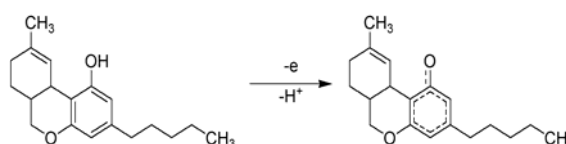


Fig. 4. Purposed electrooxidation of Δ^9 -THC molecule [2, 6, 9, 13].

3.3. Influence of Scan Rate

The effect of scan rates from 20 to $150 \text{ mV} \times \text{s}^{-1}$ on the voltammetric response was next investigated. (Fig. 5). The anodic peak potential increased proportionally with the applied scan rate. The change of anodic peak potential (E_{pa}) indicated that an irreversible process is occurring and that mass transport is controlled by adsorption of Δ^9 -THC. A scan rate of $100 \text{ mV} \times \text{s}^{-1}$ was adopted for future study of the influence of concentration. A linear dependence of I_{pa} against the scan rate is reported in the Fig. 6.

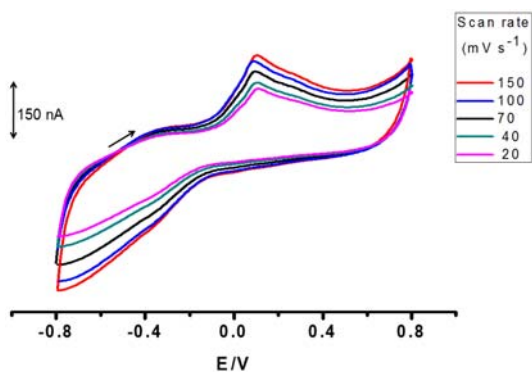


Fig. 5. An examination of the influence of scan rate on the cyclic voltammogram of an $18 \mu\text{mol}\times\text{L}^{-1}$ Δ^9 -THC standard solution. Time of accumulation: 60 s. Supporting electrolyte solution, $0.15 \text{ mol}\times\text{L}^{-1}$ potassium nitrate.

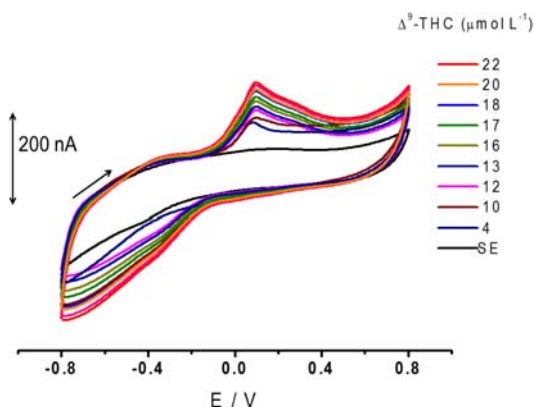


Fig. 7. Cyclic voltammogram referring to successive additions of Δ^9 -THC standard solution. Time of accumulation: 60 s. Scan rate: $100 \text{ mV}\times\text{s}^{-1}$.

3.4. Influence of Concentration

The voltammetric response to increasing concentrations of Δ^9 -THC applied to the electrode surface was next measured at 0.13 V vs. Ag-SPE. Fig. 7 shows the resultant cyclic voltammograms. The I_{pa} values increase linearly in proportion to concentration ($4 - 20 \mu\text{mol}\times\text{L}^{-1}$). The analytical curve (Fig. 8) produced a correlation coefficient (r^2) of 0.997 and a standard deviation (SD) of $0.01 \mu\text{A}$. The equation of the line was:

$$I_{pa} = 0.3 \mu\text{A} + 0.04 \mu\text{A}/\mu\text{mol}\times\text{L}^{-1} \Delta^9\text{-THC} \quad (1)$$

These results demonstrate a limit of detection (LOD) of $1.0 \mu\text{mol}\times\text{L}^{-1}$ and a limit of quantification (LOQ) of $3.3 \mu\text{mol}\times\text{L}^{-1}$ using the relationship $3\text{SD}/m$ and $10\text{SD}/m$ respectively, where m is the amperometric sensitivity of the line.

7. Conclusions

A method for the analysis of Δ^9 -THC was optimized using carbon screen printed electrodes. The process involves a 60 second pre-accumulation step

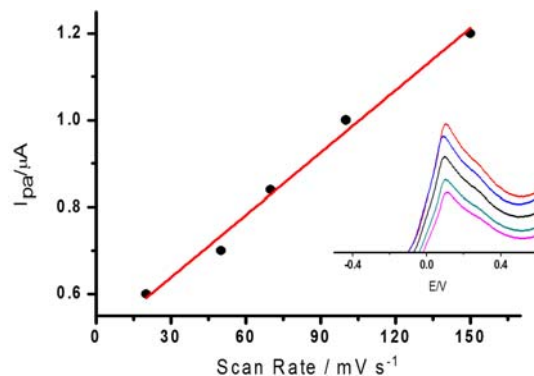


Fig. 6. Linear dependence of I_{pa} vs. scan rate.

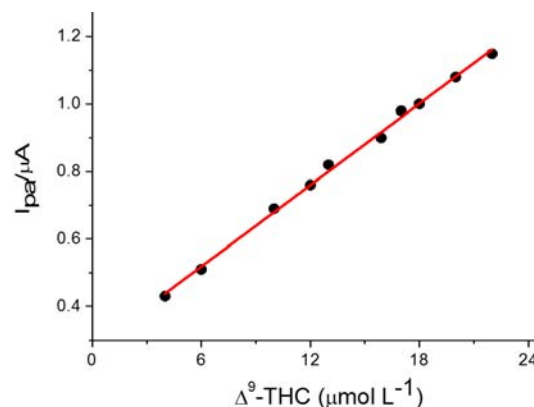


Fig. 8. Analytical curve I_{pa} vs. concentration of Δ^9 -THC standard solution ($\mu\text{mol L}^{-1}$).

followed by measurement of a peak current at 0.13 V vs. Ag-SPE. The resultant measurement produced a linear relationship between concentration and peak current with a limit of detection of $1.0 \mu\text{mol}\times\text{L}^{-1}$. This method should prove useful in the quantitative analysis of seized marijuana samples as well as in presumptive testing. Overall, the application of carbon screen printed electrodes is rapid, efficient and uses minimal chemical reagents, indicating that this procedure should be a useful alternative in forensic investigation.

Acknowledgements

We would like to thank Corredenação de Aperfeiçoamento de Pessoal de Nível Superior (CAPES Foundation, Edital Pró-Forenses 25/2014) and Fundação de Amparo à Pesquisa do Estado de São Paulo (FAPESP) for financial support.

References

- [1]. United Nations Office of Drugs and Crime World Drug Report, *United Nations Publication*, Sales No. E.16.XI.7, 2016, pp. 1-174.

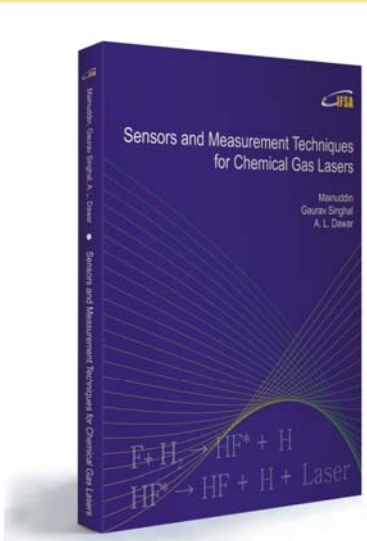
- [2]. R. Nissim, R. G. Compton, Absorptive stripping voltammetry for cannabis detection, *Chemistry Central Journal*, Vol. 9, Issue 41, 2015, pp. 1-7.
- [3]. J. G. Ramaekers, J. H. van Wel, D. B. Spronk, S. W. Toennes, K. P. C. Kuypers, E. L. Theunissen, R. J. Verkes, Cannabis and tolerance: acute drug impairment as a function of cannabis use history, *Scientific Reports*, Vol. 6, No. 26843, 2016, pp. 1-8.
- [4]. J. G. Ramaekers, G. Berghaus, M. van Laar, O. H. Drummer, Dose related risk of motor vehicle crashes after cannabis use, *Drug and Alcohol Dependence*, Vol. 73, 2014, pp. 109–119.
- [5]. M. A. Balbino, I. C. Eleotério, B. R. McCord, M. F. de Oliveira, Voltammetric detection of Δ^9 -THC using carbon screen printed electrode in aqueous media: improvements in forensic analysis, in *Proceedings of the 2nd International Conference on Sensors and Electronic Instrumentation Advances*, 2016, pp. 62-63.
- [6]. M. A. Balbino, L. S. de Oliveira, E. N. Oiyee., M. F. M. Ribeiro, B. R. McCord., A. J. Ipolito, M. F. de Oliveira, The Application of Voltammetric Analysis of Δ^9 -THC for the Reduction of False Positive Results in the Analysis of Suspected Marijuana Plant Matter, *Journal of Forensic Sciences*, Vol. 61, Issue 4, 2016, pp. 1067-1073.
- [7]. J. F. Kelly, K. Addanki, O. Bagasra, The nonspecific of Duquenois-Levine field test of marijuana, *The Open Forensic Science Journal*, Vol. 5, 2012, pp. 4-8.
- [8]. *Scientific Working Group for the Analysis of Seized Drugs*. Available: (<http://www.swgdrug.org/Documents/SWGDRUG%20Recommendations%20Version%207-1.pdf>).
- [9]. M. A. Balbino, M. M. T. de Menezes, I. C. Eleotério, A. A. Saczk, L. L. Okumura, H. M. Tristão, M. F. de Oliveira, Voltammetric determination of Δ^9 -THC in glassy carbon electrode: An important contribution to forensic electroanalysis, *Forensic Science International*, Vol. 221, 2012, pp. 29-32.
- [10]. M. F. M. Ribeiro, J. W. Cruz-Júnior, E. R. Dockal, B. R. McCord, M. F. de Oliveira, Voltammetric Determination of Cocaine Using Carbon Screen Printed Electrodes Chemically Modified with Uranyl Schiff Base Films, *Electroanalysis*, Vol. 28, 2016, pp. 320-326.
- [11]. M. A. Balbino, I. C. Eleotério, L. S. Oliveira, M. M. T. de Menezes, J. F. de Andrade, A. J. Ipolito, M. F. de Oliveira, A Comparative Study Between Two Different Conventional Working Electrodes for Detection of Δ^9 -Tetrahydrocannabinol Using Square-Wave Voltammetry: A New Sensitive Method for Forensic Analysis, *Journal of Brazilian Chemical Society*, Vol. 25, Issue 3, 2014, pp. 589-596.
- [12]. S. Hasan, D. Bromfield-Lee, M. T. Oliver-Hoyo, J. A. Cintron-Maldonado, Using Laboratory Chemicals to Imitate Illicit Drugs in a Forensic Chemistry Activity, *Journal of Chemical Education*, Vol. 85, Issue 6, 2008, pp. 813-816.
- [13]. M. A. Balbino, E. N. Oiyee, M. F. M. Ribeiro, J. W. Cruz-Júnior, I. C. Eleotério, A. J. Ipolito, M. F. de Oliveira, Use of screen-printed electrodes for quantification of cocaine and Δ^9 -THC: adaptations to portable systems for forensic purposes, *Journal of Solid State Electrochemistry*, Vol. 20, 2016, pp. 2435-2443.
- [14]. A. J. Bard, L. R. Faulkner, *Electrochemical methods: fundamentals and applications*, 2nd ed., *John Wiley and Sons*, 2001.
- [15]. P. G. Gandra, A. A. Alves, D. V. Macedo, L. T. Kubota, Electrochemical determination of antioxidant capacity for physical exercise evaluation, *Química Nova*, Vol. 27, Issue 6, 2004, pp. 980–985.
- [16]. P. T. Kissinger, W. R. Heineman, Cyclic voltammetry, *Journal of Chemical Education*, Vol. 60, Issue 9, 1983, pp. 702-706.
- [17]. L. S. de Oliveira, M. A. Balbino, M. M. T. de Menezes, E. R. Dockal, M. F. de Oliveira, Voltammetric analysis of cocaine using platinum and glassy carbon electrodes chemically modified with Uranyl Schiff base films, *Microchemical Journal*, Vol. 110, 2013, pp. 374–378.
- [18]. L. S. de Oliveira, A. P. S. Poles, M. A. Balbino, M. M. T. de Menezes, J. F. de Andrade, E. R. Dockal, H. M. Tristão, M. F. de Oliveira, Voltammetric Determination of Cocaine in Confiscated Samples Using a Carbon Paste Electrode Modified with Different [UO₂(X-MeOSalen)(H₂O)]·H₂O complexes, *Sensors*, Vol. 13, No. 6, 2013, pp. 7668-7679.
- [19]. M. T. Fernández-Abedul, J. R. B. Rodriguez, A. Costa-Garcia, P. T. Blanco, Voltammetric determination of cocaine in confiscated samples, *Electroanalysis*, Vol. 3, 1991, pp. 409–412.
- [20]. V. Pavlova, V. Mirceski, Š. Komorsky-Lovric, S. Petrovska-Jovanovic, B. Mitrevski, Studying electrode mechanism and analytical determination of cocaine and its metabolites at the mercury electrode using square-wave voltammetry, *Analytica Chimica Acta*, Vol. 512, Issue 1, 2004, pp. 49–56.
- [21]. E. N. Oiyee, N. B. de Figueiredo, J. F. de Andrade, M. F. de Oliveira, Voltammetric determination of cocaine in confiscated samples using a cobalt hexacyanoferrate film-modified electrode, *Forensic Science International*, Vol. 192, No. 1-3, 2009, pp. 94-97.
- [22]. M. C. Tadini, M. A. Balbino, I. C. Eleotério, L. S. de Oliveira, L. G. Dias, G. D. Jean-François, M. F. Oliveira, Developing electrodes chemically modified with cucurbit[6]uril to detect 3,4 methylenedioxymethamphetamine (MDMA) by voltammetry, *Electrochimica Acta*, Vol. 121, 2014, pp. 188–193.
- [23]. L. R. Cumba, J. P. Smith, K. Y. Zuway, O. B. Sutcliffe, D. R. do Carmo, C. E. Banks, Forensic electrochemistry: simultaneous voltammetric detection of MDMA and its fatal counterpart “Dr Death” (PMA), *Analytical Methods*, Vol. 8, 2016, pp. 142-152.
- [24]. E. M. P. J. Garrido, Electrochemical oxidation of amphetamine-like drugs and application to electroanalysis of ecstasy in human serum, *Bioelectrochemistry*, Vol. 79, No. 1, 2010, pp. 77-83.
- [25]. A. Goodwin, C. E. Banks, R. G. Compton, Graphite micropowder modified with 4-amino-2,6-diphenylphenol supported on basal plane pyrolytic graphite electrodes: micro sensing platforms for the indirect electrochemical detection of Δ^9 -tetrahydrocannabinol in saliva, *Electroanalysis*, Vol. 11, 2006, pp. 1053–1067.
- [26]. E. R. Lowe, C. E. Banks, R. G. Compton, Indirect detection of substituted phenols and cannabis based on the electrochemical adaptation of the Gibbs reaction, *Analytical and Bioanalytical Chemistry*, Vol. 383, Issue 3, 2005, pp. 523–531.
- [27]. I. Novak, M. Mlakar, S. Komorsky-Lovric, Voltammetry of immobilized particles of cannabinoids. *Electroanalysis*, Vol. 25, Issue 12, 2013, pp. 2631–2636.

- [28]. A. Bobrowski, A. Krýlicka, M. Maczuga, J. Zarebski, Highly Sensitive and Selective Adsorptive Stripping Voltammetric Method Employing a Lead Film Screen-printed Electrode for Determination of Cobalt as its Nioximate Complex, *Electroanalysis*, Vol. 28, Issue 2, 2016, pp. 343-349.
- [29]. L. Asturias-Arribas, M. A. Alonso-Lomillo, O. Domínguez-Renedo, M. J. Arcos-Martínez, Sensitive and selective cocaine electrochemical detection using disposable sensors, *Analytica Chimica Acta*, Vol. 834, 2014, pp. 30-36.
- [30]. L. Asturias-Arribas, M. A. Alonso-Lomillo, O. Domínguez-Renedo, M. J. Arcos-Martínez, CYP450 biosensors based on screen-printed carbon electrodes for the determination of cocaine, *Analytica Chimica Acta*, Vol. 685, 2011, pp. 15-20.
- [31]. L. Asturias-Arribas, M. A. Alonso-Lomillo, O. Domínguez-Renedo, M. J. Arcos-Martínez, Electrochemical determination of cocaine using screen-printed cytochrome P450 2B4 based biosensors, *Talanta*, Vol. 685, Issue 1, 2011, pp. 15-20.
- [32]. C. Wanklyn, D. Burton, E. Enston, C. Bartlett, S. Taylor, A. Raniczkowska, M. Black, L. Murphy, Disposable screen printed sensor for the electrochemical detection of delta-9-tetrahydrocannabinol in undiluted saliva, *Chemistry Central Journal*, Vol. 10, Issue 1, 2016.
- [33]. M. O. Sales, T. R. L. C. da Paixão, Voltametria, in B. S. De Martinis, M. F. de Oliveira, Química Forense Experimental, *Cengage Learning*, 2016, pp. 261-275.
- [34]. C. M. Oliveira, A. S. Barros, A. C. S. Ferreira, A. M. S. Silva, Study of quinones reactions with wine nucleophiles by cyclic voltammetry, *Food Chemistry*, Vol. 11, 2016, pp. 1-7.
- [35]. N. R. Stradiotto, H. Yamanaka, M. V. B. Zanoni, Electrochemical Sensors: A Powerful Tool in Analytical Chemistry, *Journal of Brazilian Chemical Society*, Vol. 14, Issue 2, 2003, pp. 159-173.
- [36]. E. Burestedt, A. Narvaez, T. Ruzgas, L. Gorton, J. Emneus, E. Domingues, G. Marko Varga, Rate-limiting steps of tyrosinase-modified electrodes for the detection of catechol, *Analytical Chemistry*, Vol. 68, Issue 9, 1996, pp. 1605-1611.




Published by International Frequency Sensor Association (IFSA) Publishing, S. L., 2016 (<http://www.sensorsportal.com>).

Sensors and Measurement Techniques for Chemical Gas Lasers



Mainuddin
Gaurav Singhal
A. L. Dawar



Sensing and measurement are the key technologies in the development of chemical gas lasers. These advanced technologies are required to acquire, analyze and transform data into information that is useful to enhance the performance and capabilities of these lasers systems.

The goal of this book is to enable scientists and technologists working in rather complex area of chemical lasers to achieve the best technical performances. Till now such topics have been covered scantily in open literature and that too in the research papers only.

Hardcover: ISBN 978-84-617-1152-9
Printable PDF: ISBN 978-84-617-1865-8

Order: http://www.sensorsportal.com/HTML/BOOKSTORE/Gas_lasers.htm

Dual Approach to Amplify Anodic Stripping Voltammetric Signals Recorded Using Screen Printed Electrodes

Agnieszka KRÓLICKA

AGH University of Science and Technology, Faculty of Materials Science and Ceramics, Department of Building Materials Technology, Al. Mickiewicza 30, 30-059 Kraków, Poland

Tel.: +48 12 617 48 61, fax: +48 12 617 38 99

*E-mail: krolicka@agh.edu.pl

Received: 5 November 2016 /Accepted: 5 December 2016 /Published: 30 December 2016

Abstract: Screen printed electrodes plated with bismuth were used to record anodic stripping voltammograms of Pb(II), In(III) and Cd(II). Using two bismuth precursors: Bi₂O₃ dispersed in the electrode body and Bi(III) ions spiked into the tested solution it was possible to deposit bismuth layers, demonstrating exceptional ability to accumulate metals forming alloys with bismuth. The voltammetric signals were amplified by adjusting the electrode location with respect to rotating magnetic field. The electrode response was influenced by vertical and horizontal distance between the magnet center and the sensing area of screen printed electrode as well as the angle between the magnet surface and the electrode. When the electrode was moved away from the magnet center the recorded peaks were increasingly smaller and almost not affected by the presence of bismuth ions. It was shown that to obtain well-shaped signals a favourable morphology of bismuth deposits is of key importance. Hypotheses explaining processes responsible for the amplification of voltammetric signals were proposed.

Keywords: Screen printed electrodes, Anodic stripping voltammetry, Bismuth precursors, Bismuth film electrode.

1. Introduction

Anodic stripping voltammetry (ASV) is a proven electrochemical method for trace metal analysis, providing low detection limits (sub μgL^{-1} range) and the capability of multimetal analysis. All stripping techniques have two consecutive steps in common: preconcentration of analyte species and follow-up electrooxidation or electroreduction of accumulated analyte. After accumulation the recorded signals are several times higher than that not preceded by analyte accumulation and, in this way, the stripping

techniques have the lowest limits of detection of any of the commonly used electroanalytical techniques.

Historically, mercury was the electrode of choice for ASV. Recently, however, there has been much interest in developing substitute electrode materials because of mercury's toxicity and volatility. Bismuth is an alternate electrode material that possesses many of the same properties for metal ion analysis that mercury does, and is both non-toxic and non-volatile [1]. Some of the attractive properties of bismuth electrodes for electroanalysis are their wide negative potential window, large overpotential for hydrogen evolution, insensitivity to dissolved oxygen (an

essential feature for onsite applications) and simple preparation. Bismuth film electrodes (BiFEs) have been found to provide a sensitive, reproducible, and stable response for several metal ions [2] and other priority organic compounds [3] in different types of samples.

The unique capability of bismuth electrode to accumulate metals could be ascribed to the ability of bismuth to form 'fused' alloys, with a melting point below 100 °C [4]. Bismuth readily combines with many metals and forms with them binary and multimetal alloys: binary (e.g., Bi-Pb), ternary (e.g., Bi-Pb-Sn; Bi-Sn-In), quaternary (e.g., Bi-Pb-Sn-Cd) and even quinary (e.g., Bi-Pb-Sn-Cd-In) or senary (e.g., Bi-Pb-Sn-Cd-In-Tl). Electrodeposited alloys are similar to thermally prepared alloys in structure and they usually contain the same phases [5].

During co-deposition of bismuth and one or more metals not only an alloy can be deposited but also formation of individual crystals of each metal is possible. The formation of different deposits of zinc on both bismuth and carbon support, which exhibit different lattice energy, was responsible for peak splitting reported for screen printed and glassy carbon electrodes [6-7].

Unlike spectrometric methods, electrochemical techniques are suitable for miniaturization and on-site applications. Using microfabrication techniques (e.g. chemical or physical vapor deposition coupled with photolithography) or screen-printing techniques it is possible to produce small planar electrodes serving as electrochemical sensors.

The screen-printed electrodes (SPEs) have been attracting increasing interest in stripping voltammetry as an alternative substrate for metal film formation because of their numerous advantages, such as mass production, low cost, small size, lower susceptibility to oxygen interferences and the possibility of disposal after a single use [8-10]. Moreover, integrated screen-printed electrodes comprising 3-electrodes on one strip require smaller amounts of samples, which decreases the volume of the solutions used and waste generated. SPEs could be coupled with portable, battery-operated electrochemical analyzers making them a convenient tool for on-site analysis for the reasons of cost, simplicity, speed (analysis time shorter than 5 min), sensitivity (LOD's below $\mu\text{g/l}$) and portability. Before the application of the SPE's in voltammetric analysis its surface is frequently modified with additional layers which positively influence their voltammetric performance.

In this paper SPE's plated with bismuth film originating from two bismuth precursors: Bi_2O_3 dispersed in the electrode body and Bi(III) ions spiked into the tested solution were applied for the development of Pb(II), In(III) and Cd(II) voltammetric curves. The deposition of bismuth film was performed using different locations of SPE strips with the respect to magnetic field induced by the rotating permanent magnet. Eventually, the synergic effect of two bismuth precursors and the favorable location of SPE contributed to the amplification of target metals.

2. Experimental

2.1. Apparatus and Instrumentation

Electrochemical measurements were performed using an Autolab PGSTAT204 (Nova 1.10.1.9 software) potentiostat with a standard three-electrode configuration. The screen-printed electrodes (4 mm in diameter; bismuth-oxide-modified DRP 110BI) were provided by Dropsens, Spain. The magnetic stirrer (Metrohm 801) was controlled with NOVA software. The magnet built into the stirring device induced a magnetic field of up to 86 mT, while the field induced by the 7 mm long stirring flea was up to 3 mT. The voltammetric experiments were performed in the cuboid (50×50×29 mm) polystyrene vessel.

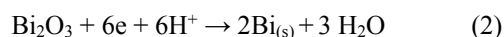
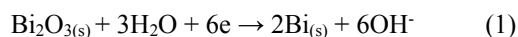
2.2. Procedure

Prior to the experiments, the SPE electrode was immersed in the tested solution for 1 minute. The supporting electrolyte contained 0.08 M $\text{CH}_3\text{COONH}_4$, $1.5 \text{ mg}\cdot\text{l}^{-1}$ Bi(III), $0.26 \text{ g}\cdot\text{l}^{-1}$ NaCl, and had a pH of 6.3. The accumulation potential of -1.5 V was then applied for 300 s and the DP-ASV curve was recorded within the range of -1.5 V to 0.3 V. During accumulation, the solution was stirred using a magnetic bar. The parameters of the DPV mode were as follows: $\Delta E = 25 \text{ mV}$, $E_s = 5 \text{ mV}$, $t_{\text{eq}} = 5 \text{ s}$.

3. Results and Discussion

3.1. The Selection of Bismuth Precursor

The SPEs modified with bismuth oxide were chosen as a sensor for anodic stripping voltammetric studies. Bismuth oxide may be electrochemically converted to metallic bismuth in both highly alkaline media (1) and acidic media (2) after the application of a negative potential.



When other metals are present in the solution they could be co-deposited with bismuth. During co-deposition alloys or deposits consisting of individual crystals of target metals and bismuth are formed. In the course of stripping the opposite process takes place, namely the target metal and bismuth are stripped off from the electrode surface by positive going potential scan.

In Fig. 1 the ASV voltammograms recorded using bismuth film deposited in 0.1 M KOH by electroreduction of Bi_2O_3 dispersed in SPE carbon ink are shown. The recorded signals of Zn(II) and Cd(II) did not stabilize and continued to drift downward starting from the fourth curve. When the fifth

voltammogram is considered the zinc signal retained only 6 % of the current value measured on the first voltammogram.

Given that poor performance of bismuth films deposited in alkaline media the consecutive experiments involved bismuth films plated in acidic media only.

The first results obtained after deposition of bismuth layer from bismuth oxide dispersed in SPE's ink were still unsatisfactory. The ASV peaks recorded using such electrode (Fig. 2, curves 1-3) were rather low, wide and sometimes distorted by undesirable shoulders. The electrode response improved clearly only after Bi(III) ions were introduced into the tested solution (Fig. 2, curve 4). Using a combination of these two precursors i.e. Bi₂O₃ dispersed in carbon ink and Bi(III) present in the examined solution, it was possible to deposit bismuth layers demonstrating exceptional ability to accumulate metals forming alloys with bismuth [11]. The double-precursor-electrode was therefore selected as suitable for further experiments.

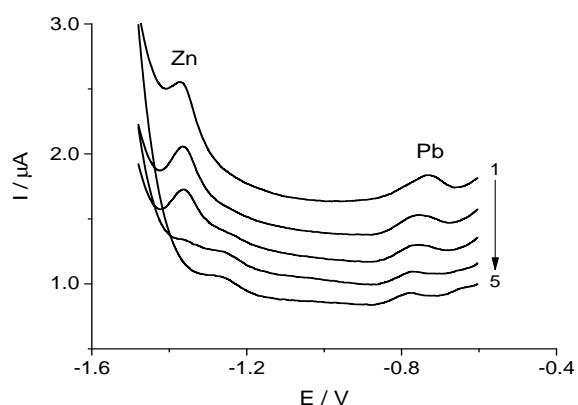


Fig. 1. DP-ASV curves of Zn(II) and Pb(II) obtained in mineral water. Composition of the examined solution: mineral water diluted 2 times, 0.08 M CH₃COONH₄, pH = 6.3. E_{acc} = -1.5 V, t_{acc} = 300 s. Plating procedure: 0.1 M KOH, E_{plat} = -1.2 V, t_{plat}: 600 s (ex-situ plating).

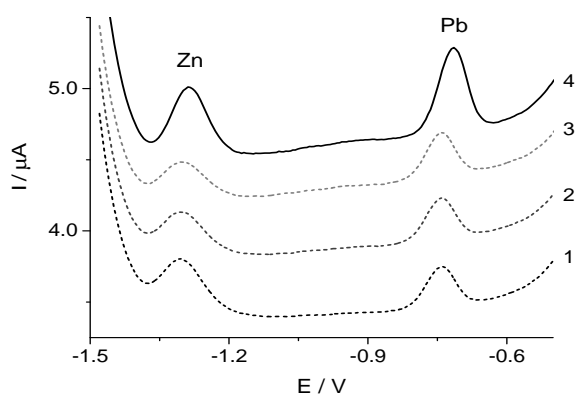


Fig. 2. DP-ASV curves of Zn(II) and Pb(II) obtained in mineral water. Composition of the examined solution: mineral water diluted 2 times, 0.08 M CH₃COONH₄ (curves 1 – 3), 1.5 mg×l⁻¹ Bi(III) (curve 4), pH = 6.3. E_{acc} = -1.5 V, t_{acc} = 300 s. Plating procedure: bismuth co-deposited with target ions (in-situ plating).

3.2. The Arrangement of SPE and Magnetic Stirrer

The ASV signal of examined metals could be amplified by another 200 %-600 % after adjusting the SPE location with respect to magnetic field [11-12]. Three factors were considered: (v) vertical and (h) horizontal distance between the magnet center and the sensing area of SPE and, finally, the angle (α) between the magnet surface and the SPE strip as shown in Fig. 3. Effect of different SPE arrangements on the geometry of voltammograms of lead, indium and cadmium is shown in Figs. 4–7.

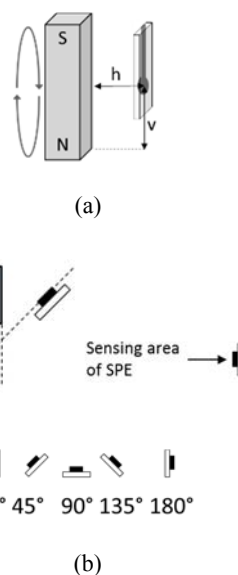


Fig. 3. (a) Side, and (b) top view of SPE arrangement. M – magnet.

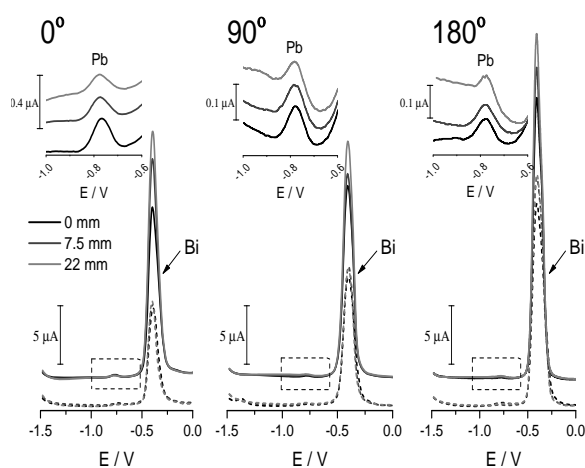


Fig. 4. DP-ASV curves of Pb(II) obtained in the absence (dash line) in the presence (solid line) of Bi(III) ions at different vertical (v) SPE's location. Composition of the examined solution: 10 μg×l⁻¹ Pb(II), 0.08 M CH₃COONH₄, 1.5 mg×l⁻¹ Bi(III) (solid lines only), pH = 6.3, 0.26 g×l⁻¹ NaCl. E_{acc} = -1.5 V, t_{acc} = 300 s. h = 8 mm. Insets: magnified fragment of voltammograms showing lead signals.

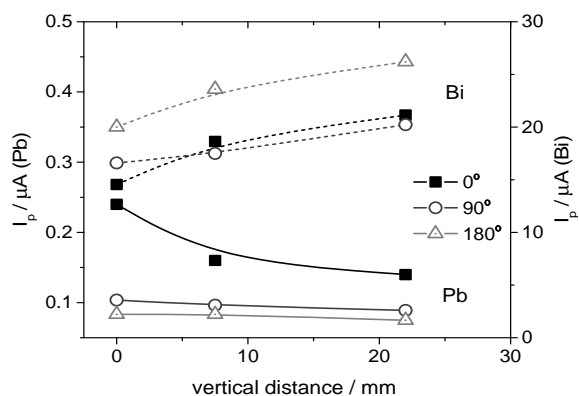


Fig. 5. The influence of vertical location and of the angle (α) between the magnet surface and the SPE strip on the lead (solid line) and bismuth (dash line) signal. $h = 0.8$ cm, $c_{\text{Pb(II)}} = 10 \mu\text{g}\times\text{l}^{-1}$. Other parameters as in Fig. 3.

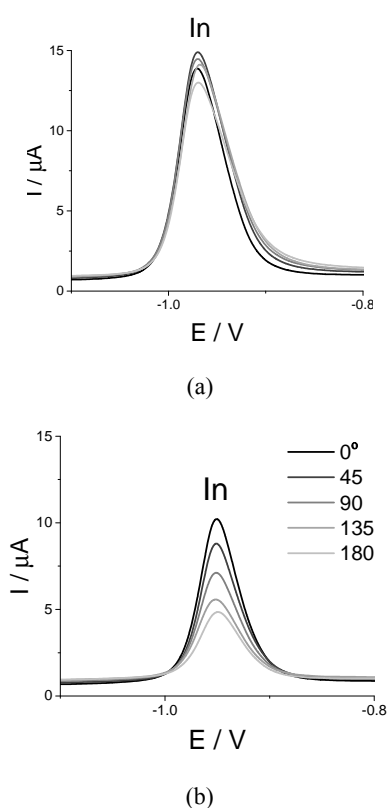


Fig. 6. DP-ASV curves recorded in two horizontal locations of SPE: (a) $h = 0.8$ cm, (B) $h = 1.6$ cm (b) and different α values. $v = 0$ cm, $c_{\text{In(III)}} = 50 \mu\text{g}\times\text{l}^{-1}$.

In the absence of Bi(III) ions in the examined solution the influence of SPE location on both lead (analyte) and bismuth (film material) signals is minimal (Fig. 4, dash line). When examined solution was spiked with Bi(III) ions the lead signal exhibited clear dependence on the location and SPE's angle. The highest lead signals were observed when the electrode was parallel to the stirring plane and the distance from magnet center was minimal. The opposite trend was observed for bismuth signal (Fig. 5). As far as indium and cadmium signals go, increasing of the distance between the magnet and the SPEs' surface both in

horizontal (Fig. 6) and vertical directions (Fig. 7) caused a decrease in their peak currents.

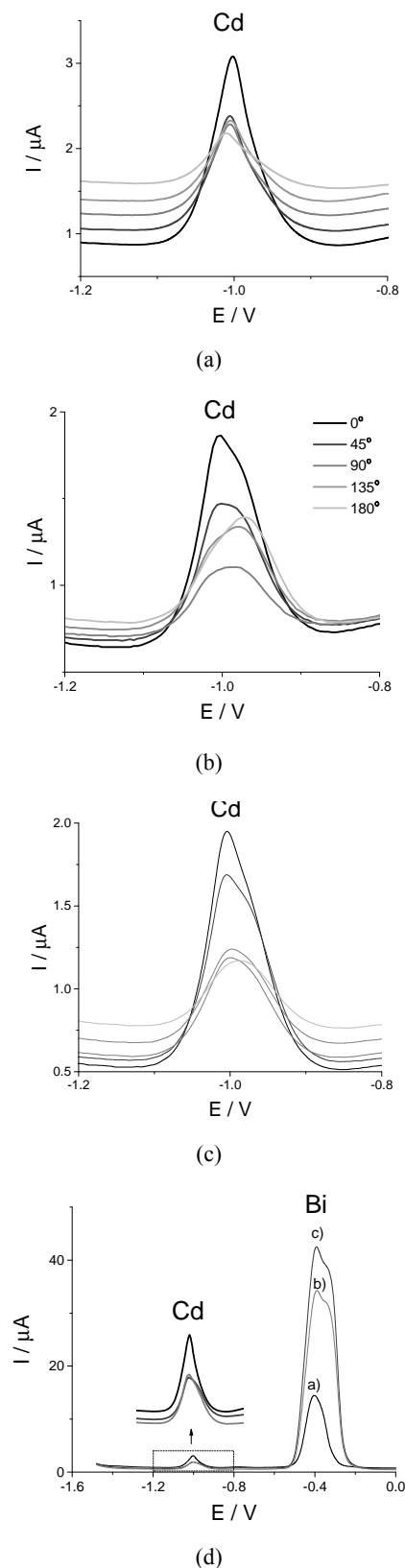


Fig. 7. DP-ASV curves recorded in three SPE positions: (a) $h = 0.8$ cm, $v = 0.75$ cm, (b) $h = 0.8$ cm, $v = 1.5$, (c) $h = 1.6$ cm, $v = 2.2$ cm and different α values. (d) voltammograms for $\alpha = 0^\circ$, $c_{\text{Cd(II)}} = 50 \mu\text{g}\times\text{l}^{-1}$.

The influence of the angle α was more complex and depended on SPE localization and the type of target element. In the case of indium, when the SPE was immersed in the location expressed by $v = 0$ cm and $h = 0.8$ cm, α did influence the In signal intensity but only to a small degree (up to about 15 %). If the location of the SPE was more distant ($h = 1.6$ cm) the 180 degrees rotation of the SPE produced a large, 60 % drop in the signal intensity (Fig. 6).

Additionally, the SPE rotation angle α influenced not only the signal intensity but also its symmetry. The SPE's performance in terms of cadmium signal symmetry is highest at central locations. At farther, more peripheral locations the SPE's performance decreased and cadmium signals were wide and distorted by shoulders (Fig. 7(b), Fig. 7(c)). Not only cadmium signals but also bismuth peaks became considerably wider at peripheral locations of SPE (Fig. 7(d)). The signal splitting indicates that crystallites formed at the peripheral SPEs locations during accumulation are non-identical and, therefore, different energy must be delivered to oxidize them.

Furthermore, a comparison of oxidation signals shown in Fig. 4 and Fig. 7(d) (representing lead, cadmium and bismuth oxidation) reveals that it is not the amount of bismuth which is crucial to obtain well-shaped signals of cadmium but, instead, a favourable morphology of bismuth deposits is of key importance. As shown in Fig. 4 and Fig. 7(d), when the oxidation signal of bismuth is at minimum the cadmium signal reaches its highest value.

4. Conclusions

It was shown that using two bismuth precursors and a favorable location of SPE with respect to magnetic stirrer it is possible to greatly amplify ASV signal of lead, cadmium and indium.

To explain the role of two precursors and the influence of the location of SPEs in the magnetic field on the quality of the signals recorded using anodic stripping voltammetry several factors should be taken into consideration.

The electrochemical reduction of Bi_2O_3 solid particles was considered by Hwong [13]. The obtained results indicated that bismuth oxide could be successfully reduced to metallic bismuth during the electrochemical reduction step. However, it was observed that bismuth particles were highly agglomerated after the electrochemical reduction. The deposited crystals were non-identical and required different energy for the oxidation process to occur. When the bismuth film was deposited by reducing Bi_2O_3 the stripping peaks of deposited metals were wide and distorted by shoulders, which in turn indicates that they probably resulted from the stripping of metal layers with slightly different lattice energy [6, 14]. According to voltammetric results reflecting the structure of these deposited metals, the metal layers deposited using two precursors – Bi_2O_3 and Bi(III) – were more homogenous because signals

delivered by that electrodes were narrow and symmetrical.

By changing the location of SPE with respect to the stirring plane the transport of electroactive substances may be affected, especially Bi(III) ions. In the absence of Bi(III) ions the dependence of the anodic stripping signals on the location of SPE was barely discernible.

The results of studies investigating the effect of the magnetic field on the electrodeposition of bismuth [15-17] show that it is a very complex process. It is also reported that the magnetic field has no influence on the structure of Bi deposited from electrolytes containing diamagnetic Bi(III) ions [16]; however, when electrochemically inert paramagnetic ions are added to the electrolyte [16] the bismuth films were thinner in regions with a high magnetic gradient.

The electrodeposition at relatively negative potentials in acidic media leads to the reduction of protons and evolution of hydrogen bubbles, an increase in the pH value and subsequent hydroxide formation. The convection induced locally, occurring in inhomogeneous magnetic fields, can remove the hydrogen bubbles and hydroxide particles, which might block the electrode surface and favor the deposition of analyte, bismuth or their alloys.

In summary, it is evident that the external magnetic field applied to the electrochemical cell is an extra variable which influences processes taking place in it. It is difficult though to unambiguously indicate which processes are responsible for the observed amplification of voltammetric signals.

Acknowledgements

Financial support from the Polish National Science Centre (Project 2014/15/B/ST8/03921) is gratefully acknowledged.

References

- [1]. J. Wang, J. Lu, S.B. Hocevar, P. A. M Farias, Bismuth-Coated Carbon Electrodes for Anodic Stripping Voltammetry, *Analytical Chemistry*, Vol. 72, Issue 14, 2000, pp. 3218–3222.
- [2]. I. Svancara, C. Prior, S. B. Hocevar, J. Wang, A Decade with Bismuth-Based Electrodes in Electroanalysis, *Electroanalysis*, Vol. 22, Issue 15-16, 2010, pp. 1405–1420.
- [3]. N. Lezi, V. Vyskocil, A. Economou, J. Barek, Electroanalysis of Organic Compounds at Bismuth Electrodes, A Short Review, *Sensing in Electroanalysis*, Eds. K. Kalcher, R. Metelka, I. Svancara, K. Vytras, University Press Centre: Pardubice, Czech Republic, Vol. 7, 2012, pp. 71-78.
- [4]. A. J. Bard, G. Inzelt, F. Scholz, (eds.) Electrochemical Dictionary, *Springer Science & Business Media*, 2008.
- [5]. A. Brenner, Electrodeposition of Alloys: Principles and Practice, Vol. 1, *Academic Press*, 1963.
- [6]. A. Crew, D. C. Cowell, J. P. Hart, Development of an anodic stripping voltammetric assay, using a disposable mercury-free screen-printed carbon

- electrode, for the determination of zinc in human sweat, *Talanta*, Vol. 75, Issue 5, 2008, pp. 1221–1226.
- [7]. A. Królicka, A. Bobrowski, A. Kowal, Effects of Electroplating Variables on the Voltammetric Properties of Bismuth Deposits Plated Potentiostatically, *Electroanalysis*, Vol. 18, Issue 17, 2006, pp. 1649–1657.
- [8]. M. Li, Y.-T. Li, D.-W. Li, Y.-T. Long, Recent developments and applications of screen-printed electrodes in environmental assays - A review, *Analytica Chimica Acta*, Vol. 734, 2012, pp. 31-44.
- [9]. Z. Taleat, A. Khoshroo, M. Mazloum-Ardakani, Screen-printed electrodes for biosensing: a review (2008–2013), *Microchimica Acta*, Vol. 181, Issue 9-10, 2014, pp. 865–891.
- [10]. A. Hayat, J. L. Marty, Disposable Screen Printed Electrochemical Sensors: Tools for Environmental Monitoring, *Sensors*, Vol. 14, Issue 6, 2014, 10432-10453.
- [11]. A. Królicka, A. Bobrowski, Employing a magnetic field to amplify zinc signal obtained at bismuth film screen-printed electrodes generated using dual bismuth precursor, *Electrochimica Acta*, Vol. 187, Issue 1, 2016, pp. 224-233.
- [12]. A. Królicka, A. Bobrowski, M. Czarnota, Amplification of anodic stripping voltammetric signals recorded using screen printed electrodes in weak magnetic fields, in *Proceedings of the Conference on Sensors Engineering and Electronics Instrumental Advances (SEIA'2016)*, Barcelona, Castelldefels, Spain, 22-23 September 2016, pp.107-109.
- [13]. G. H. Hwang, W. K. Han, S. J. Kim, S. J. Hong, J. S. Park, H. J. Park, S. G. Kang, An electrochemical preparation of bismuth nanoparticles by reduction of bismuth oxide nanoparticles and their application as an environmental sensor, *Journal of Ceramic Processing Research*, Vol. 10, Issue 2, 2009, pp. 190-194.
- [14]. K. C. Honeychurch, J. P. Hart, D. C. Cowell, Voltammetric Behavior and Trace Determination of Lead at a Mercury-Free Screen-Printed Carbon Electrode, *Electroanalysis*, Vol. 12, Issue 3, 2000, pp. 171-177.
- [15]. C. O'Reilly, G. Hinds, J. M. D. Coey, Effect of a Magnetic Field on Electrodeposition; Chronoamperometry of Ag, Cu, Zn, and Bi, *Journal of The Electrochemical Society*, Vol. 148, Issue 10, 2001, pp. C674-C678.
- [16]. K. Tschulik, Ch. Cierpka, G. Mutschke, A. Gebert, L. Schultz, M. Uhlemann, Clarifying the Mechanism of Reverse Structuring Electrodeposition in Magnetic Gradient Fields, *Analytical Chemistry*, Vol. 84, Issue 5, 2012, pp. 2328–2334.
- [17]. K. Tschulik, J. Adam Koza, M. Uhlemann, A. Gebert, L. Schultz, Effects of well-defined magnetic field gradients on the electrodeposition of copper and bismuth, *Electrochemistry Communications*, Vol. 11, Issue 11, 2009, pp. 2241–2244.



Published by International Frequency Sensor Association (IFSA) Publishing, S. L., 2016 (<http://www.sensorsportal.com>).

NANOSENSORS: Materials and Technologies

Hardcover: ISBN 978-84-616-5378-2
e-Book: ISBN 978-84-616-5422-2



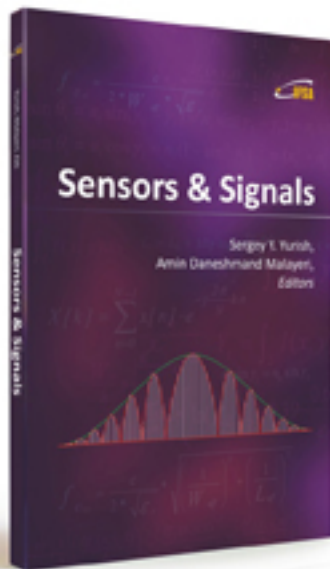
Nada F. Atta, Ed.



Nanosensors: Materials and Technologies aims to provide the readers with some of the most recent development of new and advanced materials such as carbon nanotubes, graphene, sol-gel films, self-assembly layers in presence of surface active agents, nano-particles, and conducting polymers in the surface structuring for sensing applications. The emphasis of the presentations is devoted to the difference in properties and its relation to the mechanism of detection and specificity. Miniaturization on the other hand, is of unique importance for sensors applications. The chapters of this book present the usage of robust, small, sensitive and reliable sensors that take advantage of the growing interest in nano-structures. Different chemical species are taken as good example of the determination of different chemical substances industrially, medically and environmentally. A separate chapter in this book will be devoted to molecular recognition using surface templating.

The present book will find a large audience of specialists and scientists or engineers working in the area of sensors and its technological applications. The *Nanosensors: Materials and Technologies* will also be useful for researchers working in the field of electrochemical and biosensors since it presents a collection of achievements in different areas of sensors applications.

Order: http://www.sensorsportal.com/HTML/BOOKSTORE/Nanosensors_IFSA.htm



Sensors & Signals

Sergey Y. Yurish,
Amin Daneshmand Malayeri,
Editors

Sensors & Signals is the first book from the Book Series of the same name published by IFSA Publishing. The book contains eight chapters written by authors from universities and research centers from 12 countries: Cuba, Czech Republic, Egypt, Malaysia, Morocco, Portugal, Serbia, South Korea, Spain and Turkey. The coverage includes most recent developments in:

- Virtual instrumentation for analysis of ultrasonic signals;
- Humidity sensors (materials and sensor preparation and characteristics);
- Fault tolerance and fault management issues in Wireless Sensor Networks;
- Localization of target nodes in a 3-D Wireless Sensor Network;
- Opto-elastography imaging technique for tumor localization and characterization;
- Nuclear and geophysical sensors for landmines detection;
- Optimal color space for human skin detection at image recognition;
- Design of narrowband substrate integrated waveguide bandpass filters.

Each chapter of the book includes a state-of-the-art review in appropriate topic and well selected appropriate references at the end.

With its distinguished editors and international team of contributors *Sensors & Signals* is suitable for academic and industrial research scientists, engineers as well as PhD students working in the area of sensors and its application.



Order: http://www.sensorsportal.com/HTML/BOOKSTORE/Sensors_and_Signals.htm



www.sensorsportal.com

ISSN 2306-8515



9 772306 851006